

**UNIVERSITÉ LIBRE DE BRUXELLES
FACULTE DES SCIENCES**



**ET
UNIVERSITÉ PAVOL JOZEF ŠAFÁRIK DE KOŠICE
FACULTE DES SCIENCES**

**Studies of Diffractive Scattering of Photons at
Large Momentum Transfer And of the VFPS
Detector at HERA**

**Dissertation présentée en vue
de l'obtention du titre de
Docteur en Sciences**

Tomáš HREUS

Septembre 2008

Abstract

In this thesis, two studies of the diffractive phenomena in the electron proton collisions with the H1 detector at HERA are presented. The first is the study of the inclusive elastic diffractive events $ep \rightarrow eXp$ in the regime of high photon virtuality ($Q^2 > \text{few GeV}^2$), with the scattered proton detected by the Very Forward Proton Spectrometer (VFPS). The VFPS detector, designed to measure diffractive scattered protons with high acceptance, has been installed in 2004 to benefit from the HERA II luminosity increase. The selected event sample of an integrated luminosity of 130.2 pb^{-1} was collected in years 2006-2007. Data sample distributions are compared to the prediction based on the diffractive parton distribution functions, as extracted from the H1 measurement of the diffractive structure function $F_2^{D(3)}$ at HERA I. After the study of the VFPS efficiency, the VFPS acceptance as a function of x_P is estimated and studied in relation to the forward proton beam optics.

The second study leads to the cross section measurement of the diffractive scattering of quasi-real photons off protons, $\gamma p \rightarrow \gamma Y$, with the large momentum transfer, $|t|$. The final state photon is separated from the proton dissociation system, Y , by a large rapidity gap and has a large transverse momentum, $p_T > 2 \text{ GeV}$. Large p_T imply the presence of the hard scale t ($|t| \simeq p_T^2$) and allows predictions of the perturbative QCD to be applied. The measurement is based on an integrated luminosity 46.2 pb^{-1} of data collected in the 1999-2000 running period. Cross sections $\sigma(W)$ as a function of the incident photon-proton centre of mass energy, W , and $d\sigma/d|t|$ are measured in the range $Q^2 < 0.01 \text{ GeV}^2$, $175 < W < 247 \text{ GeV}$, $4 < |t| < 36 \text{ GeV}^2$ and $y_P < 0.05$. The cross section measurements have been compared to predictions of LLA BFKL calculations.

Contents

1	Introduction	7
2	Theoretical Overview	9
2.1	Deep Inelastic Scattering	9
2.1.1	Kinematics	9
2.1.2	DIS Cross Section and Parton Model	11
2.1.3	Quantum Chromodynamics	12
2.1.4	Evolution of Parton Distribution Functions	12
2.1.5	Hadronisation	15
2.2	Inclusive Diffractive Scattering	16
2.2.1	Diffraction in the DIS regime	16
2.2.2	Diffractive Structure Function And the Factorisation	18
2.2.3	Recent Results on the Partonic Structure of the Pomeron	19
2.3	Diffractive Scattering of Photons with Large Momentum Transfer	21
2.4	Simulation of Physics Processes	23
2.4.1	The RAPGAP Event Generator	24
2.4.2	The HERWIG Event Generator	24
2.4.3	H1 Detector Simulation And Reconstruction	24
3	H1 Experiment at HERA	25
3.1	The H1 Detector	30
3.1.1	Tracking Detectors	30
3.1.2	Calorimeters	34
3.1.3	The Muon System	36
3.1.4	Time of Flight Counters	36
3.1.5	The Luminosity System	36
3.1.6	The Trigger System	38
3.2	The Very Forward Proton Spectrometer	41
3.2.1	Design and Location	42
3.2.2	The x_P and t Reconstruction	45
3.2.3	The Level 1 Trigger	45
3.2.4	The Complementarity of VFPS And FPS	47
4	Study of the Very Forward Proton Spectrometer	49
4.1	Trigger Tile Efficiencies	49
4.2	The Proton Beam Optics	51

4.2.1	Proton Beam Orbits	54
4.2.2	Optimisation of the Beam Optics	54
4.2.3	The Proton Beam Position Monitoring	55
4.2.4	Calibration of the Beam Position Monitor at 220 m	56
4.3	Study of Inclusive Diffraction With Tagged Proton	59
4.3.1	Kinematic Reconstruction And Resolution	60
4.3.2	Data Selection of the Reference Sample	61
4.3.3	Subsample of Events With Proton Tagged by the VFPS	65
4.3.4	Simulation of Signal And Background Processes	66
4.3.5	Inclusive Diffraction	69
4.3.6	Inclusive Diffraction With VFPS Tagged Protons	70
4.3.7	VFPS Acceptance in $x_{\mathbb{P}}$	70
4.3.8	Prospects	76
5	Diffractive Scattering of Photons Off Protons at Large Momentum Transfer	79
5.1	Reconstruction of Kinematic Variables	80
5.2	Preselection	80
5.2.1	Subtrigger Utilisation	81
5.3	Event Selection	83
5.3.1	Scattered Electron	84
5.3.2	Final State Photon Identification	84
5.3.3	Proton Dissociative System	85
5.3.4	Basic Background Rejection	85
5.3.5	Kinematic Region	88
5.4	Monte Carlo Models	88
5.4.1	Signal Process	90
5.4.2	Background Processes	91
5.5	Monte Carlo Corrections	92
5.5.1	Detector Level	92
5.5.2	Model Correction	94
5.6	Control Plots	95
5.7	Cross Sections	101
5.7.1	Acceptances	103
5.7.2	Study of Systematic Errors	103
5.7.3	γp Cross-section Extraction Method	110
5.7.4	$\sigma_{\gamma p}$ Measurement And Extraction of the α_s^{BFKL} Parameter	113
5.7.5	Summary	114
6	Conclusions	117

Chapter 1

Introduction

The present understanding of the elementary particles and their interactions is contained in the Standard Model of electroweak and strong interactions. According to the Standard Model, matter is made of point-like particles, quarks and leptons, interacting via the exchange of gauge bosons. Leptons are sensitive to the electro-weak interaction, whereas quarks in addition interact strongly. The exchange boson for the electromagnetic interaction is the photon. The weak interaction is mediated by the exchange of the massive gauge bosons W^+ , W^- and Z^0 . The weak and electromagnetic interactions are unified within the electroweak theory. Gluons are exchanged in the strong interaction, described in the quantum chromodynamics (QCD).

In high energy lepton-hadron scattering experiments, an elementary particle, the lepton, is probing the hadron, a composite particle, and thus delivers an excellent tool to investigate the hadron structure. Diffractive phenomena, which in the past have been observed in hadron-hadron scattering experiments, find an equivalent in the photon-proton interactions at the ep collider HERA. Due to the possible presence of a hard scale such as a large virtuality of the exchanged photon, Q^2 , large masses or large transverse momentum, HERA offers the opportunity to study diffraction in terms of a fundamental theory, QCD.

Diffractive processes such as $ep \rightarrow eXY$, where X and Y are hadronic systems of dissociated photon and proton, respectively, have been studied extensively at HERA this last decade, but the detailed understanding in terms of QCD remains a challenge. In top of the understanding of the diffractive dynamics itself such studies bring valuable information on possible saturation of the proton parton densities at large energy, which is directly related to the question of the unitarity of the S matrix.

Different angles of attack have been used to study diffraction at HERA, using different hard scales and inclusive, semi inclusive or exclusive final states. The present work studies two different aspects of diffraction at HERA:

- 1) The inclusive diffraction $ep \rightarrow eXp$ in the deep inelastic regime (i.e. $Q^2 > \text{few GeV}^2$), where the scattered proton is tagged in the Very Forward Proton Spectrometer (VFPS). The study of the VFPS detector, installed in 2004 in H1, and of the related data presented here constitute a first step towards the measurement of diffractive structure function using the VFPS.
- 2) The cross section measurement of the diffractive photon scattering off proton $\gamma p \rightarrow \gamma Y$ with a large momentum exchange in the t channel ($|t| \gg \Lambda_{QCD}^2$) obtained through the reaction $ep \rightarrow e\gamma Y$ measurement.

In the first study, i.e. $ep \rightarrow eXp$ in DIS regime, the Q^2 supplies a hard scale for the application of perturbative QCD. Diffractive DIS processes can be factorised into universal diffractive parton densities characteristic for the proton and a hard scattering matrix elements calculable at any order in pQCD, analogous to the factorisation in inclusive deep inelastic scattering. This approach is extended by the Resolved Pomeron Model which interprets the diffractive parton densities of the proton as the product of a pomeron flux in the proton and parton densities of the pomeron. The measured hard scattering cross section was found to be well described by the NLO DGLAP evolution equation, therefore allowing the extraction of diffractive parton distribution functions. In this work, we present the first study of the elastic diffractive scattering using data collected in the H1 experiment using the VFPS. Data were collected during the running period of years 2006-2007. The analysis gives an insight on the amount of available data, the available kinematic domain, the quality of the understanding of the data (at this early level) and the VFPS performance in terms of efficiency and acceptance.

In the second analysis, where the diffractive process $\gamma p \rightarrow \gamma Y$ is considered, the final photon is separated from the dissociative Y system by the rapidity gap. The required high transverse photon momentum ($p_T^\gamma > 2$ GeV) reflects the presence of the large momentum squared transferred at the proton vertex, $|t| > 4$ GeV², which provides the needed hard scale for the applicability of the perturbative QCD calculation, whereas $Q^2 \ll \Lambda_{QCD}^2$. This process is of particular interest as it provides a unique test of perturbative QCD prediction in the asymptotic limit of high energy given by the evolution equation called BFKL. Unlike in the diffractive vector meson production, where the products of the vector meson subsequent decay give additional multiplicity to be detected, the considered process consists of the single photon, leading to enlargement of the geometric acceptance. The cross section of this process is measured here for the first time. The kinematic region is $4 < |t| < 36$ GeV² and $175 < W < 247$ GeV, where W is the γp center of mass energy. Cross sections are measured as $\sigma(W)$ and $d\sigma/d|t|$. These results have been submitted for publication by the H1 Collaboration very recently.

This thesis is structured as follows: In chapter 2 the relevant theoretical aspects are discussed, including different Monte Carlo programs used to estimate the detector acceptance and background contributions. An introduction to the HERA collider and the H1 experiment with the emphasis on important parts for presented studies is given in chapter 3. Chapter 4 presents the study of the performance of the Very Forward Proton Spectrometer and of related data of inclusive diffraction in DIS regime. Chapter 5 presents the study and the cross section measurement of the diffractive scattering of photons at large momentum transfer.

Chapter 2

Theoretical Overview

Deep inelastic scattering (DIS) has played an important role in the understanding of the structure of the hadronic matter. Measurements at HERA, with large centre of mass energies of the ep collisions, has totally changed our vision of the proton structure, showing large densities of quarks and gluons carrying a small momentum fraction of the proton. Also the HERA experiments allow the investigation of the hadronic final state, which for the first time permits the measurement of the diffractive contribution to the proton structure functions.

In this chapter an outline of DIS is given, followed by a discussion of inclusive diffraction in the DIS regime and then by a discussion on a particular diffractive process consisting of the photon scattering off the proton with a large momentum transfer in the t channel. The theoretical aspects are discussed only to the extent which is necessary for the motivation of the presented analyses and the interpretation of the data.

2.1 Deep Inelastic Scattering

The lepton-proton deep inelastic scattering (DIS) can be written in the general way as

$$l(k) + p(p) \rightarrow l'(k') + X(p') \quad (2.1)$$

where k , p , k' and p' represent the four momentum of the incoming lepton, proton, scattered lepton and hadronic system, respectively, as illustrated in Fig.2.1. In DIS at leading order, the incoming electron interacts with the incoming proton by the exchange of a single gauge boson. In neutral current events a virtual photon (γ^*) or a Z^0 boson is exchanged, leading to an electron and the hadronic final state system X . In charged current interactions a W boson is exchanged and the final state consists of a neutrino and the hadronic system X . In the following we will consider only neutral current interactions and limit ourselves to a single photon exchange.

2.1.1 Kinematics

In order to describe the kinematics of the DIS process, the following Lorentz invariant variables are used:

- The ep centre of mass energy squared, s ,

$$s \equiv (k + p)^2 \simeq 4E_e E_p, \quad (2.2)$$

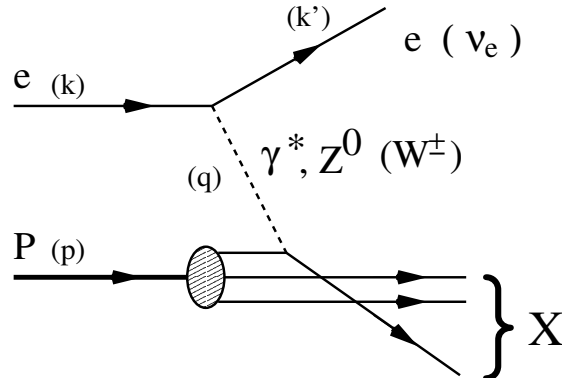


Figure 2.1: Diagram of deep inelastic electron proton scattering. The electron (carrying the four momentum vector k) interacts with the proton (p) via the exchange of a virtual gauge boson (q).

is fixed at collider experiments by the energies of the electron and proton beams, E_e and E_p , respectively.

- The negative of the square of the exchanged virtual photon four momentum, Q^2 , is defined as

$$Q^2 = -q^2 \equiv -(k - k')^2, \quad (2.3)$$

where q is the four momentum transfer of the intermediate boson. Q^2 represents the virtuality of the photon. If the photon is almost real ($Q^2 \simeq 0$), the process is referred to as photoproduction. The so called DIS regime corresponds to Q^2 greater than a few GeV^2 .

- The Björken scaling variable, x , is defined as

$$x \equiv \frac{-q^2}{2p \cdot q} \quad (2.4)$$

and in the Quark Parton Model (section 2.1.2) x can be seen as the longitudinal momentum fraction of the proton carried by the struck parton (this interpretation being valid only in a fast frame w.r.t. the proton).

- The inelasticity, y , defined as

$$y \equiv \frac{p \cdot q}{p \cdot k}, \quad (2.5)$$

corresponds in the proton rest frame to the energy fraction of the incident electron carried by the exchanged photon and transferred to the hadronic final state X .

At fixed centre of mass energy \sqrt{s} , only two of these variables are independent. When neglecting the electron and proton masses they are connected by the relation

$$Q^2 = xys. \quad (2.6)$$

In addition, the energy in the γ^*p centre of mass system, W , is given by

$$W^2 \equiv (p + q)^2, \quad (2.7)$$

which corresponds to $W^2 \simeq ys - Q^2$, neglecting the proton mass.

2.1.2 DIS Cross Section and Parton Model

The cross section for NC ep interactions can be expressed as the squared sum of the amplitudes from the γ^* and Z^0 exchanges as $\sigma_{NC} = |A(\gamma^*) + A(Z^0)|^2$. In the region of $Q^2 \ll M_{Z^0}^2$ only photon exchange contributes, resulting in a simplification of the cross section expression. In the data sample studied in the present work, the Z^0 exchange and the interference term can be neglected due to the large mass of the Z^0 boson ($M_{Z^0} \simeq 91.2$ GeV), according to the ratios of the propagator terms.

Since the DIS process has two degrees of freedom at fixed s , a complete description can be obtained by measuring the differential cross section $\frac{d\sigma}{dx dQ^2}$, as

$$\frac{d^2\sigma^{e^\pm p \rightarrow e^\pm X}(x, Q^2)}{dx dQ^2} = \frac{4\pi\alpha_{em}^2}{xQ^4} \left[\left(1 - y + \frac{y^2}{2} \right) F_2(x, Q^2) - \frac{y^2}{2} F_L(x, Q^2) \right], \quad (2.8)$$

where α_{em} denotes the electromagnetic coupling constant and F_2 and F_L two proton structure functions. The longitudinal structure function F_L is defined by the F_1 and F_2 structure functions as

$$F_L(x, Q^2) = F_2(x, Q^2) \left(1 + \frac{4M_p^2 x^2}{Q^2} \right) - 2xF_1(x, Q^2). \quad (2.9)$$

In the kinematic region of y not too close to unity, the contribution of the structure function F_L can be neglected and the cross section only depends on F_2 .

The Quark Parton Model

The momentum transfer squared, Q^2 , can be interpreted as the resolution power of the probe to reveal the proton structure.

The SLAC-MIT Collaboration in the late 1960s performing DIS measurements in the kinematic region $1 < Q^2 < 10$ GeV² for $x \simeq 0.2$, observed that F_2 shows only little Q^2 dependence but is dependent on x . This scaling invariance suggested the parton model, in which the proton consists of point-like constituents among which the proton momentum is distributed. At large Q^2 , the quarks appear as free particles inside the proton and the electron scatters elastically off one of them. The DIS cross section can thus be expressed as the incoherent sum of elastic electron-parton cross sections calculable in quantum electrodynamics, assuming massless quarks of spin 1/2. The resulting cross section is

$$\frac{d^2\sigma^{ep \rightarrow eX}}{dx dQ^2} = \sum_i \int dx e_i^2 f_i(x) \left(\frac{d^2\sigma^{eq_i \rightarrow eq_i}}{dx dQ^2} \right), \quad (2.10)$$

where e_i is the electric charge of the quark of flavour i and $f_i(x)dx = [q_i(x) + \bar{q}_i(x)]dx$ is interpreted as the probability to find a quark or an antiquark with momentum fraction in the interval $[x, x + dx]$ in the proton.

The Quark Parton Model leads to the observed scaling behaviour and the structure function F_2 is then written as

$$F_2(x, Q^2) \rightarrow F_2(x) = \sum_i e_i^2 x f_i(x), \quad (2.11)$$

If quarks and antiquarks were the only constituents of the proton, their momentum sum should be equal to unity. However, measurements revealed that this sum is equal to ~ 0.5 , the missing

momentum being carried by gluons. Moreover, by exploring a larger region in the (Q^2, x) plane, violations of the scaling behaviour mentioned above were observed at SLAC and subsequent experiments. These observations can not be interpreted within the QPM, but can be understood in the framework of quantum chromodynamics.

2.1.3 Quantum Chromodynamics

The partons in the proton and their interactions are generally described in terms of quantum chromodynamics (QCD), which is the field theory of the strong interaction, based on the $SU_C(3)$ gauge group.

In QCD the proton is built from quarks which are spin 1/2 fermions. They are bound together by gluons which are the massless spin 1 gauge bosons of QCD. The colour (red, blue, green) corresponds to a new degree of freedom carried by the quarks and, in contrast to QED, also by the gauge bosons. This leads to a self coupling of the gluons and hence to fundamental differences between QCD and QED. Opposite to the effect of α_{em} seen in the electromagnetic interactions, the effective strong coupling constant, $\alpha_s(\mu^2)$, where μ^2 is the scale parameter, gets smaller at smaller distances, corresponding to higher μ^2 . For a scale μ large enough (whose value should be determined experimentally) cross sections are calculable as a perturbative expansions in α_s , and quarks and gluons are considered as asymptotically free. At large distances (small μ^2) the coupling strength of α_s gets large and the perturbation theory is no longer applicable. This long range effect is responsible for the confinement of partons in bound states, the hadrons.

Factorisation in QCD

The theorem of hard scattering factorisation in QCD has been proven [41] in the kinematic limit of $s \rightarrow \infty$, $Q^2 \rightarrow \infty$ and x fixed. It states that the short range part, i.e. perturbatively calculable aspects of a physical process, can be separated from long range aspects (i.e. the partonic content of the interaction of hadrons), for which the perturbation theory is not applicable:

$$d\sigma^{ep \rightarrow eX}(x, Q^2) = \sum_i f_i(x, Q^2, \mu_f^2) \otimes d\hat{\sigma}^{ei}(x, Q^2/\mu_f^2), \quad (2.12)$$

where μ_f is the factorisation scale which corresponds to the energy scale above which parton emissions from the quark are computed in perturbative QCD (as illustrated in Fig. 2.2). Parton emissions with $k_T^2 < \mu_f^2$ are absorbed into the universal parton distribution functions f_i , which depend on the factorisation scale μ_f . $\hat{\sigma}^{ei}$ are the partonic cross sections, calculable in perturbative QCD to a given order in α_s .

2.1.4 Evolution of Parton Distribution Functions

The parton density functions cannot be calculated from first principles, and have to be extracted from the experimental data. However, perturbative QCD calculations predict the evolution of parton densities with the factorisation scale, in the form of differential equations, once the parton distributions are known for a certain starting scale (i.e. $\mu_f^2 = Q_0^2$). To solve these equations it would in principle be necessary to include all terms to all orders in the perturbative series. However, approximations are available, neglecting different terms in the perturbation series.

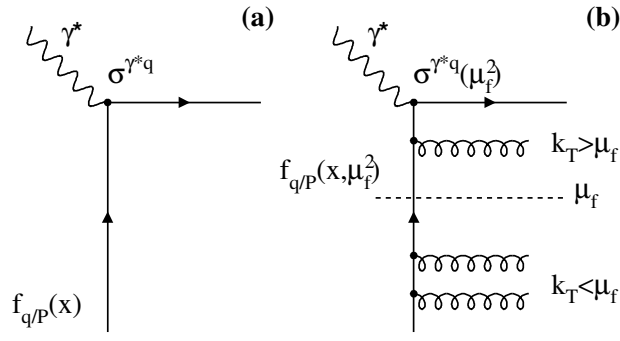


Figure 2.2: The factorisation of hard and soft contributions: lowest order in α_s for the photon-quark scattering (a); next-to-leading order in α_s with additional parton emission.

The DGLAP Evolution Equations

The DGLAP equations [42] describe the evolution of quark and gluon distributions, denoted by $q_i(x, Q^2)$ and $g(x, Q^2)$, respectively, from a starting scale Q_0^2 to an arbitrary scale $Q^2 > Q_0^2$:

$$\frac{\partial q_i(x, Q^2)}{\partial \ln Q^2} = \frac{\alpha_s(Q^2)}{2\pi} \int_x^1 \frac{dz}{z} \left[\sum_j q_j(z, Q^2) P_{ij}\left(\frac{x}{z}\right) + g(z, Q^2) P_{ig}\left(\frac{x}{z}\right) \right], \quad (2.13)$$

$$\frac{\partial g(x, Q^2)}{\partial \ln Q^2} = \frac{\alpha_s(Q^2)}{2\pi} \int_x^1 \frac{dz}{z} \left[\sum_j q_j(z, Q^2) P_{gj}\left(\frac{x}{z}\right) + g(z, Q^2) P_{gg}\left(\frac{x}{z}\right) \right]. \quad (2.14)$$

The perturbatively calculable splitting functions $P_{ij}(z)$ describe parton emission. They give the probability for parton branchings (Fig. 2.3) off an initial parton, where the radiated parton is emitted with fractional momentum $(1 - z)$, leaving the initial parton with the fraction z of its momentum. At leading order they are given by

$$P_{qq}(z) = \frac{4}{3} \frac{1+z^2}{1-z}, \quad P_{qg}(z) = \frac{z^2 + (1-z)^2}{2}, \quad (2.15)$$

$$P_{gq}(z) = \frac{4}{3} \frac{1+(1-z)^2}{z}, \quad P_{gg}(z) = 6 \left(\frac{z}{1-z} + \frac{1-z}{z} + z(1-z) \right).$$

Keeping only the effect of gluon emission P_{gg} approximated by a $1/z$ dependence, one can solve these equations order by order. Summing them up to order n , the obtained series lead to the so called double logarithmic approximation for parton densities

$$Q^2 p(x, Q^2) \sim \left(\bar{\alpha}_s \ln \frac{1}{x} \ln \frac{Q^2}{Q_0^2} \right)^n, \quad (2.16)$$

where $p(x, Q^2)$ refers to quark density, $q(x, Q^2)$, or to gluon density, $g(x, Q^2)$, and $\bar{\alpha}_s = 3\alpha_s/\pi$. It resums ladders (see Fig. 2.4), in which there is a strong ordering both in the transverse and longitudinal momenta along the ladder,

$$k_{T,1}^2 \ll \dots \ll k_{T,i}^2 \ll k_{T,i+1}^2 \dots \ll Q^2; \quad (2.17)$$

$$x \ll \dots \ll x_{i+1} \ll x_i \ll \dots \ll 1,$$

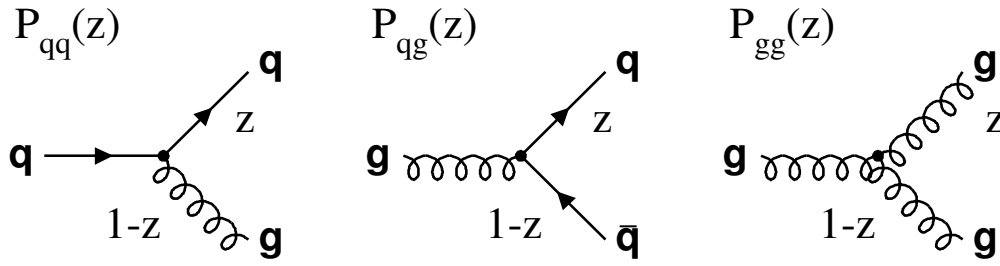


Figure 2.3: Diagrams of the splitting functions $P_{ij}(z)$ for the processes $q \rightarrow q'g$, $g \rightarrow q\bar{q}$ and $g \rightarrow gg$.

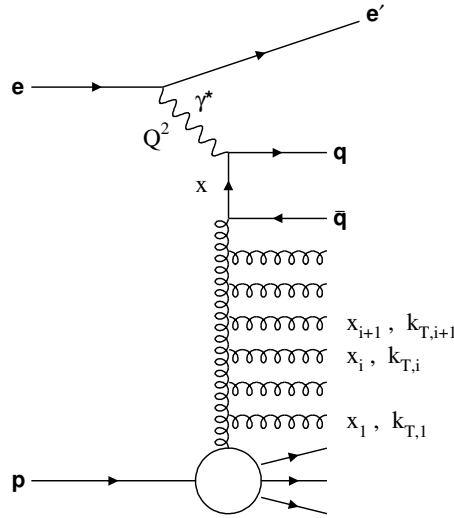


Figure 2.4: The ladder diagram of the QCD parton evolution of the structure function F_2 . The longitudinal and transverse momenta of emitted gluons are labeled x_i and $k_{T,i}$, respectively.

respectively.

The above arguments are relevant in the limit where both $1/x$ and Q^2/Q_0^2 are large. If $1/x$ is not large, we can limit ourselves to the leading logarithmic approximation (LLA) of resumming only terms of the type $(\bar{\alpha}_s \ln \frac{Q^2}{Q_0^2})^n$, in which there is a strong ordering in the transverse momenta of the emitted gluons (taken relative to the motion of the initial parton before gluon radiation) and a simple ordering in their longitudinal momenta,

$$k_1^2 \ll \dots \ll k_i^2 \ll k_{i+1}^2 \dots \ll Q^2; \quad (2.18)$$

$$1 > \dots > x_i > x_{i+1} > \dots > x.$$

This LLA of DGLAP is usually used to fit F_2 measurements for the extraction of parton densities.

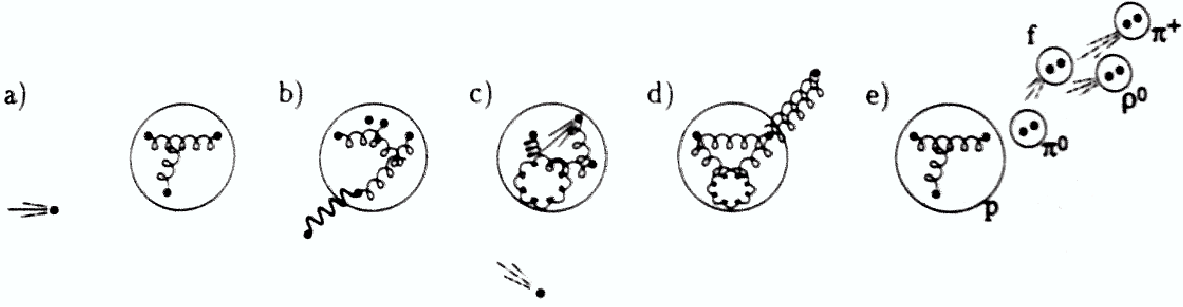


Figure 2.5: An example of the hadronisation process.

The BFKL Evolution Equations

In the limit of large $1/x$ and Q^2 of the order of Q_0^2 , terms in $\bar{\alpha}_s \ln \frac{1}{x}$ will dominate the perturbative serie equation. This corresponds to relaxing the strong ordering in k_T^2 , but imposing it in x [47]. Such a LLA in $1/x$, summing up terms in $(\alpha_s \ln \frac{1}{x})^n$, was proposed by Balitzky, Fadin, Kuraev and Lipatov [15], referred as the BFKL equations.

A general form can be given to these approaches, rewriting eq. (2.16) as

$$q(x, Q^2) = q^0(x, Q^2) + \int_x^1 \frac{dz}{z} \int^{Q^2} dk^2 \mathcal{K}(Q^2, k^2) q\left(\frac{x}{z}, k^2\right), \quad (2.19)$$

where the kernel $\mathcal{K}(Q^2, k^2)$ is given in the LLA DGLAP case by $\mathcal{K}(Q^2, k^2) = \frac{\bar{\alpha}_s}{Q^2}$, which is valid for $Q^2 \gg k^2$. The kernel expression in LLA BFKL is more complicated and is not given here.

2.1.5 Hadronisation

Due to the phenomenon of confinement, free states exist only as colour neutral states: they are the hadrons. Hadrons are formed by soft interactions that can be factorised in time to the hard interaction. In the example of a DIS scattering shown in Fig. 2.5, a high energy (in the centre of mass system) electron approaches a proton (a). A single quark within the proton receives a substantial momentum from the electron via the exchange of a photon (b) and both particles recoil (c). As the quark leaves the remnant of the proton (d), the gluonic field between the recoiled quark and other quarks of the proton remnant fluctuates into $q\bar{q}$ pairs and these quarks combine to make colour neutral objects (e). The hadronisation process is theoretically poorly understood as perturbative QCD can not be applied. Instead, phenomenological models, as the Lund String Model, are used to describe the hadronic final state of the interactions.

In the Lund String Model a massless relativistic string is used to model the QCD field between coloured objects. The endpoints of the string are identified as the quark and the antiquark. The final state hadrons observed in high energy collisions stem from the breakup of the force field. As the q and \bar{q} move apart, the potential energy stored in the string increases and the string may break by the production of a new $q'\bar{q}'$ pair, with colour values such that the system splits into two colour-singlet systems $q\bar{q}'$ and $q'\bar{q}$. The string break-up process is assumed to proceed until only on-mass-shell hadrons remain, each hadron corresponding to a small piece of string with a quark in one end and an antiquark in the other.

2.2 Inclusive Diffractive Scattering

The term diffractive scattering originates from observations in hadronic interactions. They consist in a generalisation of the elastic scattering $h_1+h_2 \rightarrow h_1+h_2$ to the case of $h_1+h_2 \rightarrow h_3+h_4$ where h_3 (h_4) are hadronic state of invariant mass equal or close to h_1 (h_2), i.e. $M_{h_3}, M_{h_4} \ll W$. In the interaction a colourless pseudo particle (reggeon or pomeron) is exchanged between the hadrons in the t channel. The reaction is characterised by a large, non exponentially suppressed rapidity gap in the final state¹,

$$\frac{dN}{d\Delta\eta} \sim \text{constant}, \quad (2.20)$$

where, in the relativistic limit, the pseudo-rapidity of a particle emerging from the interaction under the polar angle θ is

$$\eta = -\ln \tan \frac{\theta}{2}. \quad (2.21)$$

To describe such reactions, the Regge phenomenology was introduced in 1960's (the preQCD era) and describes soft hadron-hadron interactions at high energy as mediated by meson resonances which have a linearly correlated spin J and mass squared, m^2 . A straight correlation is observed between $\alpha = J$ and $t = m^2$, and is known as the Regge trajectory

$$\alpha(t) = \alpha(0) + \alpha' \cdot t, \quad (2.22)$$

which extrapolates to negative values of t . The full calculation of a cross section should involve all Regge trajectories that can be exchanged in a given reaction, but two trajectories are sufficient to describe the high energy dependence of hadron-hadron and photon-hadron cross sections (Fig. 2.6). The Reggeon trajectory with an intercept $\alpha_{\mathcal{R}}(0) = 0.55$ and slope $\alpha'_{\mathcal{R}} \simeq 1 \text{ GeV}^{-2}$, corresponding to a meson exchange, describes W dependence of the cross section for small W . The pomeron trajectory with $\alpha_{\mathcal{P}}(0) = 1.08$ and slope $\alpha'_{\mathcal{P}} \simeq 0.25 \text{ GeV}^{-2}$ was introduced to describe the slight growth of the cross section at high energy (above $\sim 10 \text{ GeV}$). The ability of Regge theory to describe photon-hadron interactions results from photon fluctuations into a $q\bar{q}$ state allowing hadron-like interactions.

2.2.1 Diffraction in the DIS regime

In ep collisions, diffractive events of the type

$$e(k) + p(p) \rightarrow e(k') + X(p_X) + Y(p_Y) \quad (2.23)$$

have been observed in deep inelastic scattering at HERA. They consist of two distinct final state systems separated by a large (i.e. $\Delta\eta > 2$) rapidity gap: the dissociation system of the photon, X , and the scattered proton or (as shown in Fig. 2.7) a low mass dissociated system, Y .

The high energy of HERA beams offers the opportunity to try to understand the diffractive exchange taking place here in terms of a fundamental theory, QCD, in the perturbative regime.

¹as opposed to DIS, where the gap is exponentially suppressed, $\frac{dN}{d\Delta\eta} \sim e^{-\Delta\eta}$.

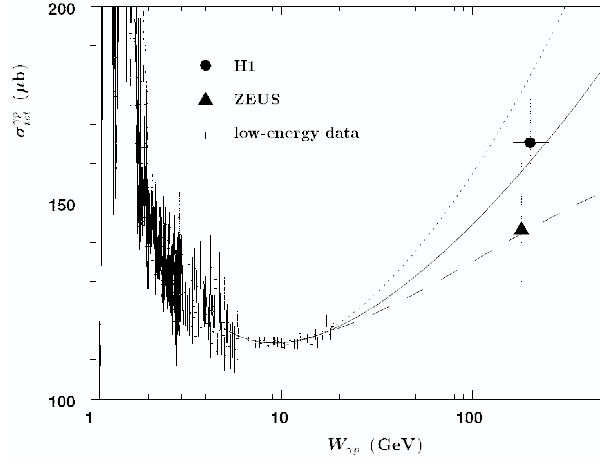


Figure 2.6: The total photon-proton cross section as a function of the centre of mass energy $W_{\gamma p}$ with Regge-type parameterisations.

Kinematics

The kinematic variables used to describe diffractive processes are shown in Fig. 2.7. The definitions of kinematic variables as introduced in the section 2.1.1 remain valid in diffraction, and in addition several new variables are introduced.

Let the invariant masses and four-vectors of the two dissociative systems be M_X , M_Y and p_X , p_Y , respectively. The new kinematic variables are

- the momentum fraction $x_{\mathbb{P}}$ of the proton carried by the pomeron, defined as

$$x_{\mathbb{P}} \equiv \frac{q \cdot (p - p_Y)}{q \cdot p}; \quad (2.24)$$

- the elasticity of the γp interaction, which can be seen as the energy fraction of the exchanged photon transferred to the final state photon, is given by $1 - y_{\mathbb{P}}$, where

$$y_{\mathbb{P}} \equiv \frac{p \cdot (q - p_X)}{p \cdot q}; \quad (2.25)$$

- the momentum transfer t at the proton vertex, given by

$$t \equiv (p - p_Y)^2 = (q - p_X)^2; \quad (2.26)$$

- the momentum fraction β of the pomeron carried by the interacting quark

$$\beta \equiv \frac{-q^2}{q \cdot (p - p_Y)}, \quad (2.27)$$

such that $\beta = x/x_{\mathbb{P}}$, showing the analogy between β and x in a deep inelastic scattering.

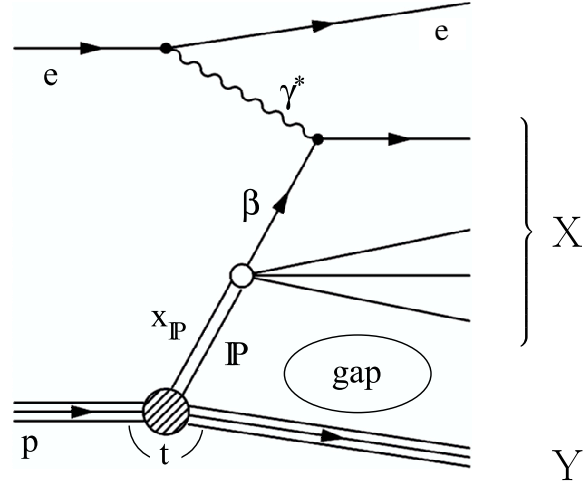


Figure 2.7: Diagram of the diffractive scattering in DIS with the kinematic variables.

2.2.2 Diffractive Structure Function And the Factorisation

Diffractive events can be used to study the pomeron structure in a similar way to the study of the proton structure with inclusive DIS events. For inclusive diffractive scattering a diffractive structure function $F_2^{D(5)}$ can be introduced, similarly to F_2 in the inclusive DIS case. The inclusive diffractive cross section, in the limit where the contribution of the longitudinal photon cross section can be neglected and for $Q^2 \ll M_{Z^0}^2$, is written as

$$\frac{d^5 \sigma^{ep \rightarrow eXY}}{dx_P d\beta dQ^2 dM_Y dt} = \frac{4\pi\alpha_{em}^2}{\beta Q^4} \left(1 - y + \frac{y^2}{2}\right) F_2^{D(5)}(x_P, \beta, Q^2, M_Y, t). \quad (2.28)$$

If the outgoing dissociated system of the proton Y is not detected (i.e. escaping through the beam pipe), M_Y is not directly measured. In the inclusive elastic diffraction $ep \rightarrow eXp$ case, when the scattered proton is not measured by the proton spectrometers, the t variable is not well measured. In these cases, the diffractive structure function $F_2^{D(5)}$ is integrated over M_Y and t and we define

$$F_2^{D(3)}(\beta, Q^2, x_P) = \int_{M_p}^{M_Y^{max}} dM_Y \int_{t_{min}(M_Y)}^{t_{max}} dt F_2^{D(5)}(\beta, Q^2, x_P, M_Y, t). \quad (2.29)$$

In the following discussion we limit ourselves to the elastic case.

As inclusive DIS processes can be described in terms of universal parton densities of the proton and parton-parton scattering matrix elements, it was proven [43] that diffractive processes $ep \rightarrow eXp$ can be factorized into universal partonic cross sections, $\hat{\sigma}^{ei}$ (the same as in DIS), with diffractive parton distributions, f_i^D . These diffractive parton distributions (DPDFs) represent the probability distributions for a parton i in the proton, under the additional constraint that the proton remains intact, with particular values of x_P and t . For Q^2 large enough and for fixed x , x_P and t , the cross section can be written as

$$d\sigma^{ep \rightarrow eXp}(\beta, Q^2, x_P, t) = \sum_i f_i^D(\beta, Q^2, x_P, t) \otimes \hat{\sigma}^{ei}(\beta = x/x_P, Q^2) \quad (2.30)$$

and the diffractive parton distributions obey the DGLAP evolution equations.

Resolved Pomeron Model

A main obstacle for the experimental determination of the diffractive parton distributions is the fact that it depends on five (three, if integrated over t and M_Y) independent variables. To further reduce the number of dimensions, the application of the Regge phenomenology of soft high energy interactions is used in the following. This assumption allows to apply the concept of a resolved pomeron model with a partonic structure invariant under changes in $x_{\mathbb{P}}$ and t . One can then visualize diffractive DIS as the proton emitting a pomeron, which then undergoes a hard interaction with the photon, resolving the partonic structure of the pomeron. The diffractive parton distributions hence are assumed to factorise into a pomeron flux in the proton, $f_{\mathbb{P}/p}$ and the pomeron parton distributions $f_i^{\mathbb{P}}$,

$$f_i^D(\beta, Q^2, x_{\mathbb{P}}, t) = f_{\mathbb{P}/p}(x_{\mathbb{P}}, t) \cdot f_i^{\mathbb{P}}(\beta, Q^2). \quad (2.31)$$

The pomeron flux factor describes the probability of finding a pomeron in the proton as a function of $x_{\mathbb{P}}$ and t . The diffractive structure function then factorises to $F_2^{D(4)}(\beta, Q^2, x_{\mathbb{P}}, t) = f_{\mathbb{P}/p}(x_{\mathbb{P}}, t) \cdot F_2^{\mathbb{P}}(\beta, Q^2)$, where $F_2^{\mathbb{P}}$ denotes the pomeron structure function which describes the parton distributions of the pomeron,

$$F_2^{\mathbb{P}}(\beta, Q^2) = \sum_i e_i^2 \beta f_i^{\mathbb{P}}(\beta, Q^2), \quad (2.32)$$

on which the DGLAP evolution will be applied.

For F_2^D measurements at high $x_{\mathbb{P}}$ values ($x_{\mathbb{P}} \gtrsim 0.01$) it is necessary to consider contributions from the sub-leading Regge trajectory, the reggeon, on top of the pomeron exchange, such that

$$F_2^D = f_{\mathbb{P}/p} \cdot F_2^{\mathbb{P}} + f_{\mathbb{R}/p} \cdot F_2^{\mathbb{R}}. \quad (2.33)$$

In practice, for the parameterisation of the parton densities of the reggeon, the pion structure functions are used. The $x_{\mathbb{P}}$ and t dependences of the pomeron and the reggeon flux factors are parameterised using the Regge inspired form of

$$f_{\mathbb{P}/p}(x_{\mathbb{P}}, t) = A_{\mathbb{P}} \cdot \frac{e^{B_{\mathbb{P}}t}}{x_{\mathbb{P}}^{2\alpha_{\mathbb{P}}(t)-1}}, \quad f_{\mathbb{R}/p}(x_{\mathbb{P}}, t) = A_{\mathbb{R}} \cdot \frac{e^{B_{\mathbb{R}}t}}{x_{\mathbb{P}}^{2\alpha_{\mathbb{R}}(t)-1}} \quad (2.34)$$

2.2.3 Recent Results on the Partonic Structure of the Pomeron

The H1 Collaboration has recently performed a QCD analysis [44] of the inclusive diffractive cross section based on data collected during the first phase of HERA activity (years 1997-2000). Event candidates for the reaction $ep \rightarrow eXY$ were selected by the presence of a large rapidity gap between the X and Y systems. It should be noted that it includes a contribution of events with a proton dissociated system of mass $M_Y < 1.6$ GeV. The $F_2^{D(3)}$ structure function was measured in the region of $x_{\mathbb{P}} < 0.05$ and $|t| < 1$ GeV². DPDFs and their uncertainties were determined from a next-to-leading order DGLAP QCD analysis of the Q^2 and β dependences of the cross section in the kinematic range $8.5 < Q^2 < 1600$ GeV² and $\beta \leq 0.8$. The DPDFs were modeled in terms of a light flavour singlet distribution $\sum(z)$ consisting of u , d and s quarks and anti-quarks and of gluon distribution $g(z)$, parameterised at Q_0^2 as

$$z f_i(z, Q_0^2) = A_i z^{B_i} (1-z)^{C_i}, \quad (2.35)$$

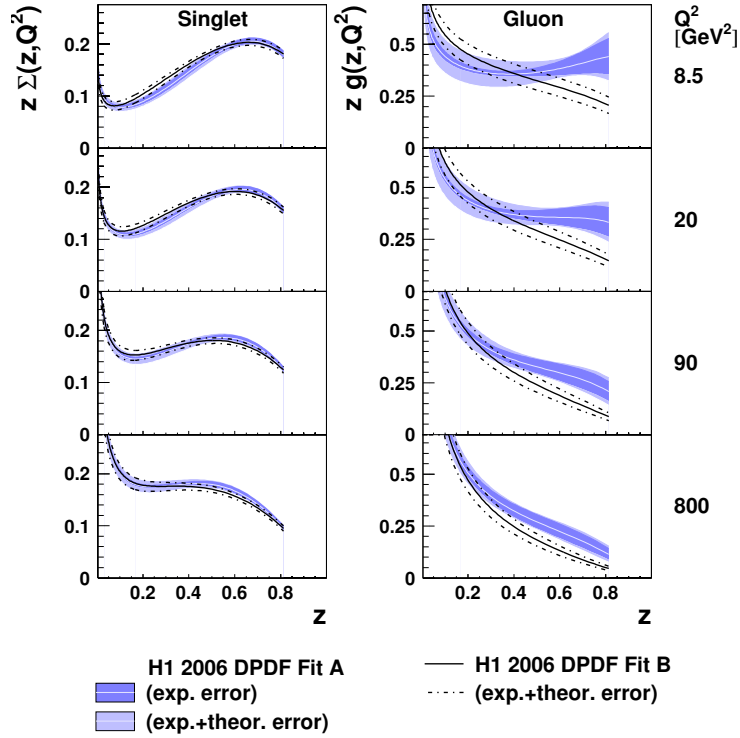


Figure 2.8: The total quark singlet and gluon distributions obtained from the NLO QCD H1 2006 DPDF Fit A compared to H1 2006 DPDF Fit B.

with the $x_{\mathbb{P}}$ and t dependences parameterised according to eq. (2.34). The measured $F_2^D Q^2$ dependence is well described by a NLO DGLAP evolution. The two different results of the QCD fits (each describing the data), are depicted in Fig. 2.8. The H1 2006 DPDF Fit B is performed with the parameter C_g , which determines the high z behaviour, set to zero and was motivated by a weak sensitivity of F_2^D to the gluon density in that z region. The gluon distribution carries an integrated fraction of around 70% of the exchanged momentum in the measured range. The extracted effective pomeron intercept $\alpha_{\mathbb{P}}(0) = 1.118 \pm 0.008(\text{exp})$.

The measurement of the elastic diffractive events $ep \rightarrow eXp$ by the H1 Collaboration [40] in the range $0.08 < |t| < 0.5 \text{ GeV}^2$ and $2 < Q^2 < 50 \text{ GeV}^2$, using Roman pot detectors to measure the scattered protons in the beam pipe, shows that the differential cross section has a dependence of approximately

$$d\sigma^{ep \rightarrow eXp}/dt \propto e^{6t} \quad (2.36)$$

for $x_{\mathbb{P}} \lesssim 0.01$, independently of $x_{\mathbb{P}}$, β and Q^2 within the uncertainties. In the region $x_{\mathbb{P}} < 0.05$, the ratio of the diffractive cross section as measured by the large rapidity gap, $\sigma^{ep \rightarrow eXY}$, to the elastic diffractive cross section is,

$$\frac{\sigma^{ep \rightarrow eXY}(M_Y < 1.6 \text{ GeV})}{\sigma^{ep \rightarrow eXp}} = 1.23 \pm 0.03(\text{stat}) \pm 0.16(\text{syst}), \quad (2.37)$$

independently on the β , Q^2 and $x_{\mathbb{P}}$ within uncertainties.

2.3 Diffractive Scattering of Photons with Large Momentum Transfer

In the previous sections we described diffractive ep processes in the DIS regime within perturbative QCD with the hard scale given by the high photon virtuality. The evolution from the soft scale at the proton vertex, i.e. the proton mass, to the hard scale Q^2 is found to be well described by the NLO DGLAP approach. We will now discuss a totally different case where the hard scale is provided by large values of $|t|$, the four momentum transfer squared at the proton vertex, such that the pQCD calculations can be applied in the photoproduction regime ($Q^2 \sim 0$).

Experimentally the easiest cases are exclusive vector meson production and photon scattering:

$$\gamma p \rightarrow VM Y, \quad (2.38)$$

where $VM = \gamma, \rho, \omega, \varphi, J/\psi$ or Υ and Y is the hadronic system of the proton remnants. Here again the diffractive character is signed by the presence of a large gap in rapidity between the VM and the hadrons of the Y system.

These processes can be studied at HERA through the reaction $ep \rightarrow e VM Y$ but we'll consider directly the γp interaction, factorising out the photon flux coming from the electron beam. We note that the $1/Q^4$ term in the expression of the differential ep cross section (i.e. eq. (2.8)) implies that interactions are dominated by the photoproduction regime, in which electrons emit almost real photons. The ep and γp cross sections are related by

$$\frac{d^2\sigma^{ep}}{dydQ^2} = \sigma_{\gamma p}(ys)\Gamma(y, Q^2), \quad (2.39)$$

where $\Gamma(y, Q^2)$ is the photon flux, which can be calculated using an improved form of the Weizsäcker-Williams approximation for the case of quasi-real photons [11] (see section 5.7.3).

In the present case, the hard scale is present both at the proton and at the photon vertices (see Fig. 2.9a). Large $|t|$ values imply large transverse momentum for the Y system and also for the VM . We would therefore expect no k_T ordering in the QCD description of the colourless exchange and therefore that the process would not satisfy the DGLAP approach conditions. On the contrary, we can expect a strong ordering in $1/x$ as the colour singlet exchange has to connect a fast moving proton (w.r.t. the detector frame) to a photon moving in the opposite direction. Such processes in the HERA kinematic conditions are therefore expected to be described by the BFKL approach. Several measurements of ρ, φ and J/ψ production at large $|t|$ [17, 18] were found to be well described by LLA BFKL predictions.

In the present work we study the case of $VM = \gamma$, i.e. the photon scattering at large $|t|$:

$$\gamma p \rightarrow \gamma Y, \quad (2.40)$$

whose cross section has never been measured so far at high energy. Relative to vector meson production, the cross section is suppressed by the electromagnetic coupling of the $q\bar{q}$ pair to the final state photon. In the other hand, diffractive γp scattering has the advantage of being completely calculable in perturbative QCD, as opposed to vector mesons, where the transition from the $q\bar{q}$ pair to the final vector meson is modeled. The only non-perturbative component resides in the factorisable parton density functions of the proton.

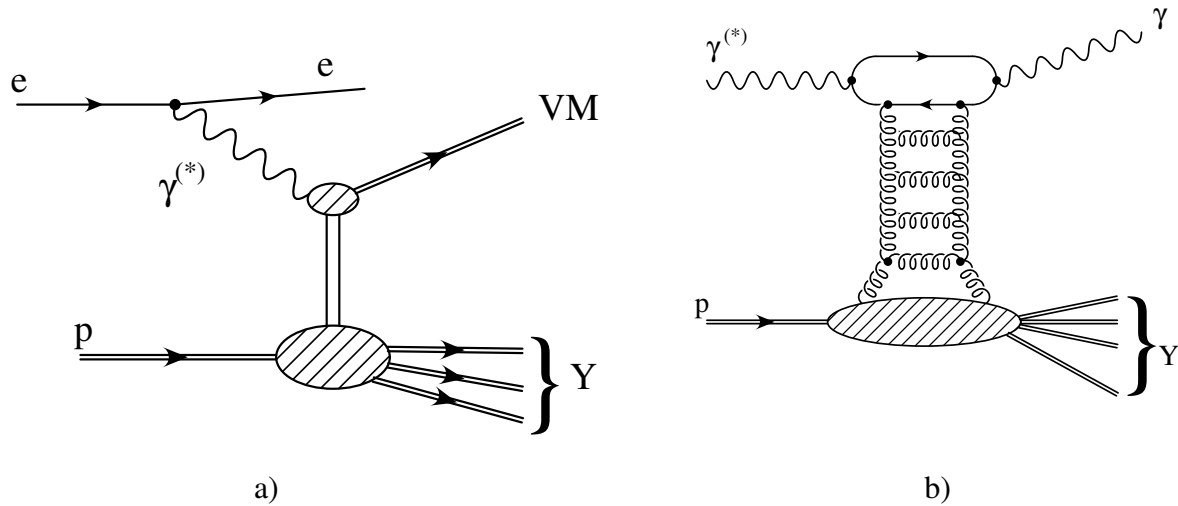


Figure 2.9: The diffractive scattering of photons at high $|t|$ described by introducing the BFKL ladder.

The experimental signature of this process is also very clear. Important is the very large rapidity gap between the photon and the hadronic Y system. The extension of the angular acceptance corresponds to small x , i.e. the optimal region of BFKL predictions.

The idea to use this process as a test for pQCD is discussed in [8–10]. The measured $\gamma p \rightarrow \gamma Y$ cross section presented in chapter 5 is compared to the predictions of Forshaw et al. [5], based on calculations [9, 10] of the BFKL dynamics and computed in the leading log approximation. The γp interaction is seen (see Fig. 2.9b) as the interaction between the photon and one parton, q , contained in the proton, and

$$\frac{d\sigma^{\gamma p}}{dx dp_T^2} = \left[\frac{81}{16} g(x, \mu) + q(x, \mu) \right] \frac{d\sigma^{\gamma q}}{dp_T^2}, \quad (2.41)$$

where p_T is the transverse momentum of the scattered photon and μ is the factorisation scale. The only kinematic dependences to be considered here are the γq centre of mass energy squared, \hat{s} , related to the γp centre of mass energy W by $W^2 = \hat{s}/x$ and the transverse momentum of the scattered photon, p_T , which in a good approximation is $|t| = p_T^2$.

The γq interaction can be seen in the proton rest frame as a sequence of three steps:

- 1) the fluctuation of the incoming photon into a $q\bar{q}$ pair at a long distance from the proton target;
- 2) the $q\bar{q}$ pair is then involved in a hard interaction with the parton q via the exchange of a colour singlet state;
- 3) the final $q\bar{q}$ pair annihilates into a real photon.

In the leading logarithmic approximation, the colour singlet exchanged is modeled by the effective exchange of a gluon ladder.

Due to the very low Q^2 values, the incoming photon may be considered as only transversally polarised. The final state photon being real, only the non helicity flip amplitude, A_{++} , is

considered and

$$\frac{d\sigma^{\gamma q}}{dp_T^2} \approx \frac{|A_{+++}|^2}{16\pi\hat{s}^2}. \quad (2.42)$$

The amplitude A_{+++} , calculated in LLA BFKL, only depends on α_s , which is considered as non running here and referred in the following as α_s^{BFKL} .

In the BFKL approach, the transverse momentum of the final state photon is entirely transferred by the gluon ladder to the struck parton in the proton. The hadronic final state Y can then be seen as containing a jet, originating from the struck parton, and the rest of the proton. Because the struck parton is the most transverse among the proton remnants, it is the closest in rapidity to the scattered photon. The separation in rapidity between the struck parton and the scattered photon is given by $\Delta\eta \simeq \log(\hat{s}/p_T^2)$.

In the asymptotic approximation of calculations [5]

$$\sigma_{\gamma p}(W) \sim W^{4\omega_0}, \quad (2.43)$$

where

$$\omega_0 = \frac{3\alpha_s^{BFKL}}{\pi} 4 \ln 2. \quad (2.44)$$

The power of the W distribution, i.e. the pomeron intercept, is affected only by the choice of α_s^{BFKL} . The LLA BFKL also predicts an approximate power-law behaviour for the t -dependence of the form

$$\frac{d\sigma}{dt} \sim |t|^{-n}, \quad (2.45)$$

where n depends on the value of α_s^{BFKL} .

2.4 Simulation of Physics Processes

Simulating processes of high energy physics with Monte Carlo techniques is a way to generate events according to theoretical distributions and compare data from an experiment to theoretical predictions. The corresponding programs are Monte Carlo event generators (MC).

A particular physics process is generated by a MC which randomly selects the values of kinematic variables, based on the cross section of this process. Final state particles with four vector information are then built according to the generated kinematics. When the final particles are partons, a fragmentation and hadronisation simulations are required to evolve the system into hadrons. A statistics of several times the luminosity of the real data is generated in order to avoid statistical fluctuations.

After the four vectors of final state particles are generated, particles are propagated to a detailed simulation of the H1 detector response and simulated events are processed through the same H1 reconstruction chain as the real data. Experimental cuts on the reconstructed quantities can then be imposed to simulated events, so that theoretical distributions can be compared to distributions of data.

In this section the main event generators used in the two analyses in this thesis are presented and the H1 simulation and reconstruction process is briefly described.

2.4.1 The RAPGAP Event Generator

The RAPGAP [2] event generator was used for the VFPS study (chapter 4), to generate inclusive diffractive electron proton scattering in the DIS regime as well as the inclusive deep inelastic scattering.

RAPGAP uses the (D)PDF at the leading order in α_s , assuming for diffraction the resolved pomeron model. Higher order QCD effects are modeled using initial and final state parton showers in the leading log approximation. Real photon emission from either the incoming or the scattered electron can have large effects on the reconstruction of the kinematic variables. Such QED radiative effects are simulated with the HERACLES module [36], which is used to generate the $e\gamma^*e$ vertex including photon emission from the incoming and outgoing electron as well as virtual corrections. The Lund String Model is used for the hadronisation, as implemented in the JETSET module [37].

As input for the diffractive events, the diffractive parton distributions [44] from the H1 Collaboration were used, labeled as 'H1 2006 DPDF Fit B', briefly described in section 2.2.3. The simulation of the inclusive non-diffractive contribution is based on the 'H1 2000 LO' [33] parton densities of the proton.

2.4.2 The HERWIG Event Generator

The HERWIG Monte Carlo program [39] was used to simulate the diffractive high $|t|$ photon scattering. Simulation of the process is based on the leading logarithmic approximation of the BFKL prediction [5], as discussed previously in section 2.3. At leading logarithmic accuracy, two independent parameters need to be set in the calculation: the value of α_s and the scale which defines the leading logarithms, the value of W_0 . In exclusive production of vector mesons the scale parameter is chosen to be half of the vector meson mass. In the case of diffractive photon scattering the unknown scale translates into an uncertainty of the normalisation of the cross section.

2.4.3 H1 Detector Simulation And Reconstruction

The output of the MC event generator - final state particles with the four vector information - is propagated in the H1 detector simulation, where interactions of particles with the detector components are simulated. From the simulated interactions and the resulting ionisations and energy depositions, the detector response is calculated. This is done in the H1SIM program package, which handles the full simulation of the H1 detector, including the forward region with the beam pipe and magnet settings up to 220 m, which is essential for the simulation of the VFPS detector. The result of the detector simulation is given in the same format as the real data. The simulated detector response is taken as input for the reconstruction procedure.

Chapter 3

H1 Experiment at HERA

HERA (Hadron-Elektron Ring Anlage) is an electron proton collider located at DESY (Deutsches Elektronen Synchrotron) laboratory in Hamburg, Germany. The data taking took place between 1992 and 2007. During the years of 1999 - 2007 (relevant for analyses presented in this thesis), electrons or positrons with an energy of $E_e = 27.6$ GeV were collided with protons with an energy $E_p = 920$ GeV, leading to an energy in the ep centre of mass of 319 GeV. HERA electron and proton storage rings (see Fig. 3.1) have a circumference of 6.3 km and meet at the two points, where the ZEUS and H1 experiments are located. Each rings is equipped with magnets and accelerating cavities.

The HERA Facility

Electrons are first preaccelerated in a LINAC facility to an energy of 500 MeV and then injected in DESY-II machine and accelerated up to 7.5 GeV. Up to 60 bunches are then filled and stored in PETRA-II facility and further accelerated to 12 GeV. Four such fillings are injected into the HERA-e ring and accelerated up to their colliding energy.

Free protons are produced by passing negatively charged hydrogen atoms H^- , accelerated up to an energy of 50 MeV in the H-LINAC, through a stripping foil where the ions loose their two electrons. Subsequently they are accelerated up to an energy of 7.5 GeV in DESY-III and injected into the PETRA-II storage ring. Here, up to 70 proton bunches are accumulated and accelerated up to 40 GeV. Four PETRA-II fillings are injected into the HERA-p ring and accelerated up to the final colliding energy.

Each of the electron and proton fills contains up to 220 bunches of 10^{10} to 10^{11} particles, with a crossing frequency of 10.4 MHz, corresponding to a crossing time interval of 96 ns. The performance of the collider is characterised by the luminosity. The instantaneous luminosity depends on the bunch crossing frequency, f , number of particles N_e and N_p in the electron and proton bunches and the collimation of the beams in the transverse directions σ_x and σ_y as

$$\mathcal{L} = \frac{f N_e N_p}{4\pi \sigma_x \sigma_y} \text{ cm}^{-2} \text{ s}^{-1}. \quad (3.1)$$

The number of expected interactions for a given process, N , is proportional to the integrated luminosity $L = \int \mathcal{L} dt$ over the data taking time, t , and is related to the cross section σ of the process as

$$N = L\sigma. \quad (3.2)$$

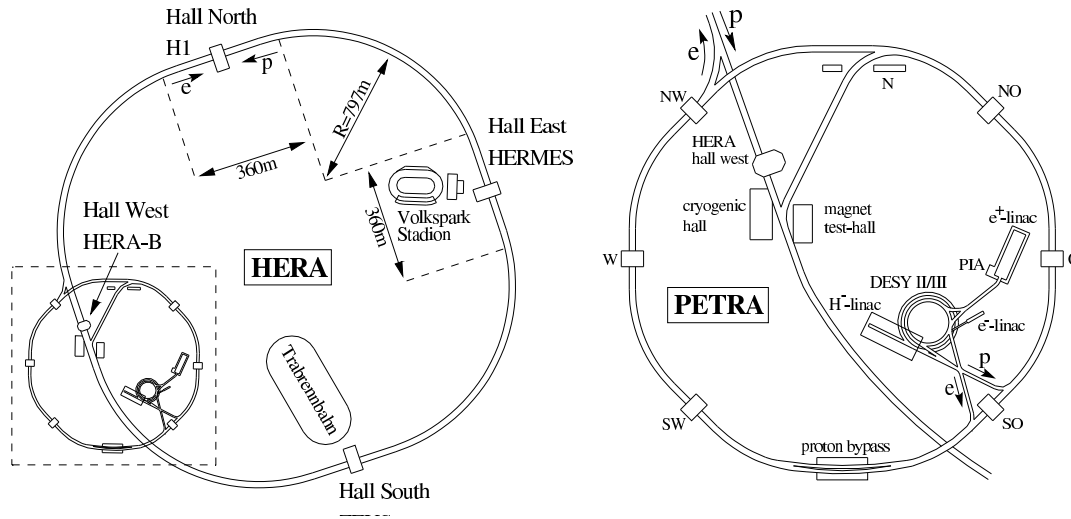


Figure 3.1: Accelerator chains of the HERA facility.

Over the 15 years of HERA running, the combined integrated luminosity delivered to the two experiments reached 1 fb^{-1} .

The HERA II Luminosity Upgrade

The luminosity peak achieved in the first HERA phase was $\simeq 1.8 \times 10^{31} \text{ cm}^{-2}\text{s}^{-1}$. According to eq. (3.1), a higher luminosity can be achieved by increasing the number of particles in the electron or proton bunches, or by decreasing the beam cross section. After the year 2000, the luminosity upgrade of the HERA II phase provided an increase of the instantaneous luminosity to a value of $\simeq 4.8 \times 10^{31} \text{ cm}^{-2}\text{s}^{-1}$. The comparison between the integrated luminosity of the HERA I and the HERA II period can be seen in Fig. 3.2. To achieve this improvement, the HERA accelerator has been equipped with four new superconducting focusing magnets close to the H1 and ZEUS interaction points to decrease $\sigma_{x,y}$. In order to accommodate these magnets, significant changes to the inner part of the H1 detector, in particular, were necessary, as described later.

The new focusing magnets also increase the synchrotron radiation generated inside the H1 detector. To minimize the radiation impact on the detector components, a system of absorbers was placed making an efficient shielding. However, absorbers are themselves a source of backscattered radiations, which implied additional shielding with a system of collimators inside the detector. The beam optics and the synchrotron radiation limit the minimum transverse dimensions of the beam pipe, which has an elliptic shape of $70 \times 110 \text{ mm}^2$ in that region. An important HERA II improvement was also a longitudinal polarisation of the electron beam at the interaction point, realised using special magnet arrangements. More details on the HERA II luminosity upgrade can be found in [25].

HERA II Beam Magnets Relative To the H1 Detector

The HERA-e ring is composed of 456 dipole magnets of the strength of 0.17 T and of 605 quadrupoles as well as other elements. In the four bending regions of HERA (779 m long

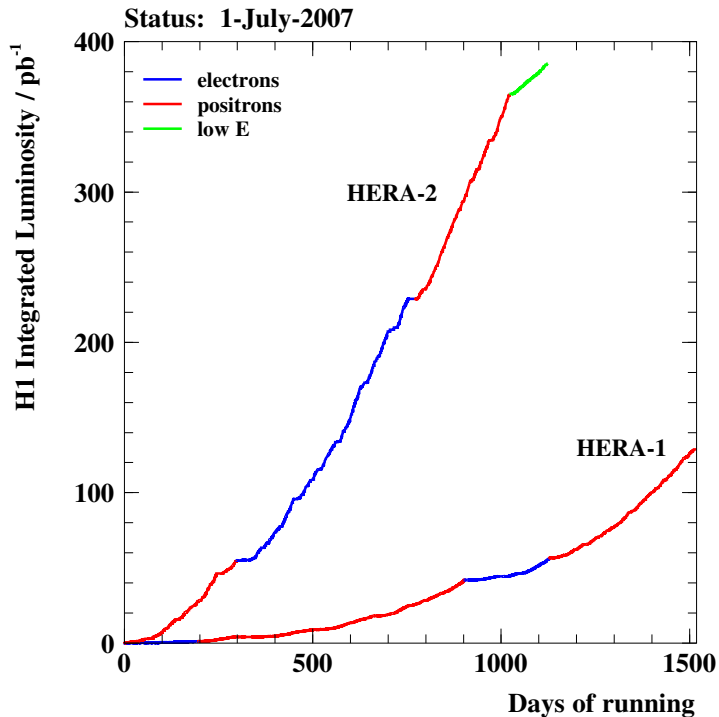


Figure 3.2: The H1 integrated luminosity during the HERA I and HERA II running periods.

each), electron ring magnets are grouped into 12 m long units consisting of a 9 m long bending magnet, a quadrupole and a sextupole. Approximately 90% of the synchrotron radiation created by the electron beam bend is absorbed by the 4 mm thick copper beam pipe cooled by water; the energy loss of electrons is compensated by their acceleration in cavities installed in the straight section of the storage ring. The HERA-p ring contains 422 superconducting dipole magnets (out of which 6 are vertically deflecting) of curvature radius of 588 m, and 224 superconducting quadrupoles [26]. In the bending regions these magnets are grouped in 47 m long units consisting of 4 dipoles, 2 quadrupoles and correction coils.

At the H1 interaction point, electron and proton beams are guided to each other to produce ep interactions. After passing the interaction point, beam trajectories have to be separated, traversing the distance of about 80 cm (in the transverse direction) between the electron and the proton ring. In the following, we first describe magnets close to the H1 interaction point, which are responsible mainly for the focusing of the incoming electron bunches. Then we proceed towards the arcs in the direction of outgoing protons and describe magnets of the proton ring.

The separation of beam trajectories starts at 2 m from the interaction point (thus within the H1 detector), where the combined function (dipole and quadrupole) separator magnet (see Fig. 3.3a) provides the horizontal bend (bending angle of 8 mrad [27]) of incoming electrons and their vertical focusing. At the end of this magnet, the distance between the two beam trajectories is of 17 mm. The separator is followed by a quadrupole doublet responsible for the main part of the electron beam focusing. At the end of this doublet, beam orbits are separated by 47 mm.

The first dedicated proton beam focusing magnets start at 11 m and incorporate two subsequent, vertically focusing, septum quadrupoles of combined length of 13.78 m. The construc-

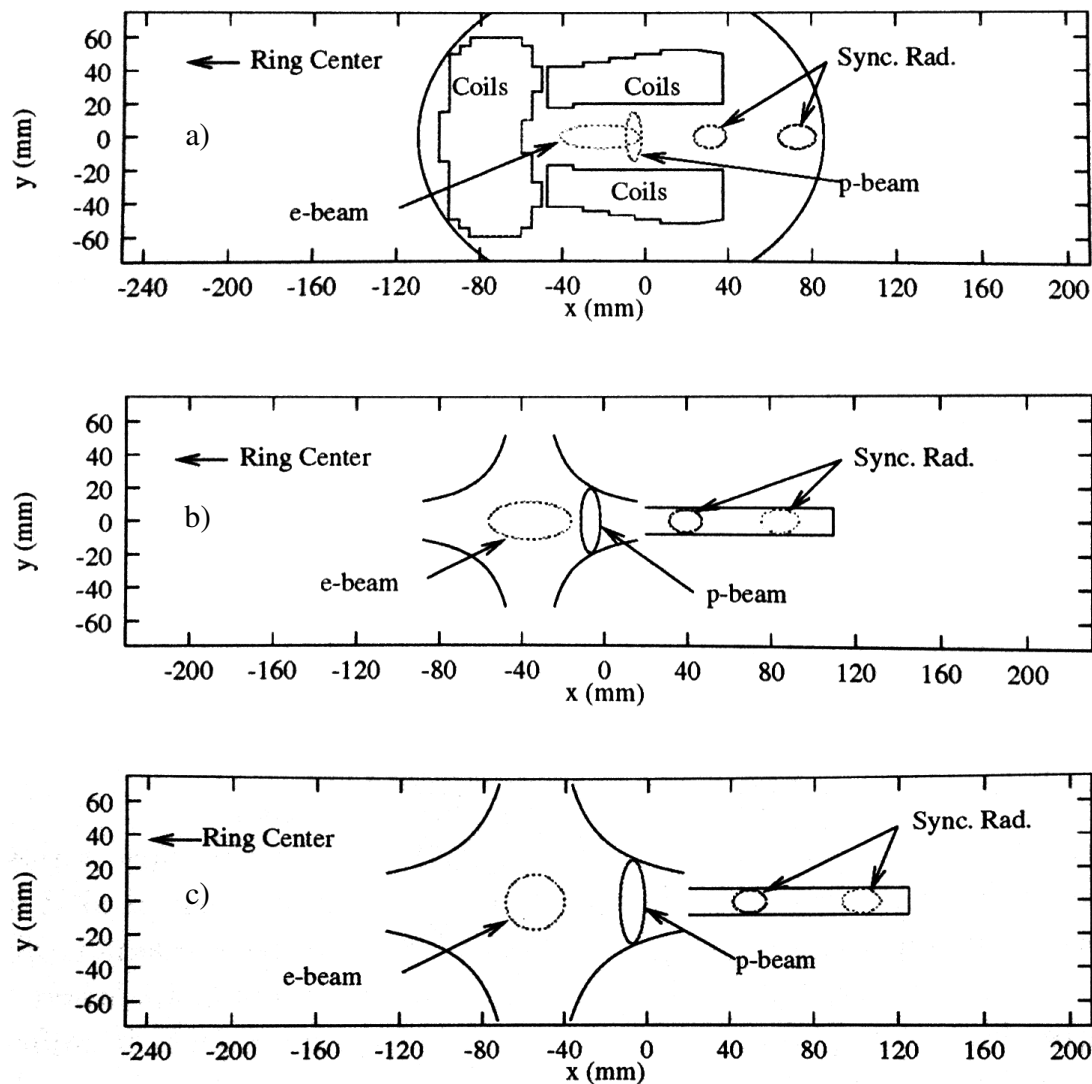


Figure 3.3: Positions of HERA beam magnets in the electron beam focusing region close to the interaction point. $\pm 20\sigma$ and $\pm 12.5\sigma$ are indicated for the electron and the proton beams, respectively. For the case of the outgoing electron beam, an extreme position of the synchrotron radiation cone (right circle) is shown together with an intermediate position. *a)* separator dipole (coil dimensions are not on scale); *b)* end of the first horizontally focusing dipole; *c)* end of the first vertically focusing dipole.

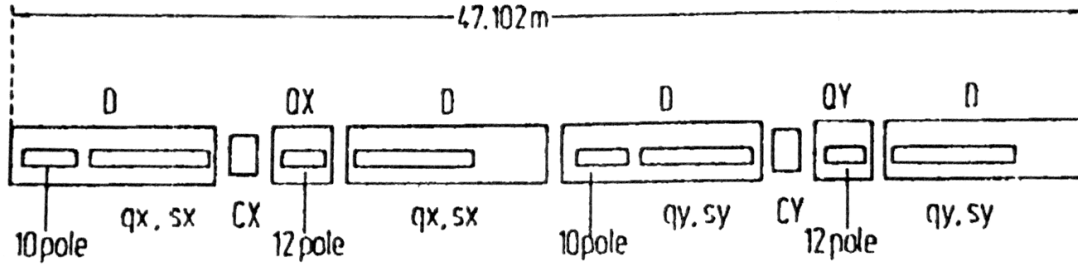


Figure 3.4: The main structure of the proton beam magnet block in HERA arcs: main dipoles (D), main quadrupoles (QX, QY), quadrupole correction coils (qx, qy), sextupole correction coils (sx, sy), correction dipoles (CX, CY). The proton beam direction is from left to right.

tion of septums is such that they isolate the high magnetic field regions seen by the proton beam from a very low field regions for the electron beam. Electrons and protons are now separated in two vacuum beam pipes, but they are still covered within common magnets. At the end of septum magnets, at 25.3 m, beams are separated by 178 mm, enough space to place separated magnets for the proton beam: three conventional quadrupole magnets are placed in serie to focus protons horizontally. At 35.4 m, most of the proton beam focusing is accomplished.

The separation of the two beams, as described so far, was in the horizontal direction. However, approaching the arcs the proton beam is bended such that it is moved above the electron beam. This is done between 56 m and 79 m by several bending magnets. Bending the proton beam allows (by placing a calorimeter close to the beam pipe) to measure interactions with a leading neutron, in particular $ep \rightarrow enX$. The main horizontal bending of the proton beam starts at approximately 120 m from the interaction point. The main structure of magnets in arcs is such that a quadrupole magnet focusing either in the x or the y direction and a correction magnet are always placed before each pair of bending magnets¹ (see Fig. 3.4). In addition, sextupole and higher multipole correction coils (10-pole, 12-pole) layered between main magnets are needed to stabilise the beam. The array of focusing magnets creates alternating focusing and defocusing effects of the proton beam. The first strong focusing occurs at 122 m in the vertical direction. The consequential defocusing effect in the horizontal direction is corrected by the horizontal focusing at 152 m, which in turn creates the vertical defocusing. This is corrected at 180 m by the vertical focusing, which creates the horizontal defocusing up to 200 m. Horizontal defocusing at 200 m is of a particular interest for the study of the VFPS detector, installed in drift space at 220 m (see section 3.2). At 148 m and 200 m two correction magnets are located that are used to create a local beam bump in the x direction between 150 and 300 m (additionally two correction coils at 252 m and 299 m are needed to close the bump) which optimises the VFPS acceptance. More details on the VFPS acceptance and its dependance on the magnet settings are in chapter 4.

In the following, the H1 detector is introduced and its components relevant for analyses in this thesis are described. After the description of the H1 setup at HERA I and the HERA II upgrade, the focus is given on the Very Forward Proton Spectrometer (VFPS) installed at H1 in

¹This is so-called *FODO* lattice, where the *F* quadrupole (horizontally focusing but vertically defocusing) is followed by bending magnets, the *D* quadrupole (vertically focusing but horizontally defocusing) and another bending magnets. The overall effect of the *FODO* configuration is focusing in both horizontal and vertical planes.

2004.

3.1 The H1 Detector

The H1 detector is a multipurpose detector consisting of a set of subdetectors designed for tagging and measuring properties of particles produced in electron proton collisions. Due to the unequal beam energies, detector has an asymmetric design with the forward region (that of the outgoing proton beam) highly segmented to reconstruct hadronic final states of high multiplicity and the backward region optimised for the scattered electron detection. The origin of the right handed H1 coordinate system is at the nominal interaction point. The z axis is pointing in the direction of outgoing protons, the y axis points vertically upwards and the x axis points to the centre of the HERA ring.

As indicated in Fig. 3.5 the electrons enter through the beam pipe [1] from the left and the protons from the right side. The interaction point is surrounded by silicon detectors in the central and the backward region which are followed by the central [2] and forward [3] tracking detectors. These are surrounded by a large calorimeter system consisting of a Spaghetti calorimeter (SpaCal) [12] in the backward and a Liquid Argon calorimeter [4] and [5] in the central and forward region. Both calorimeters are divided into an electromagnetic and hadronic section. An additional plug calorimeter [13] is installed in the forward direction close to the beam pipe. The LAr calorimeter is surrounded by a superconducting coil [6] which provides a homogeneous magnetic field of 1.15 T along the tracking region. The iron return yoke [10] of the magnet is instrumented with streamer tubes and is used to detect muons and to measure energy leakage from hadrons not fully contained in the LAr calorimeter. The forward muon detector [11] has been designed to identify and to measure the momentum of penetrating muons in the forward direction through the use of drift chambers and a toroidal magnet. Between 60 and 90 m the four sets of forward proton spectrometers (FPS) are installed to measure scattered protons. At about 100 m a hadron calorimeter (FNC) is placed to measure neutrons which can emerge from electron proton collisions scattered under low angles. At 220 m a set of two VFPS detectors has been placed for the HERA II phase. In the negative z direction a set of electromagnetic calorimeters is situated to measure the final state particles from the Bremsstrahlung process to determine the luminosity, as well as scattered electrons in the photoproduction process. A more detailed description of the H1 detector can be found in [1].

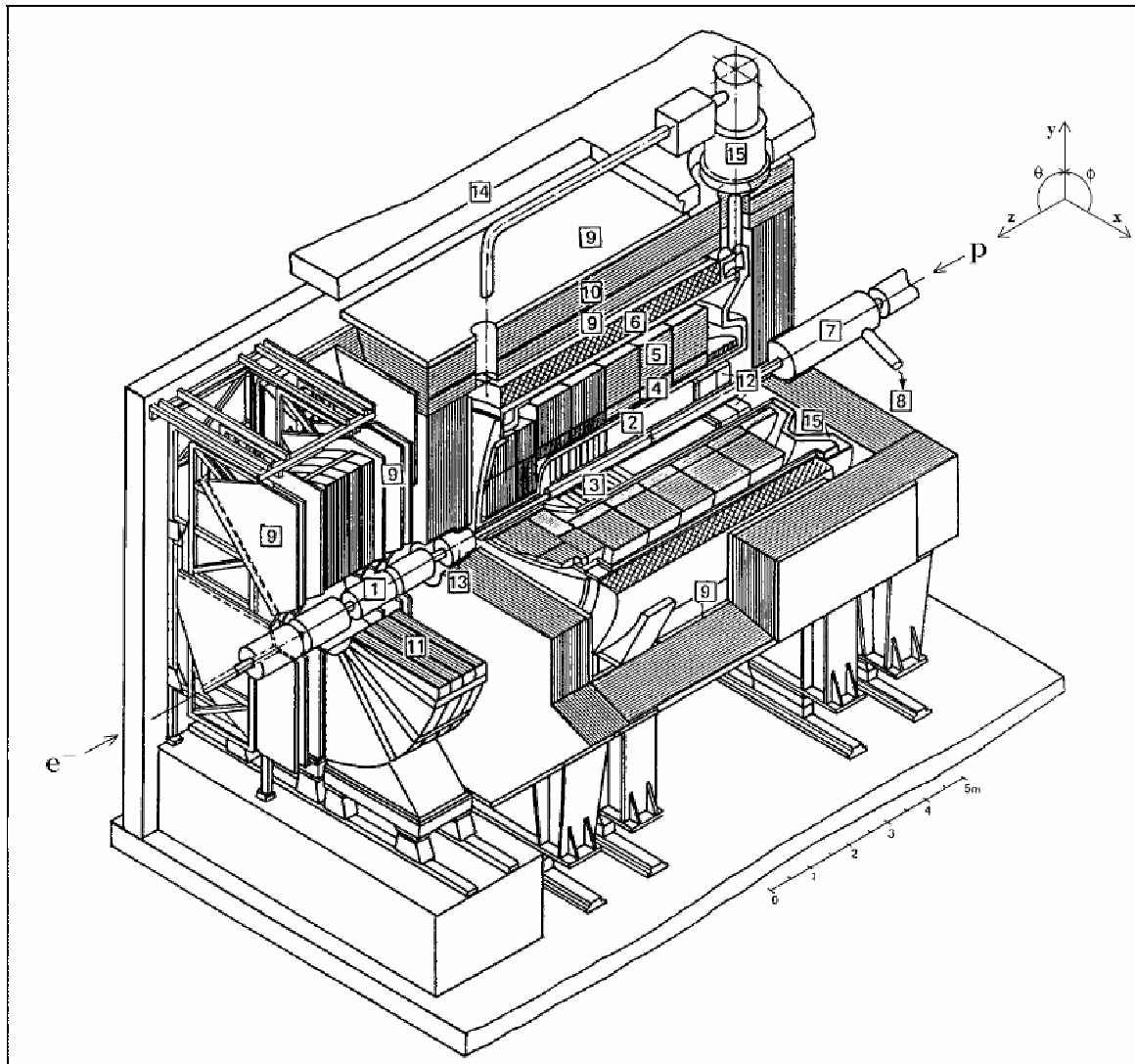
3.1.1 Tracking Detectors

The H1 tracking system is shown in Fig. 3.6 and due to asymmetric beam energies is divided into two complementing sections, the central tracking detector (CTD) and the forward tracking detector (FTD).

Silicon Trackers

Close to the beam pipe, silicon strip detectors are placed to provide a precise vertex information. The Central Silicon Tracker (CST) is placed in the region of nominal interaction point that corresponds to the range of polar angles² between 29° and 151° . It comprises of 32 ladders in

²the range in θ corresponds to ep interactions produced in the nominal interaction point



- | | | | |
|---|---------------------------------|----|-----------------------------|
| 1 | Beam pipe and beam magnets | 9 | Muon chambers |
| 2 | Central tracking device | 10 | Instrumented iron yoke |
| 3 | Forward tracking device | 11 | Forward muon toroid |
| 4 | Electromagnetic LAr calorimeter | 12 | Backw. calorimeter (SpaCal) |
| 5 | Hadronic LAr calorimeter | 13 | PLUG calorimeter |
| 6 | Superconducting coil (1.15 T) | 14 | Concrete shielding |
| 7 | Compensating magnet | 15 | Liquid argon cryostat |
| 8 | Helium supply for 7 | | |

Figure 3.5: The main H1 detector.

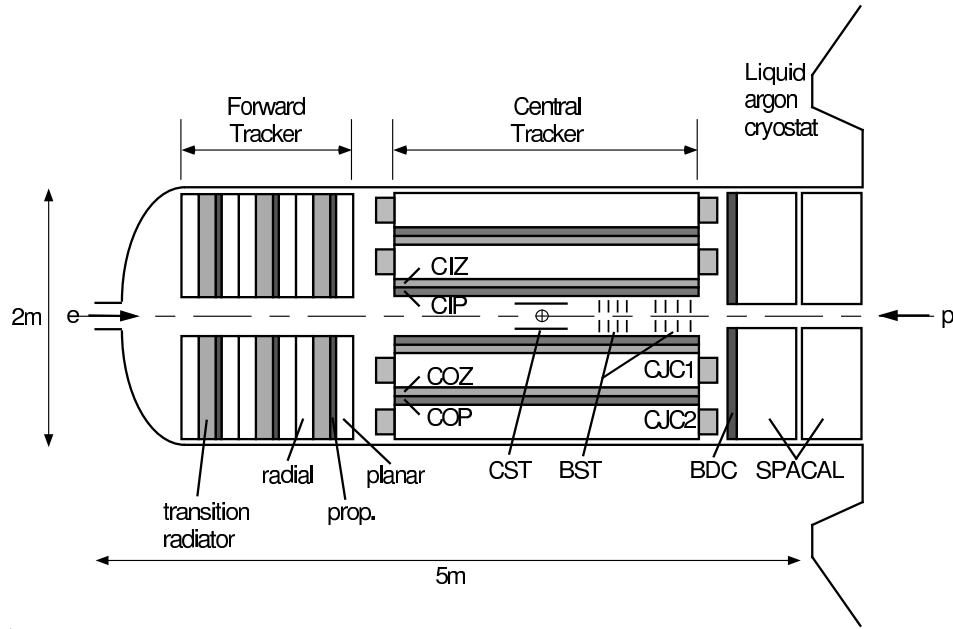


Figure 3.6: Side view of the H1 tracking system of the HERA I phase.

two layers at the radius of 6 cm and 10 cm and provides a measurement of the r and ϕ coordinate of a track with an impact parameter resolution of $57 \mu\text{m}$ [30]. It also provides a measurement of secondary vertices.

The Backward Silicon Tracker (BST) is located close to the beam pipe between the CST and the backward calorimeter SpACal and covers the range of polar angles $165 < \theta < 175^\circ$. The BST consists of 8 planes of silicon detectors arranged perpendicular to the beam axis. Every plane is divided into 16 segments in the azimuthal angle ϕ . Each segment consists of two silicon strip detectors, r - and ϕ -strip detector, with their strip orientation perpendicular and parallel to the radial direction, respectively. The hit information allows to reconstruct tracks in the backward region with a polar angle resolution of $\sigma_\theta \simeq 0.03^\circ$. The BST allows a charge confirmation of the scattered electron at smaller scattering angles with respect to the CJC (see below).

Because of the new beam pipe shape during the HERA II phase, the mechanical arrangement of the CST ladders was changed, as well as the two ϕ sectors of the BST, where a shorter version of these sectors has been used.

Central Tracking Chambers

The track reconstruction in the central region is based on two concentric drift chambers CJC1 and CJC2, central inner (CIZ) and outer (COZ) drift chambers (see Fig. 3.7). The central tracking system covers an angular angle $15 < \theta < 165^\circ$ with a full azimuthal acceptance.

Central Jet Chambers CJC1 and CJC2 have a length of 2.2 m and consist of wires parallel to the beam pipe. Jet cells are tilted by 30° in the transverse plane. The space point resolution is $170 \mu\text{m}$ in the (r, ϕ) plane, whereas the z coordinate of a hit is measured with a resolution of 2.2 cm. Additionally, the specific energy loss dE/dx is measured to improve the particle

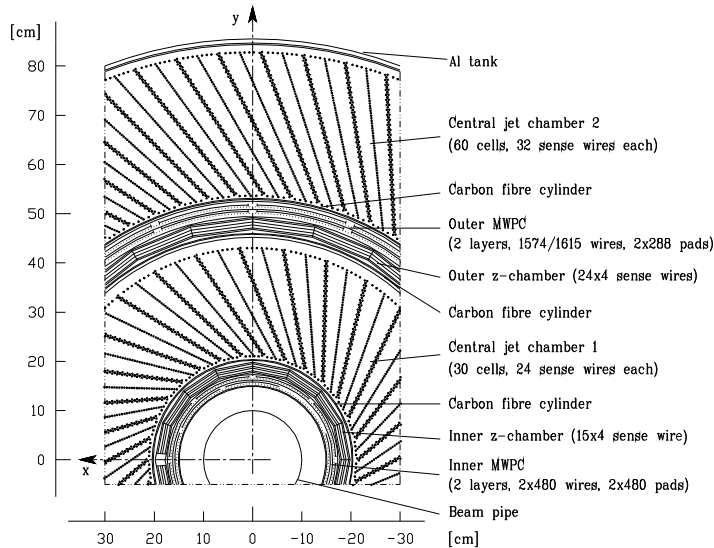


Figure 3.7: The central tracking system, cross section of the x and y plane.

identification. The interaction vertex in x and y coordinate is determined using high momentum tracks and the z coordinate is determined from all tracks fitting to the vertex.

The resolution in z is much improved by the usage of CIZ and COZ chambers with the sense wires mounted perpendicularly to the beam axis. They are located inside and outside of the CJC1 at a radius of 18 and 24 cm, respectively, and provide a $260 \mu\text{m}$ resolution in the z coordinate. The thickness of both chambers is below 1% of radiation length.

The combination of CJC1 and CJC2 with the z chambers leads to the momentum resolution for the track measurement of $\sigma(p)/p^2 < 0.01 \text{ GeV}^{-1}$. Two central multiwire proportional chambers, CIP and COP having a response time faster than the beam crossing rate, provide level 1 trigger information (section 3.1.6).

During the HERA II luminosity upgrade, the CIP system and the first level triggering based on it has been replaced and improved [28] in order to better discriminate ep collisions against beam related background events. The CIP made of two planes was replaced by a five plane cylindrical proportional chamber with four times higher z granularity. The spatial resolution of the new CIP chamber in z amounts to about 1.5 cm. The new vertex trigger has an improved angle acceptance (up to 168°) and better background rejection capabilities. At that time the CIZ was removed.

Forward Tracking Chambers

The forward tracking detector (FTD) covers the angular range of $5 < \theta < 25^\circ$ and is built from three supermodules, each containing, along the increasing z , a planar drift chamber, a proportional chamber, a transition radiation tracker and a radial drift chamber, as shown in Fig. 3.8. The planar chambers consist of parallel sense wires in a plane perpendicular to the beam axis and provide an accurate measurement of the polar angle. The multiwire proportional chambers (FPC) are used to provide a trigger based on charged particle presence in the forward region. Transition radiators produce transition radiation photons, which are detected in the

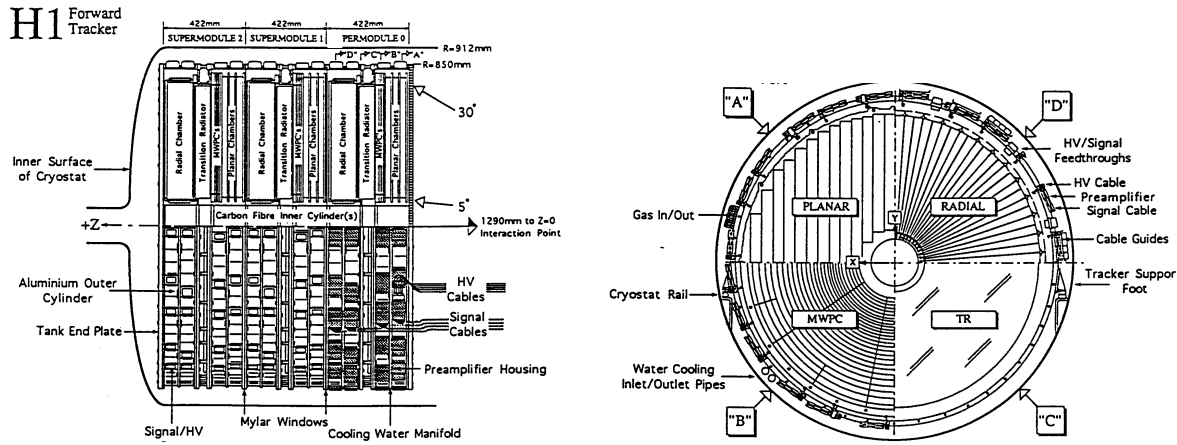


Figure 3.8: A single supermodule of the FTD. The $r - z$ view (left) shows the different components and the $r - \phi$ view (right) shows the basic structure of each component.

neighbouring radial chamber. The radial chambers supply an accurate determination of the azimuthal angle ϕ .

At HERA I, the FTD apparatus had an efficiency of well measured tracks of below 50% for events with high forward track multiplicity, raising to 90% for low forward track multiplicity events, such as the elastic J/ψ production. In order to increase the track finding efficiency for the HERA II upgrade, several modifications were made to the forward tracker [29]. The FPC was removed. The region of $\theta < 12^\circ$ was then covered by scintillator trigger planes, inserted at $z \sim 2.65$ m, i.e. in front of the FTD. Three extra planar chambers have been installed into the freed space to suppress ambiguities. An increased number of wires in the new chambers aided the accuracy of measurements.

The Backward Drift Chamber

The backward drift chamber (BDC) was located in front of the backward calorimeter SpaCal at $z \sim -142$ cm during the HERA I period and covered the range of $151 < \theta < 177.5^\circ$. It provided a precise measurement of the polar angle of the scattered electron in the backward region. The wires in the BDC are perpendicular to the beam direction and are arranged in four pairs of octagonal double layers. Each double layer is rotated with respect to the previous layer by $\Delta\phi = \pi/16$ which leads to an improved measurement at the boundaries of the octant.

For HERA II, the BDC was replaced by the backward proportional chamber (BPC), which consists of three layers of hexagonal proportional chambers overlaid in order to measure the hit coordinate of a particle track with a high accuracy.

3.1.2 Calorimeters

The calorimetry at H1 is provided by sampling calorimeters, which consist of absorbing layers and sampling (active) layers. Incident particles, that reach calorimeter, undergo interactions with the absorber and form a shower. The energy of the shower, measured through ionization in the sampling layers is proportional to the energy of the incident particle, assuming the shower

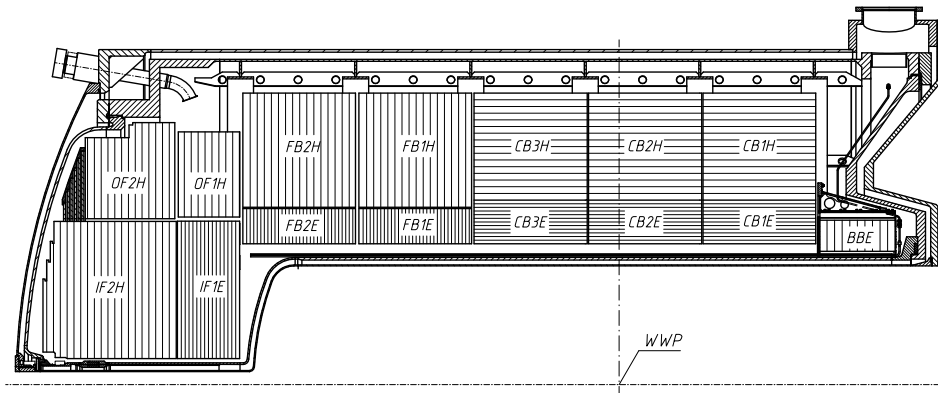


Figure 3.9: Schematic view of the LAr calorimeter.

is fully contained in the calorimeter. A propagation of an electromagnetic particle through an absorbing layer is governed by the radiation length, which is the distance corresponding to a particle energy loss of $1/e$. In case of strongly interacting particles, the characteristic length is the interaction length.

The Liquid Argon Calorimeter

One of the basic requirements of the H1 detector is to provide a clear identification and a precise measurement of electrons together with a good performance of the measurement of jets with high particle densities. These requirements were met by a calorimeter inside a large coil to minimise the amount of the dead material in front of the calorimeter. The liquid argon calorimeter (LAr) is a sandwich type calorimeter (shown in Fig. 3.9) with the pseudorapidity coverage between $3.4 > \eta > -1.4$. The calorimeter is divided into the inner electromagnetic region composed of an absorber made of 2.3 mm thick lead plates and the outer hadronic region with an absorber material of 16 mm steel plates. Between the plates supplemented with a high voltage, gaps are filled by liquid argon, used as the active detection material in both sections. The electromagnetic part amounts 20 to 30 radiation lengths and the hadronic part is 5 to 8 interaction lengths thick, depending on the polar angle. The LAr is non compensating, thus the calorimeter response to hadrons of the same energy as i.e. electrons is reduced, typically by 30%. This difference is adjusted by reweighting the hadronic energy in the offline reconstruction software. The energy resolutions for electromagnetic showers, σ_{em} , and that for hadronic showers, σ_{had} are:

$$\frac{\sigma_{em}(E)}{E} = \frac{0.12}{\sqrt{E [\text{GeV}]}} \oplus 0.01, \quad (3.3)$$

$$\frac{\sigma_{had}(E)}{E} = \frac{0.50}{\sqrt{E [\text{GeV}]}} \oplus 0.02. \quad (3.4)$$

SpaCal

The backward scattering region between $153 < \theta < 178^\circ$ is covered by the spaghetti calorimeter or SpaCal. It is a non compensating sampling calorimeter located between $z = -151$ and -244

cm, split into inner electromagnetic and outer calorimetric sections. In contrary to the LAr, the absorber material in both sections is lead with embedded scintillating fibres as the active material. Due to a limited space available for the calorimeter, both sections are 25 cm deep and correspond to 28 radiation (1 interaction) lengths. The number of combined interaction lengths of both sections is 2.2. A reliable electron pion separation helps to suppress background events to DIS events originating from the photoproduction. The resolutions of the electromagnetic, σ_{em} and hadronic, σ_{had} part are [19]:

$$\frac{\sigma_{em}(E)}{E} = \frac{0.07}{\sqrt{E [\text{GeV}]}} \oplus 0.01, \quad (3.5)$$

$$\frac{\sigma_{had}(E)}{E} = \frac{0.50}{\sqrt{E [\text{GeV}]}} \oplus 0.02. \quad (3.6)$$

Before the luminosity upgrade the acceptance in the SpaCal corresponded to photon virtualities of $2 < Q^2 < 100 \text{ GeV}^2$. During the upgrade a number of inner SpaCal cells were removed which reduced the polar angular coverage to $153 < \theta < 173^\circ$. As a consequence, the acceptance in Q^2 is reduced to $4 < Q^2 < 100 \text{ GeV}^2$.

3.1.3 The Muon System

Muons generally escape the calorimeters as their bremsstrahlung radiation is suppressed compared to the electron, as a result of their heavier mass. The detection system is provided by central and forward muon detectors (CMD and FMD) installed outside the main calorimeters and coil. The CMD is part of the instrumented iron yoke and covers an angular range $6 < \theta < 175^\circ$. The forward region of the detector is equipped with a muon spectrometer which allows to detect muons with momenta above 5 GeV within the polar angular range $3 < \theta < 17^\circ$. The FMD consists of a toroid magnet between three double layers of drift chambers at both sides. The drift chambers allow to measure the muon track before and after the magnet. The momentum is reconstructed from the deflection of the muon trajectory in the magnetic field of the toroid. The first drift chamber (three layers in front of the toroidal magnet) is also used to study proton dissociation events in diffraction.

3.1.4 Time of Flight Counters

The time of flight (ToF) system consists of a set of fast scintillators mounted perpendicularly to the beam pipe. They are used to distinguish ep interactions from beam induced background. ToF detectors provide a fast trigger information at the first trigger level. Background events produced near the nominal vertex cannot be distinguished from ep interactions using timing requirement, but the counters are able to significantly reduce the background with vertices far away from the interaction point. The ToF devices are located within the unused gaps of the Plug absorber, integrated inside the SpaCal calorimeter and behind the backward end cap of the instrumented iron.

3.1.5 The Luminosity System

The Bethe-Heitler process $ep \rightarrow e\gamma p$ is used for the luminosity measurement due to its large cross section and calculability in quantum electrodynamics with a high precision. The scattered

electron and the final state photon are detected in the two very backward Čerenkov crystal calorimeters installed in the HERA tunnel, the electron tagger located at $z = -33$ m and the photon detector at -103 m distance from the interaction point. The main background to the luminosity measurement is the interaction of electrons with the remaining gas atoms in the beam pipe, $eA \rightarrow eA\gamma$. This background is measured using the data from electron bunches that do not collide with a proton bunch (the corresponding proton bunch is left empty) and corresponds to 10% of the total bremsstrahlung rate.

The Electron Tagger

The electron tagger consists of crystals of 22 radiation lengths in a 7×7 array corresponding to an area of 154×154 mm². The detector has an angular acceptance of 1 mrad and is mounted on a movable platform, which is retracted during the beam injection as a protection from the radiation damage. Apart of electrons from the bremsstrahlung process, scattered electrons from the electron proton collisions are detected in the tagger if they are scattered at small angles. Electrons are deflected by bending magnets and escape the beam pipe through an exit window at $z \simeq -27$ m.

The Photon Detector

The photon detector (PD) is a Čerenkov crystal calorimeter consisting of 25 crystals in a 5×5 array covering the area of 100×100 mm². Similarly to the electron tagger, the photon detector is equipped with a movable platform and is retracted during time of beam preparation. In addition to the energy, it also measures the x and y position of the photon in order to provide an online feedback on the electron beam tilt to HERA crew.

The energy resolution of the luminosity system, averaged over the years 1999 and 2000, is

$$\frac{\sigma_E}{E} = \frac{0.17}{\sqrt{E[\text{GeV}]}} \oplus 0.01. \quad (3.7)$$

The resolution as a function of the run number is shown in Fig. 3.10. The resolution degradation over the time is related to the radiation damage of the crystals. Small regions of better resolutions are due to the partial recovery of the crystal's transparency during planned shutdowns of the HERA accelerator. The big improvement at run values above 200000 is due to the exchange of crystals in the 1997/98 shutdown.

At HERA I, the online luminosity was measured by the coincidence in the electron tagger and the photon detector, with a condition of the sum of the electron and the photon energy to equal the incident electron, $E_{e'} + E_\gamma \simeq 27.6$ GeV. The offline luminosity measurement is determined by the rate of photons of the energy above 10 GeV detected in the photon detector. This method is accurate to 1.5%.

The luminosity system has been substantially modified to deal with challenges of the HERA II. Due to the change in beam optics and placement of new magnets, the 33 m electron tagger was removed and the luminosity is measured using only the photon detector. The stronger bending of the electron beam leads to a significantly higher rate of the synchrotron radiation compared to HERA I. The PD is therefore shielded by the absorber made of a lead filter of two interaction lengths, which attenuates the synchrotron radiation by almost five orders of magnitude. Multiple photons may be produced per bunch crossing at the design luminosities

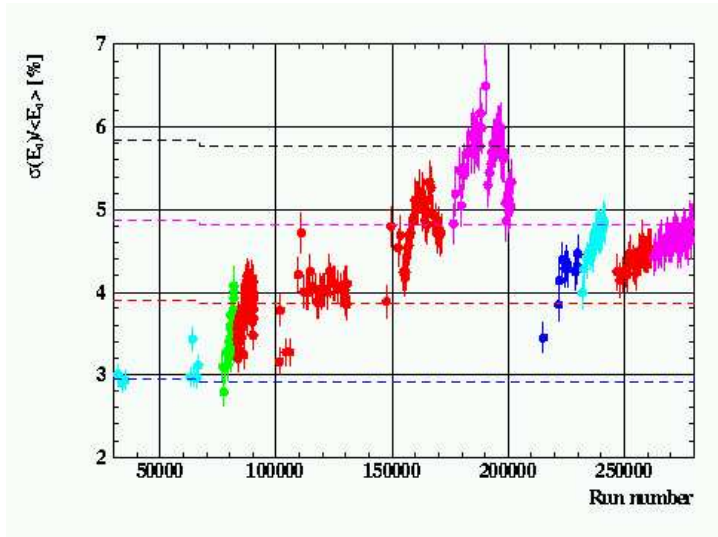


Figure 3.10: The energy resolution of the H1 luminosity system calorimeters at HERA I, based on fully reconstructed bremsstrahlung events $ep \rightarrow ep\gamma$ and is defined as the width of the energy distribution $E_e^{rec} + E_\gamma^{rec}$ from the peak position, which should be at the electron beam energy $E_0 = 27.6$ GeV. The dashed lines correspond to the values $A = 10\%$, 15% , 20% and 25% (from bottom to top) in the resolution parameterisation $\sigma/E = A/\sqrt{E} + 1\%$.

of HERA II and for this reason an upgraded electronics is necessary to control photon pileup effects.

3.1.6 The Trigger System

The rate of non ep interactions is ≈ 100 kHz, several orders of magnitude larger than that of ep interactions. The main contribution to this background are collisions of beam protons with atoms of the residual gas in the beam pipe, interactions of muons from the halo of the proton beam with the beam pipe and synchrotron radiation from the electron beam, partly rejected by collimators. The purpose of the trigger system is to select physically interesting ep interactions within a limited time frame.

H1 is using the 4 level online trigger system (see Fig. 3.11) to gradually lower the rate of kept data (from ~ 10 MHz to several Hz) to be finally saved on tapes.

Level 1

The level 1 trigger is fully hardwired and the decision on acceptance of an event is made on the basis of 128 logical combinations of the 256 trigger elements, called subtriggers. At the level 1, the trigger provides a fast decision within $2.3 \mu\text{s}$. To avoid dead time, all signals are stored in pipelines and after a synchronisation of the trigger elements, the 128 subtriggers are formed. The trigger decision of $2.5 \mu\text{s}$ is thus only a latency and does not create dead time. Each event is marked by a 128 bit pattern, representing a logical states of all subtriggers. In order to cope with high trigger rates, the subtriggers with too high raw rate are downscaled by a number n ,

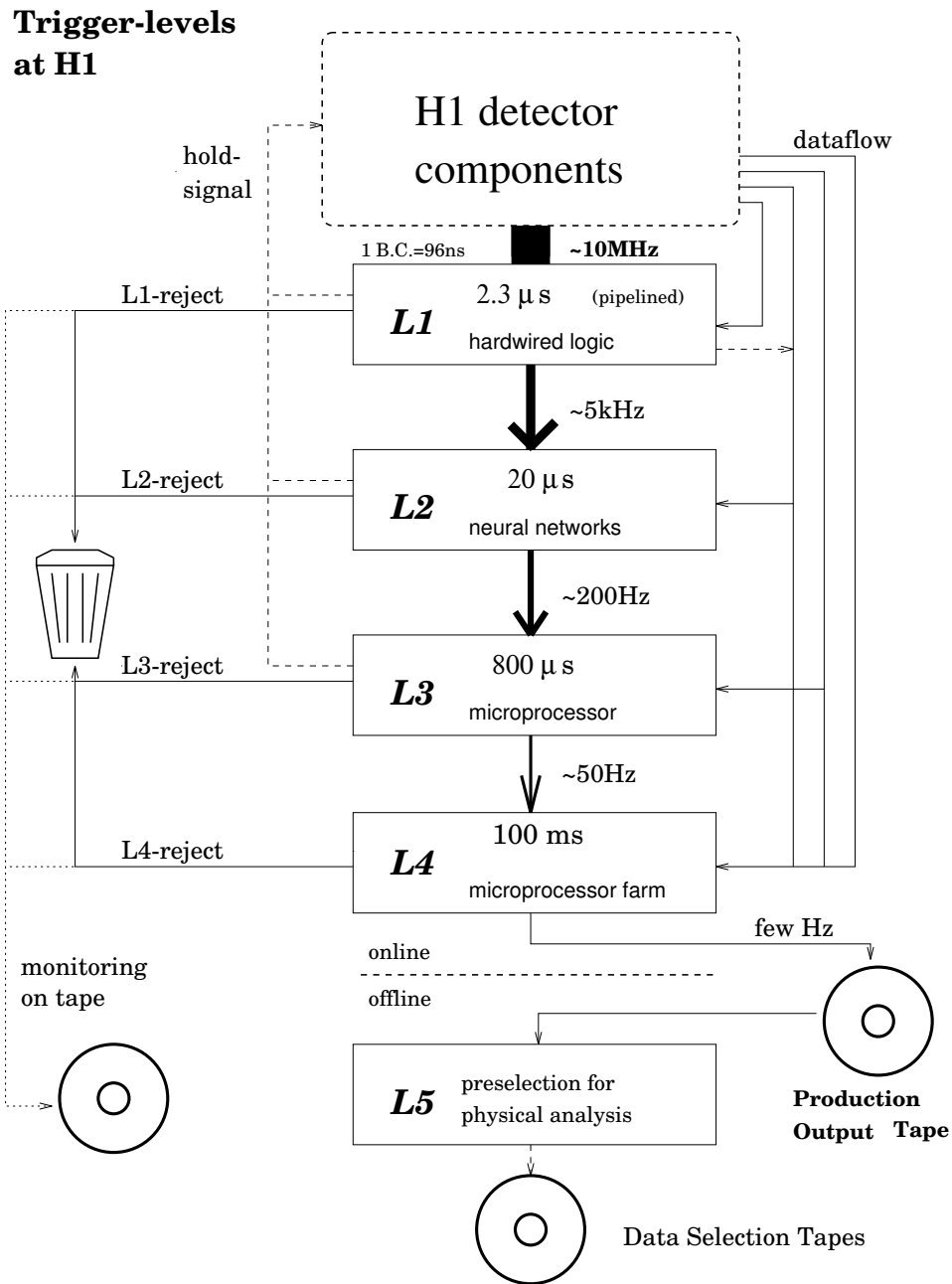


Figure 3.11: The H1 trigger system.

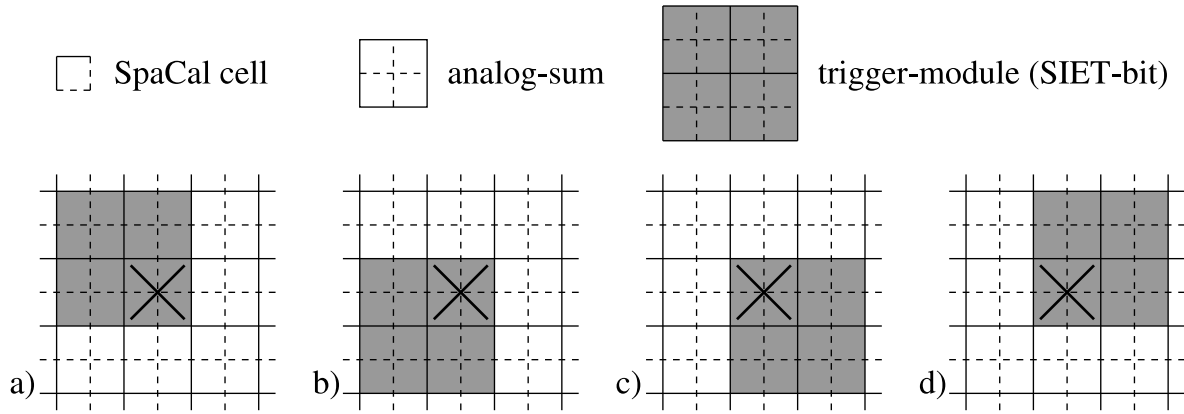


Figure 3.12: A schematic view of SpaCal cells, analog sums and trigger modules. The two dimensional sliding analog summation by trigger modules is shown as well.

such that only every n^{th} triggered event is kept and produces a L1Keep signal. The L1Keep signal sends all information of trigger elements as the input for the level 2.

The SpaCal Level 1 Elements The level 1 SpaCal trigger uses the light from fibres, read by photomultiplier tubes with the time resolution of less than 1 ns. The basic units of the electromagnetic part of the SpaCal are cells with the transverse size of $40 \times 40 \text{ mm}^2$. For trigger purpose, analog signals from 2×2 cells are summed together and so called analog sums are created. 2×2 analog sums (16 cells) are grouped together to form a single trigger module (see Fig. 3.12). Trigger modules overlap such that each analog sum is part of four trigger modules. The overlapping guarantees the absence of trigger inefficiencies as a function of the particle impact point, because the electromagnetic shower energy is always fully recovered in one of the trigger modules [20]. The inclusive electron trigger (IET) is comprised of 4×4 trigger modules and is designed to compare the deposited energy with each of the three thresholds, 0.5, 2.0 and 6.0 GeV. The resulting information, the trigger element `SPCLe_IET`, is coded into two bits and provides the level 1 trigger decision. In the central region, i.e. around the beam pipe, is given by a separate IET trigger, the `SPCLe_IET_Cen` element.

Level 2

Two different systems are implemented for the level 2 trigger, a topological trigger and a neural network. Both of them use a combination of signals from various detectors. The topological trigger works with a pattern recognition in detectors, whereas the neural network systems are trained separately for each L2 subtrigger. The maximum decision time of the L2 trigger is $20 \mu\text{s}$ and within this time the detector is unable to take events. The L2 sends an L2Keep signal that validates the L1 decision and causes the event to be read out to and send to the level 3 trigger. In this case the data taking remains stopped, resulting in a dead time of approximately one millisecond. If the L1 decision is not validated by the L2, the data taking resumes.

Level 3

At HERA I, the trigger level 3 was not used. At HERA II, the third level uses a farm of RISC based processors with processing time of $50 \mu\text{s}$ per event, employing the Fast Track Trigger (FTT) and making more use of correlation between detector subsystems to provide in particular a jet trigger. The Fast Track Trigger, commissioned as part of the H1 upgrade program, performs a fast reconstruction of CJC tracks. The FTT also provides some trigger elements for use at L1 and L2 and is able to perform a particle identification and invariant mass reconstruction at L3.

Level 4/5

The last level is a software trigger consisting of a processor farm. At this level starts a limited reconstruction from signals in electronics into the physics information and events are classified according to different types of underlying physics. The detailed linking of track and clusters from different subdetectors is made and the fully reconstructed physics subtriggers are subject to further cuts, rejecting further background events. The processing time per event is approximately 100 ms. In order to reduce the volume of data finally recorded into tapes, some high rate physics processes are downscaled.

The L4 verification process continues until either no L4 bits remain set, then the event is rejected, or the verification is completed and the event is kept [21]. Beam-gas, beam-wall and cosmic ray induced events are rejected mainly by cuts on the z coordinate of the event vertex, track distance or kinematic cuts. The hard scale physics or exclusive final states based on sophisticated finders are kept and the soft physics is downscaled depending on the reconstructed photon virtuality Q^2 . The smaller is the reconstructed Q^2 , the higher is the downscale factor [22].

Once the L4 decision is reached, the remaining part of the code is not executed and the accepted event is written to the tape. To cross check that no good events were rejected, 1% of the rejected events is written on the L4-reject tapes. These events are expected to be pure background by definition and are not supposed to be considered directly in any analysis.

At the beginning of the HERA I running phase a fast online event reconstruction was performed at the trigger level 4 and a decision was taken if the event should be kept for permanent recording or not. The full event reconstruction was done offline at the trigger level 5. Later on, both trigger levels were merged in a single level called L4/5 [23].

Globally the trigger downscale factors are tuned to keep the total dead time typically around 10%.

3.2 The Very Forward Proton Spectrometer

To take full advantage of the luminosity increase at the HERA II phase, a very forward proton spectrometer (VFPS) was installed, dedicated to measure the scattered proton in diffractive $ep \rightarrow eXp$ processes with a very large acceptance in the kinematic region of $0.005 < x_p < 0.01$ and $0 < |t| < 0.5 \text{ GeV}^2$.

3.2.1 Design and Location

The VFPS consists of two independent stations called Roman Pots. A Roman Pot is a construction of an insert into the beam pipe with a movable mechanism that allows the pot with mounted detectors to move (in the present case horizontally) very close to the beam. The two VFPS pots are installed in the 6.2 m long drift section of the proton beam pipe at 218 and 222 m from the interaction point. This section is located in the cold section of the proton beam, i.e. where superconducting magnets are used. In the cold section, the proton beam pipe is contained in a cryogenic system. In order to access the beam pipe with Roman pot detectors, the drift section of the VFPS was replaced by a warm beam pipe (operating at room temperature) and a U-turn bypass to transport all cryogenic elements.

Fig 3.13 shows a single VFPS station. The two triangle-shaped detectors are placed in a plunger vessel which can be moved (in the x direction) close to the beam via the 100 mm diameter inserts in the beam pipe. The plunger vessel is a stainless steel cylinder with a bottom plate and 0.3 mm thick windows, to reduce the material amount in front of the detectors. Detectors installed in the plunger vessel filled with the N_2 gas operate at atmospheric pressure. The pot movement is controlled by a stepping motor with a precision of $5 \mu\text{m}$. In the case of high background rates, accidental beam loss or power failure, a hydraulic system enables a fast retraction of the pots. When the interaction rate in detectors is above a critical value, the pot is quickly moved to its safe parking position. The position measurement of each Roman pot with respect to HERA magnets is performed by Heidenhein rulers and is transmitted to the H1, ZEUS and HERA control rooms. Both pots are set to the parking position during proton beam injection and beam dump and are moved as close as possible to the beam in case of stable beam conditions, whilst ensuring that the particle rate in detectors is not too high and that the close position of the pots does not limit the beam lifetime.

The active area of each of the two identical detectors at the end of the support arm has transverse dimensions of 21.1 mm perpendicular to the beam and 3.6 mm parallel to the beam. The two detectors in a single VFPS station are separated by 60 mm to allow the reconstruction of a local track segment of the proton trajectory. Each detector is composed of the u and the v plane of scintillating fibres rotated by $\pm 45^\circ$ with respect to the direction of the pot horizontal movement. Each detector thus records two coordinates such that a straight line through the measured points in a single pot determines a local trajectory of the particle. Fig. 3.14 shows the details of the two detectors of one pot. Each detector measuring a single u or v coordinate is composed of five layers of 120 scintillating fibres as shown in Fig. 3.15. Each row of five fibres is connected into a single light guide. Four such light guides (labeled A, B, C and D) are in turn connected into a single position sensitive photomultiplier (PSPM) channel. The consequence of the fibre multiplexing is an ambiguity in the hit recognition. Since a VFPS station aims to measure only one particle track, this ambiguity is resolved by a segmentation of trigger planes into four scintillator tiles. Trigger planes cover the two scintillating fibre planes and are connected into separate photomultipliers. Scintillator tiles deliver a fast trigger signal and despite the large distance of the VFPS from the main H1 detector, the trigger signal arriving by an air cable has a delay of $1.96 \mu\text{s}$, small enough to enter the trigger at level 1.

In order to determine the optimal position for the VFPS pots along the beam in the forward region in terms of the $x_{\mathcal{P}}$ and t acceptance and resolution, the HERA beam optic was simulated using the linear beam optics approximation [24]. The behaviour of the scattered proton that loses 1% of its incident energy ($x_{\mathcal{P}} = 10^{-2}$) is shown in Fig. 3.16. Beam protons not interacting

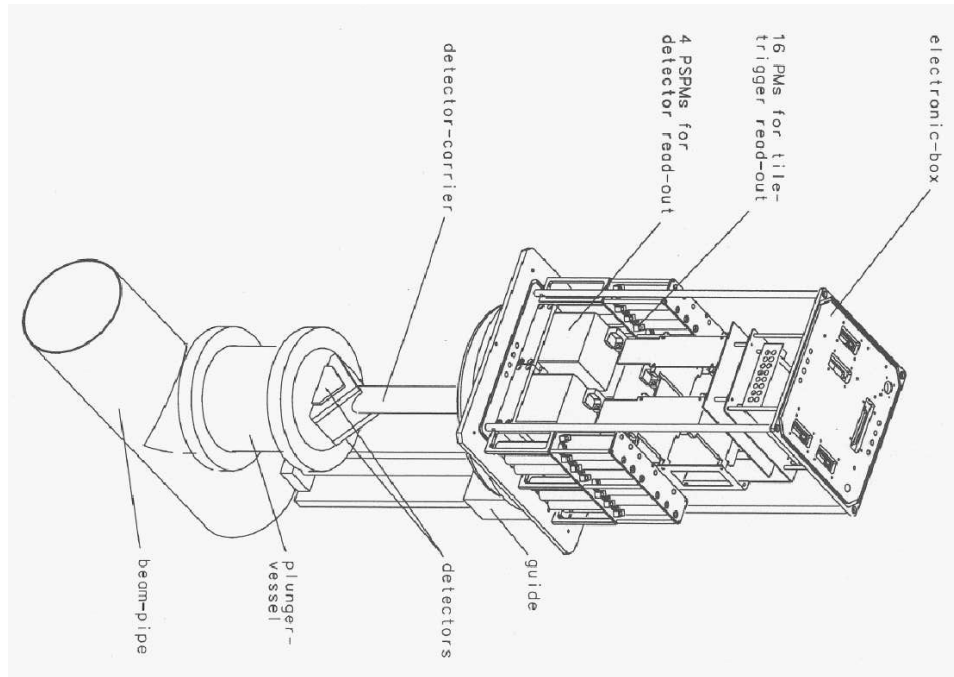


Figure 3.13: A T-shaped beam insert with a plunger vessel and a single VFPS station. The right part of the scheme shows the associated electronics.

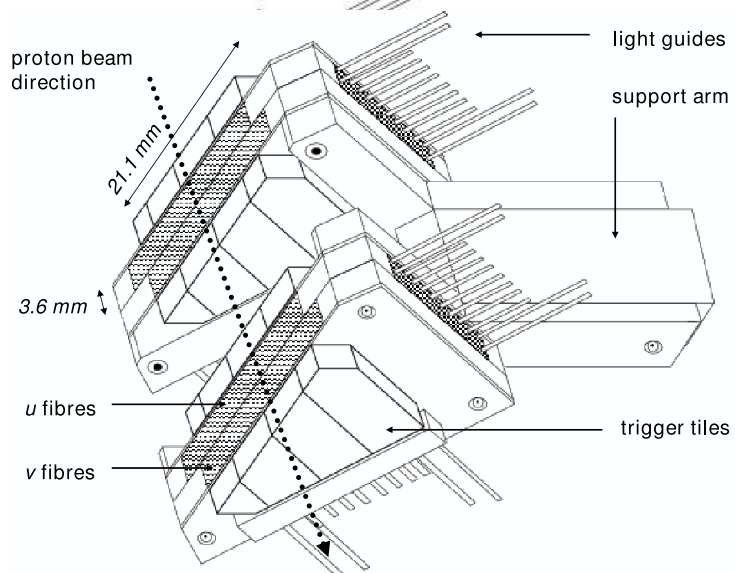


Figure 3.14: One station of two detectors showing the u and v fibre planes sandwiched between the trigger tiles. Tiles in the u plane are rotated by 45° w.r.t. tiles in the v plane.

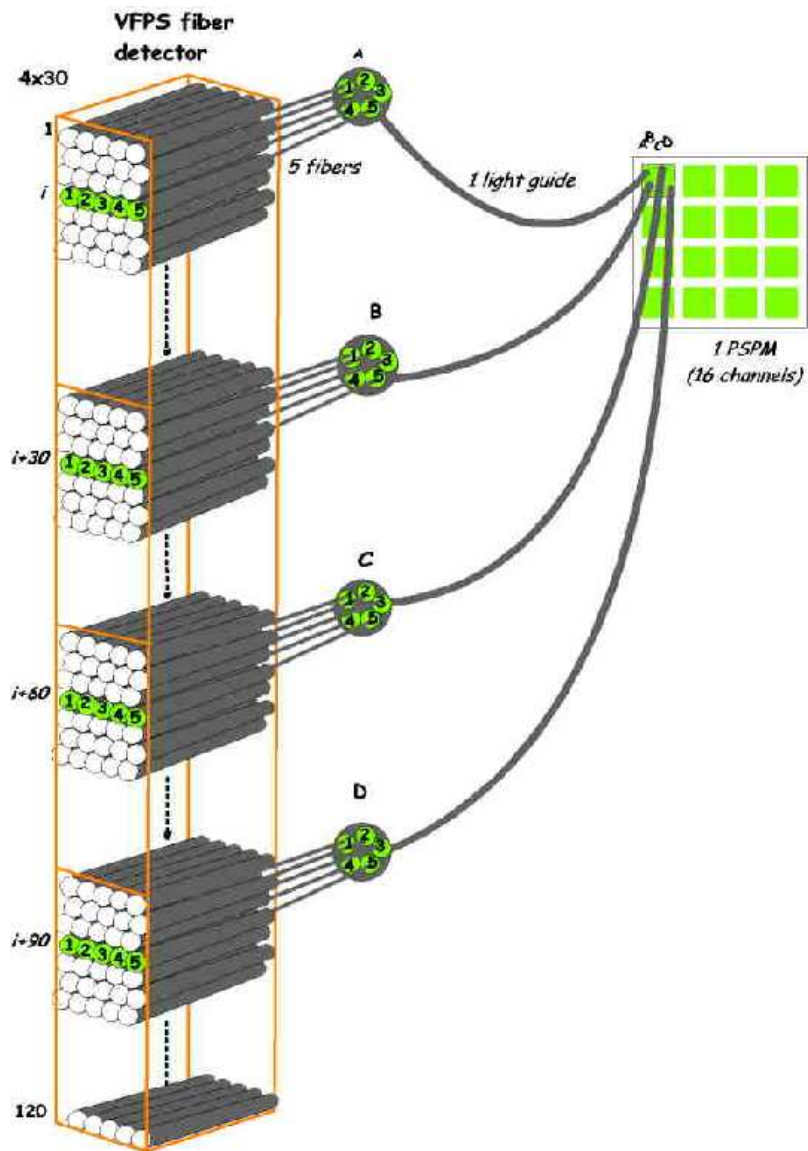


Figure 3.15: Scintillating fibres composed into one plane. Each row of five fibres is attached into one light guide and four such light guides, separated by 30 rows, are attached to a single photomultiplier.

with electrons at the interaction point form the beam envelope. The 12σ transverse distance from the center of the nominal beam is shown as the hatched area; 12σ is considered to be a safe distance, where the current is low enough not to damage the detectors. The proton beam inclination starts after the bending magnets at the distance of $z \simeq 125$ m from the interaction point. A scattered proton that loses a fraction of its energy (coloured areas) is bent in the transverse plane due to spectroscopic effects of the horizontal HERA dipole magnets and leaves the beam envelope (as can be seen in the horizontal projection) at locations beyond 160 m and hence can, in principle, be measured. Such a proton trajectory also depends on the transverse momentum it gained in the interaction with the electron. Trajectories for $|t| = \sqrt{p_x^2 + p_y^2}$ of 0.01, 0.1 and 0.5 GeV² are shown with different colors in the same figure. For comparison, the vertical projection shows that such scattered protons do not leave the beam envelope in the y direction. Fig. 3.16 shows also positions of magnets along the beam pipe (the dash-dotted lines between the two images). Since the magnets cannot be moved, a place must be found to accommodate the VFPS stations between them. Three drift spaces exist between the magnets to install the set of two Roman pots: at 165 m, 190 m and 220 m. The position of 220 m was chosen for the VFPS due to the largest acceptance.

3.2.2 The $x_{\mathcal{P}}$ and t Reconstruction

The spectroscopic effect of the bending magnets plays a role in the resulting impact point of scattered proton in the x and y plane of the VFPS detectors. Scattered protons with higher energy losses (larger $x_{\mathcal{P}}$ values) are bent more strongly towards the centre of the HERA ring, than those with smaller energy losses. Fig. 3.17 illustrates impact points of protons with $x_{\mathcal{P}} = 10^{-2}$ and $0 < |t| < 0.5$ GeV² at 220 m. The impact point is shifted mainly in x by approximately 1 cm. This translates into a basic measurement of $x_{\mathcal{P}}$. This point is smeared due to the transverse momentum of the scattered proton. Furthermore additional smearing not considered in Fig. 3.17 should be considered due to the variation in the transverse position of the interaction vertex, the beam divergence and the beam energy dispersion.

The measured impact points of the scattered proton built from the information of fibre and tile hits in one pot are used to reconstruct a local track in that pot. Since local tracks are reconstructed from the combination of all hits, a single event can contain more than one local track in a single pot. The track gives a local intercept and slopes in the x and the y axis, θ_x^{local} and θ_y^{local} , respectively. The two most forward local tracks, one in each VFPS station, are used to reconstruct the global track. The transverse intercepts x and y of the global track are determined at the position halfway between the two stations (at $z = 220$ m). The information on the position and the angle of the global track determines $x_{\mathcal{P}}$ and the horizontal and vertical scattering angles of the scattered proton, θ_x and θ_y , at the interaction point. The relation between the set of variables at the VFPS and those at the interaction point is given by the beam transport matrices describing the optical functions between the H1 interaction point and the spectrometer [24]. At the time of writing the present document, the reconstruction procedure of the kinematics was not yet fully operational.

3.2.3 The Level 1 Trigger

As stated before, the tile information is used for triggering purposes. Two L1 trigger elements for the VFPS are send to the central trigger, each for a single detector station. The trigger

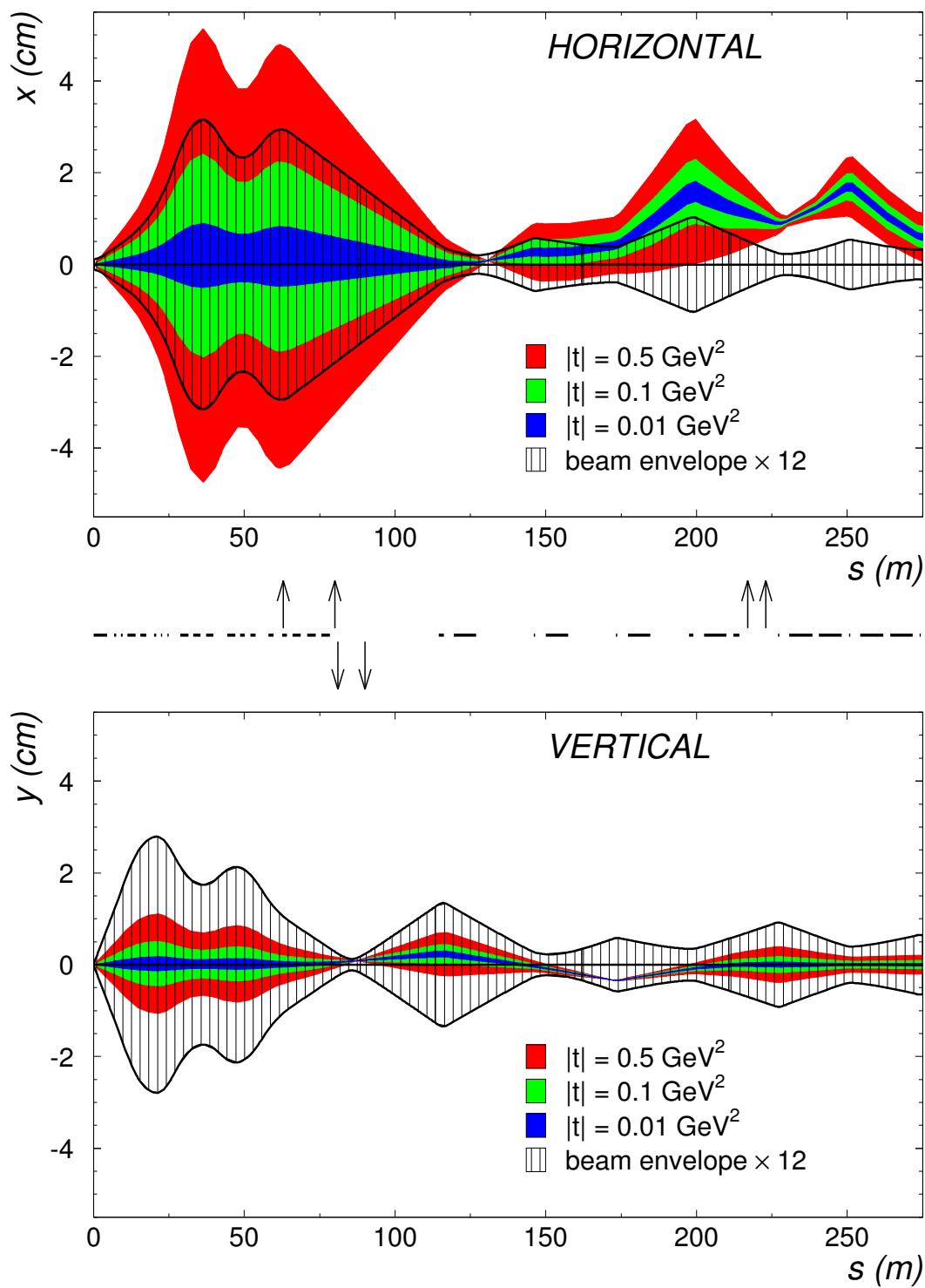


Figure 3.16: Horizontal (top) and vertical (bottom) projections of scattered proton trajectory in x and y coordinate for three different values of t for $x_p = 10^{-2}$ as a function of the distance from the interaction point ($s = 0$). The hatched area represents 12 times the beam envelope. Horizontal dashes in-between indicate locations of magnets. Vertical arrows represent FPS (two horizontal and two vertical stations) and VFPS station locations.

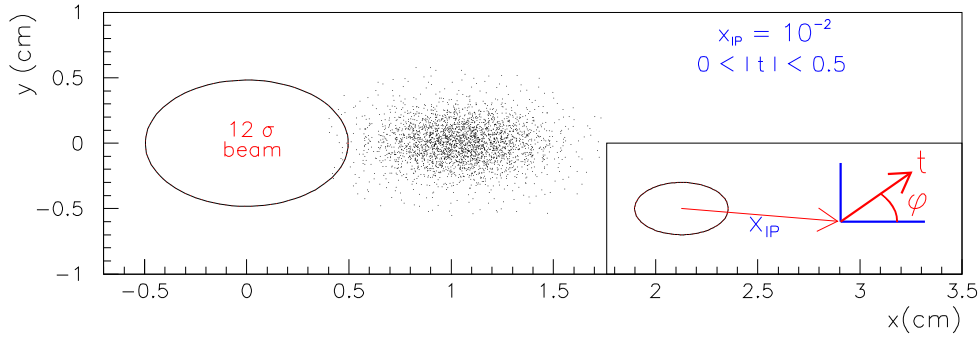


Figure 3.17: Simulation of the transverse projection of the proton deviations from the beam envelope at 220 m that lost 1% of their energy at $0 < |t| < 0.5 \text{ GeV}^2$.

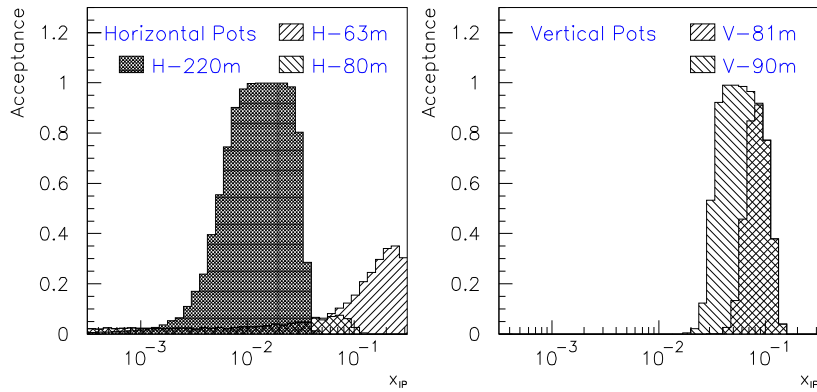


Figure 3.18: Simulated acceptance of the FPS and VFPS (H-220m) stations as a function of the $x_{\mathcal{P}}$.

element is positive if tiles in at least three out of four planes in a single pot fired. Both VFPS elements are combined with the trigger information from other H1 subdetectors to form four L1 subtriggers responsible for triggering elastic diffractive events. A subsample of events studied in section 4.3.2 is triggered by the coincidence between VFPS and SpaCal IET trigger signals.

3.2.4 The Complementarity of VFPS And FPS

The H1 experiment contains other forward proton spectrometers (FPS) made of two stations with a horizontal approach to the beam located at 63 and 80 m, and two stations with a vertical approach at 81 and 90 m. A complementary behaviour of the spectrometers in terms of acceptances as a function of $x_{\mathcal{P}}$ is shown in Fig. 3.18, based on the fast simulation. The acceptance of the FPS stations is represented by the overlap of the two FPS histograms in the horizontal or in the vertical directions. FPS-H presents a low acceptance in an extended $x_{\mathcal{P}}$ range $0.0001 \leq x_{\mathcal{P}} \leq 0.1$ (around 5%). FPS-V presents a large acceptance in the large $x_{\mathcal{P}}$ region $0.06 \leq x_{\mathcal{P}} \leq 0.2$. The VFPS were installed to complement these acceptances by a high acceptance in the region $0.005 \leq x_{\mathcal{P}} \leq 0.01$.

Chapter 4

Study of the Very Forward Proton Spectrometer

With the regain of interest for diffraction that took place in the 1990's with HERA data, H1 decided to install a new proton spectrometer, with high acceptance to take the benefit of the HERA II phase luminosity increase. Such a device should help to reduce the uncertainty in diffractive measurement due to background contribution of proton dissociation and allow precise t dependence measurement.

The VFPS detectors have been designed between the years 2000 and 2001 [24], together with the bypass of the cold elements from the proton beam pipe. The detectors have been built in 2002, cosmic tests performed at the end of the year. The installations of the bypass, both VFPS pots and the beam monitor (see section 4.2.3) have been completed during 2003 together with the detector readout testing. After a short period of data taking, the fibres of the readout cables were found to be darkened by the radiation from the beam in 2004. The cables were then replaced and put under the tunnel flooring to be shielded. Data taking restarted in 2005 until a problem of fixation of the detector into the Roman pot of one station took place due to the violence of the emergency retraction system that had to be used. After that repair the data taking went smoothly except for the needed replacement of the broken motor axis in one of the stations in the summer 2006.

In this chapter we present the first study of the data collected by H1 with the Very Forward Proton Spectrometer, based on the data from the H1 experiment during the running periods of years 2006 and 2007, when the VFPS was operating smoothly. Before studying inclusive events in the VFPS, three technical aspects are discussed in this section. The first step towards the estimate of the VFPS acceptance is to study the trigger tile efficiencies on which is based the H1 subtrigger element we use in the following. The effect of the proton beam horizontal position around 200 m from the interaction point on the rate of diffractive events tagged by the VFPS is then studied. The Beam Position Monitor placed between the two VFPS stations to measure the proton beam position in x and y is then subject to a calibration procedure.

4.1 Trigger Tile Efficiencies

The efficiency of VFPS trigger tiles for the 2006 and 2007 period is calculated using local tracks. In the ideal case, when the scattered proton hits the VFPS detectors, it leaves in total

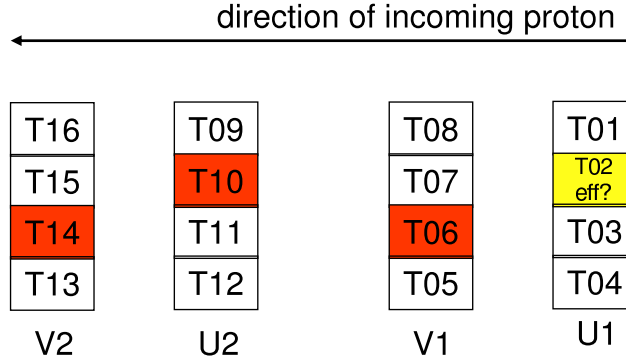


Figure 4.1: Tile mapping of the two detectors in a single VFPS station.

8 hits in the trigger tiles, one hit in each u and v plane of each pot. The data sample for the efficiency calculation is a selection of all events during the period of years 2006 and 2007 with the VFPS 1 and the VFPS 2 trigger element fired (a coincidence in two VFPS stations with at least one hit in 3 out of 4 planes). Thus, all events saved on the tape with a VFPS trigger are used, there is no requirements on the ep interaction in the main H1 detector. For the efficiency calculation in a given pot, a single fibre cluster of hits in each of the u and v planes (i.e. a single local track) is required in the other pot.

The tile mapping scheme of detectors in a single VFPS station is depicted in Fig. 4.1. As an example, to compute the efficiency for the tile $T02$, the following criteria are required:

- The tile multiplicity in the v coordinate is equal to one per plane. Tiles in plane $V1$ and $V2$ that fired are aligned.
- One fibre cluster of hits exists in each of the v planes and the reconstructed line connecting these two clusters has the slope $\theta_v^{local} < 25$ mrad.
- The $U2$ plane contains only one tile hit, $T10$ (this implies that there is only a single trigger hit in $U2$).
- The $U1$ plane contains exactly one reconstructed fibre cluster of length of two fibre rows at most. Moreover, the fibre roads associated to the cluster must not lay at the edges of the tiles. With the fibre labeling as shown in Fig. 3.15 (interval $[0, 31]$), the allowed range corresponds to fibre roads between 2 and 29.

The efficiency, ϵ_{02} , for the $T02$ tile is then computed as the ratio

$$\epsilon_{02} = \frac{N_{T02}}{N_{sel/02}} \quad (4.1)$$

of selected events with the additional condition of having the tile $T02$ in the plane $U1$ fired, N_{T02} , to the number of selected events, $N_{sel/02}$, with the above requirements. Number of selected events, N_{T_i} , with a hit in the corresponding tile i , is shown in Fig. 4.1 for each year. Because the tile 4 in each u and v plane is usually the furthest from the centre of the beam in the y direction (in Fig. 3.14 they correspond to smallest tiles in the detector edges), the number of detected particles in these edge tiles is very limited, compared to rest of tiles. However, most

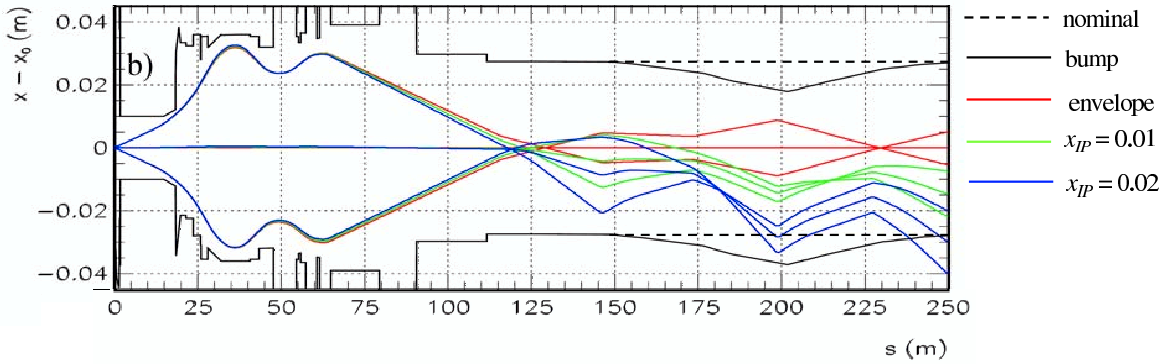


Figure 4.2: Horizontal projection of the beam pipe relative to the beam position as a function of the distance from the interaction point. Three different curves for the scattered protons of constant x_{IP} values represent different angles in the x projection, $\theta_x = -0.5, 0.0, +0.5$ mrad, at the interaction point. The 3-point beam bump of 10 mm at 200 m is represented by the solid line between 150 and 250 m.

of diffractive events are detected in central tiles (marked as no.2) due to the exponential fall of the diffractive $d\sigma/dt$ cross section.

The year averaged tile efficiencies are shown in Tab. 4.2, where the given error, $\delta\epsilon_i$, corresponds to the purely statistical error computed as

$$\delta\epsilon_i = \frac{1}{N_{sel/i}} \sqrt{N_{T_i} \left(1 - \frac{N_{T_i}}{N_{sel/i}}\right)} \quad (\times 100\%). \quad (4.2)$$

Tile efficiencies estimated for the tile 4 are computed on the basis of limited statistics, and as such are not reliable. Their values are therefore omitted in the table.

Since the VFPS level 1 subtrigger is positive if at least three out of four tiles fired, the global VFPS trigger efficiency, made of the combination of all tile efficiencies, is higher than 98%.

4.2 The Proton Beam Optics

The beam optics has been studied during the data taking in 2006 to optimise the VFPS acceptance. For that purpose, dedicated changes in the proton beam optics settings in the region of the VFPS stations have been performed by the HERA team. As explained in the section 3.2.2, the x_{IP} and t region reached by the VFPS depends on several factors. The distance of the pot with respect to the beam governs the acceptance of low x_{IP} values. The closer the pot can reach, the more protons with smaller energy losses can reach the detector. On the other hand, the access to high x_{IP} events is limited by the horizontal dimension of the proton beam pipe between the interaction point and the VFPS location.

The simulation of proton trajectories in the horizontal plane of the forward region of H1 is shown in Fig. 4.2 for energy losses of 1% and 2%, corresponding to $x_{IP} = 0.01$ and 0.02, respectively. Given the VFPS position at ~ 220 m and assuming the nominal beam position (dashed line), protons with $x_{IP} > 0.02$ are deflected into the beam pipe at ~ 200 m and thus can

2006				
VFPS 1 planes				
Tile	U1	V1	U2	V2
1	$\frac{16024}{16308}$	$\frac{13497}{13806}$	$\frac{19627}{20080}$	$\frac{11676}{12131}$
2	$\frac{283450}{288196}$	$\frac{215524}{219157}$	$\frac{266818}{271652}$	$\frac{230997}{236414}$
3	$\frac{4606}{5088}$	$\frac{656}{682}$	$\frac{2648}{2763}$	$\frac{568}{635}$
4	0	0	0	$\frac{1}{1}$
VFPS 2 planes				
Tile	U1	V1	U2	V2
1	$\frac{18027}{18296}$	$\frac{26520}{6733}$	$\frac{24077}{24729}$	$\frac{25659}{5988}$
2	$\frac{373216}{377296}$	$\frac{383991}{390783}$	$\frac{394547}{404621}$	$\frac{283543}{291363}$
3	$\frac{4953}{5413}$	$\frac{3416}{3586}$	$\frac{4123}{5432}$	$\frac{1701}{1788}$
4	$\frac{2}{2}$	$\frac{18}{20}$	$\frac{2}{2}$	$\frac{11}{11}$

2007				
VFPS 1 planes				
Tile	U1	V1	U2	V2
1	$\frac{5974}{6094}$	$\frac{16556}{16898}$	$\frac{8764}{9008}$	$\frac{13993}{14385}$
2	$\frac{114259}{116179}$	$\frac{74800}{76228}$	$\frac{108742}{110785}$	$\frac{83665}{85803}$
3	$\frac{2488}{2733}$	$\frac{143}{146}$	$\frac{1294}{1385}$	$\frac{147}{163}$
4	$\frac{2}{2}$	0	$\frac{1}{1}$	0
VFPS 2 planes				
Tile	U1	V1	U2	V2
1	$\frac{5091}{5172}$	$\frac{10592}{10857}$	$\frac{7395}{7627}$	$\frac{8858}{9323}$
2	$\frac{119472}{120992}$	$\frac{118508}{120634}$	$\frac{128947}{131894}$	$\frac{92293}{94942}$
3	$\frac{2582}{2968}$	$\frac{732}{756}$	$\frac{1768}{2413}$	$\frac{438}{459}$
4	$\frac{8}{9}$	$\frac{7}{7}$	$\frac{8}{10}$	$\frac{3}{3}$

Table 4.1: Statistics used in the tile efficiency calculation. Values represent the ratio of the number of selected events with a hit in the tile T_i for which the efficiency is calculated, N_{T_i} , over the number of selected events, $N_{sel/i}$, as described in text: $\frac{N_{T_i}}{N_{sel/i}}$.

2006				
VFPS 1 planes				
Tile	U1	V1	U2	V2
1	98.26 ± 0.10	97.76 ± 0.13	97.74 ± 0.10	96.25 ± 0.17
2	98.35 ± 0.02	98.34 ± 0.03	98.22 ± 0.03	97.71 ± 0.03
3	90.53 ± 0.41	96.19 ± 0.73	95.84 ± 0.38	89.45 ± 1.22
4	-	-	-	-
VFPS 2 planes				
Tile	U1	V1	U2	V2
1	98.53 ± 0.09	96.84 ± 0.21	97.36 ± 0.10	94.51 ± 0.29
2	98.92 ± 0.02	98.26 ± 0.02	97.51 ± 0.02	97.32 ± 0.03
3	91.50 ± 0.38	95.26 ± 0.35	75.90 ± 0.58	95.13 ± 0.51
4	-	-	-	-

2007				
VFPS 1 planes				
Tile	U1	V1	U2	V2
1	98.03 ± 0.18	97.98 ± 0.11	97.29 ± 0.17	97.27 ± 0.14
2	98.35 ± 0.04	98.13 ± 0.05	98.16 ± 0.04	97.51 ± 0.05
3	91.04 ± 0.55	97.95 ± 1.17	93.43 ± 0.67	90.18 ± 2.33
4	-	-	-	-
VFPS 2 planes				
Tile	U1	V1	U2	V2
1	98.43 ± 0.17	97.56 ± 0.15	96.96 ± 0.20	95.01 ± 0.23
2	98.74 ± 0.03	98.24 ± 0.04	97.77 ± 0.04	97.21 ± 0.05
3	86.99 ± 0.62	96.83 ± 0.64	73.27 ± 0.90	95.42 ± 0.98
4	-	-	-	-

Table 4.2: Tile efficiencies (in %) for the VFPS 1 and VFPS 2 detectors for 2006 and 2007 high energy periods.

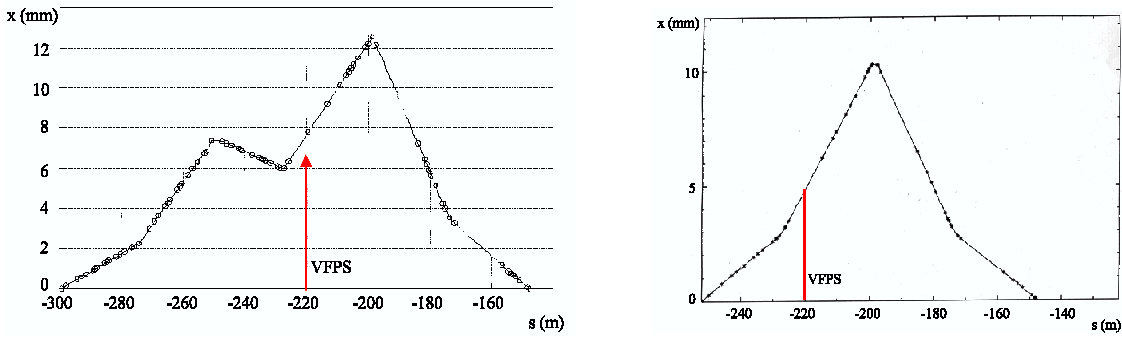


Figure 4.3: Proton beam bump (in mm) as a function of the distance from the interaction point (in m), left) 4-points, right) 3-points.

not be detected in the VFPS. This effect originates from the strong beam focusing in the vertical direction at approximately 180 m - the resulting defocusing in the horizontal direction at 200 m is too large to keep in the beam pipe all scattered protons with an energy loss above 2%. A solution to this problem is to displace the proton beam locally in the x direction (solid line in Fig. 4.2) to allow high x_P protons to hit the detector. To quantify this effect on the detector acceptance, a study of different proton orbits have been performed, as described below.

4.2.1 Proton Beam Orbits

The proton beam travels in the beam pipe on stable orbits defined by the settings of the HERA magnets. Orbits can be locally adjusted in horizontal and vertical directions by changes in the settings of certain magnets. For the VFPS acceptance study, the horizontal change in orbit on the way to the VFPS pots is of a particular interest. Depending on the magnets needed to steer away the beam, a 3-point (three magnets in action) or a 4-point (four magnets) bump is defined. A 4-point bump contains changes in the magnets (called correction magnets or CX) at 148, 200, 252 and 299 m from the interaction point, whereas the 3-point bump uses magnets at 148, 200 and 252 m. Examples of 3- and 4- point bumps leading to an additional x offset between 150 and 300 m from the interaction point are shown in Fig. 4.3. The maximum amplitude which can be achieved at 200 m is $\Delta x \simeq 12$ mm (corresponding to $\Delta x = 8$ mm at 220 m), with the 4-point bump, as measured by the beam position monitor (described in section 4.2.3). The beam is first steered up to $x = -4.8$ mm using an automatic procedure and then, during the first part of the run, carefully adjusted to higher offsets.

4.2.2 Optimisation of the Beam Optics

To quantify and optimise the effect of different proton orbit positions on the VFPS acceptance, the proton beam position at 220 m in the x direction has been studied in 2006. The raw VFPS acceptance, which is not corrected for background in the main H1 detector, A_{VFPS} , is defined as the ratio of the number of events tagged by the VFPS detector, N_{VFPS}^D , to the number of all

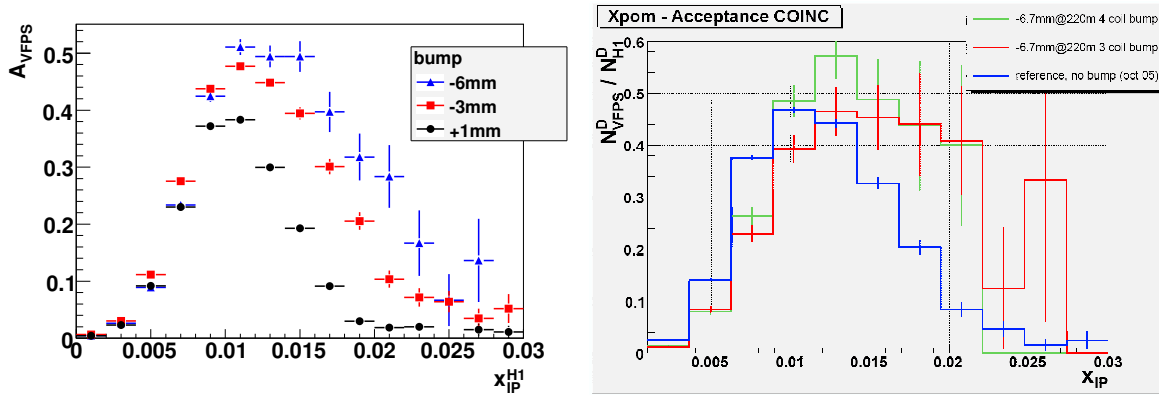


Figure 4.4: Raw VFPS acceptance as a function of x_{IP} as measured by the central H1, for different values of proton beam orbits (left) and for the 3- and 4-point bumps (right).

inclusive diffractive event candidates detected by the H1 detector, N_{H1}^D ,

$$A_{VFPS} = \frac{N_{VFPS}^D}{N_{H1}^D}. \quad (4.3)$$

The raw acceptance was determined from a sample of diffractive event candidates with the electron detected in the SpaCal and the VFPS pots in the working position, close to the beam. Events in the denominator have been selected based on a large rapidity gap in events. The cuts applied for the selection of diffractive events are those described in section 4.3.2. Events in the nominator in eq. (4.3) have to be in addition triggered by VFPS trigger elements in both stations (trigger element requires at least 3 out of 4 trigger planes to fire in a VFPS station, see section 3.2.3). Fig. 4.4, left, shows the effect of different bumps on the VFPS acceptance in the x_{IP} variable. The higher the bump in the negative x direction (i.e. towards inside the HERA ring), the higher acceptance of the VFPS in the region of larger x_{IP} values. The right plot shows that the acceptance does not depend on the 3-point or 4-point bump configuration for the same value of the beam bump at 220 m. After these tests, it was agreed by the H1 and the HERA representatives to set the beam bump to -6 mm at 220 m as the default proton beam configuration for the remaining running period in 2006 and 2007. But in reality, as shown in Fig. 4.6 left, the x position has still changed slightly after that agreement (run number $\gtrsim 480,000$).

4.2.3 The Proton Beam Position Monitoring

The proton beam positions in the x and y directions are measured by beam position monitors (BPM) installed next to the each quadrupole magnet. Next to a horizontally (vertically) focusing quadrupole, the beam monitor measures the horizontal (vertical) direction [31]. Beam monitors consist of two 395 mm long antennas installed against each other at both sides of the beam pipe (Fig. 4.5) and covering 36° in the azimuthal angle, coupling electromagnetically to the frequency spectrum of the beam. A single antenna mounted on the vacuum chamber is shown in Fig. 4.5, left. Monitors are designed to get a maximum sensitivity with a minimum disturbance of the beam. The width of each antenna, 17 mm, is the optimum balance between strong output signals (wider antennas) and high position sensitivity (thinner antennas) [32]. Two additional

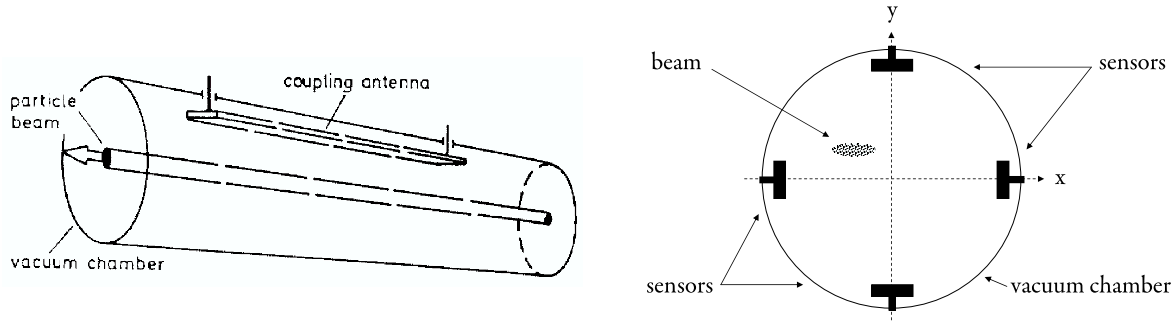


Figure 4.5: left) Antenna of a beam position monitor; right) The principle of the beam position measurement with the distance-sensitive elements.

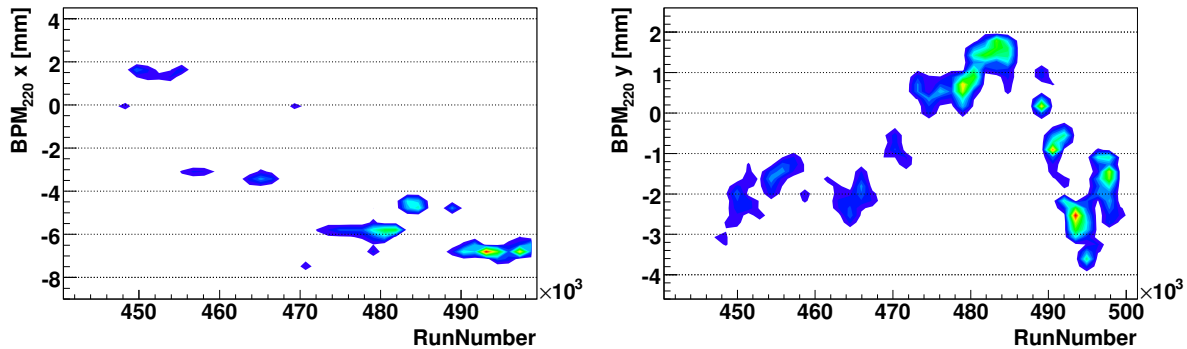


Figure 4.6: Positions of the proton beam at 220 m during years 2006 and 2007, in the x and y directions, as measured by the horizontal and vertical BPMs.

BPMs have been installed at 220 m, between the two VFPS stations, at the same time as the VFPS, to monitor the proton beam in both x and y directions at that place.

The spectrum of the proton beam orbit positions varies with the time for the continuous luminosity optimisation operated by the HERA team. Fig. 4.6 shows the beam position in the x and y directions at 220 m measured by the BPMs, as a function of the H1 run number. As can be seen, the absolute position in the x coordinate varies between +2 and -8 mm and the absolute y position varies between +2 and -4 mm. The large variation in x corresponds to the optimisation of the VFPS acceptance as discussed above.

4.2.4 Calibration of the Beam Position Monitor at 220 m

Calibration of BPM220Y

The calibration of the BPM220 measurement in the y direction (BPM220Y) has been performed using local tracks in the VFPS stations. In good approximation, the y distribution of local track intercepts in a VFPS station is expected to peak at the y position of the beam. Fig. 4.7a shows the distribution of track intercepts in VFPS 1 in the xy plane for one luminosity fill and Fig. 4.7b its projection in the y axis for two different luminosity fills (the beam orbit is assumed

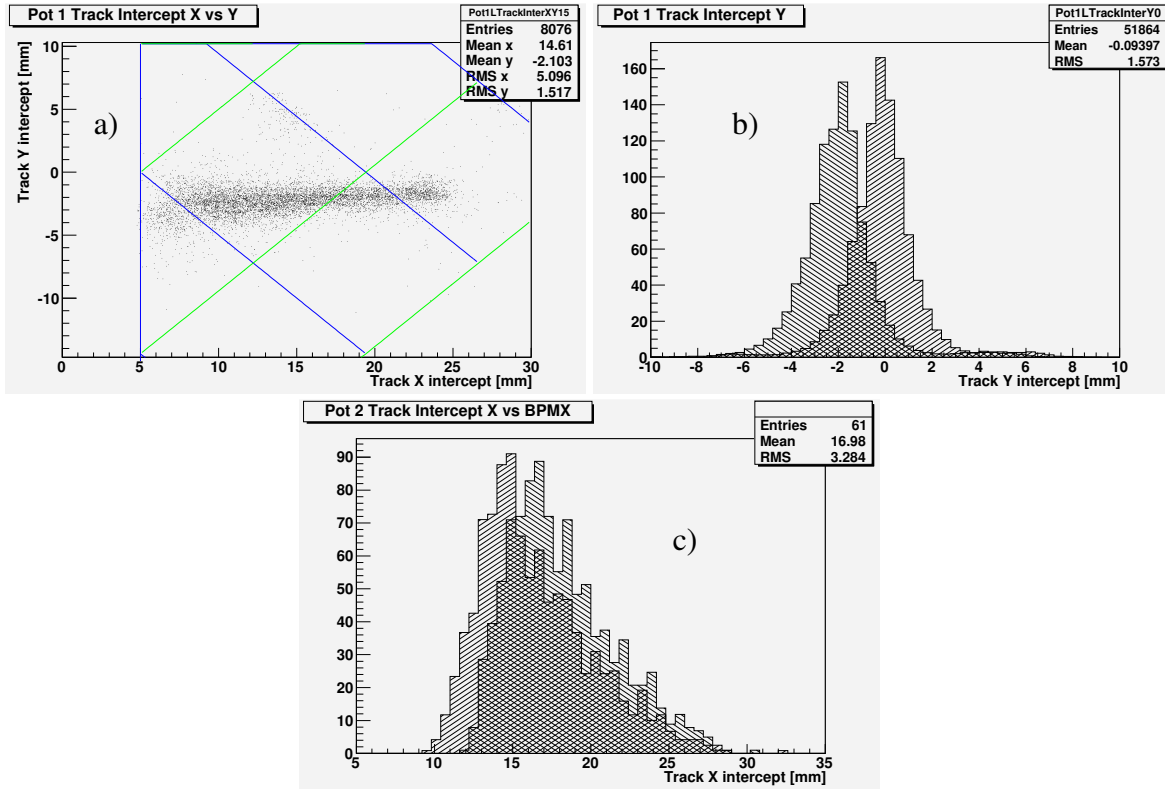


Figure 4.7: Distribution of local track intercepts in VFPS 1 in the xy plane (a); distribution of local track intercepts in the y direction for two different luminosity fills (b); distribution of local track intercepts in the x direction (c) for two different beam bumps (-6.9mm and -4.8mm).

to be stable during a luminosity fill). The mean of the y coordinate of local tracks in a single luminosity fill is then used as a measurement of the y beam position in that fill. The correlation between the difference of the mean of local tracks and the BPM y position versus the BPM y position is shown in Fig. 4.8, left. As can be seen, extremities of the orbit position give the largest deviation from values measured in the VFPS pot. The BPM was then calibrated in y using the linear fit $y'_{BPM} = A \cdot y_{BPM} + B$, where A and B are the fit parameters and y_{BPM} is the value from the beam position monitor. After this first calibration step, the same difference in y for different positions in the x direction (Fig. 4.9, left) shows that there is a correlation between the x and the y BPM measurement. Therefore, a fit of the form

$$y'_{BPM} = A \cdot y_{BPM} + B + C \cdot x_{BPM} \quad (4.4)$$

was performed leading to the fit parameters values $A = 0.53$, $B = -0.79$ mm and $C = -0.05$. The calibrated BPM positions in y and x are shown in Fig. 4.8, right and 4.9, right, respectively, which by construction have averages at $y_{POT} - y_{BPM} = 0$. Projecting this distribution, the resulting BPM resolution in the y direction amounts to $210 \mu\text{m}$, as shown in Fig. 4.10.

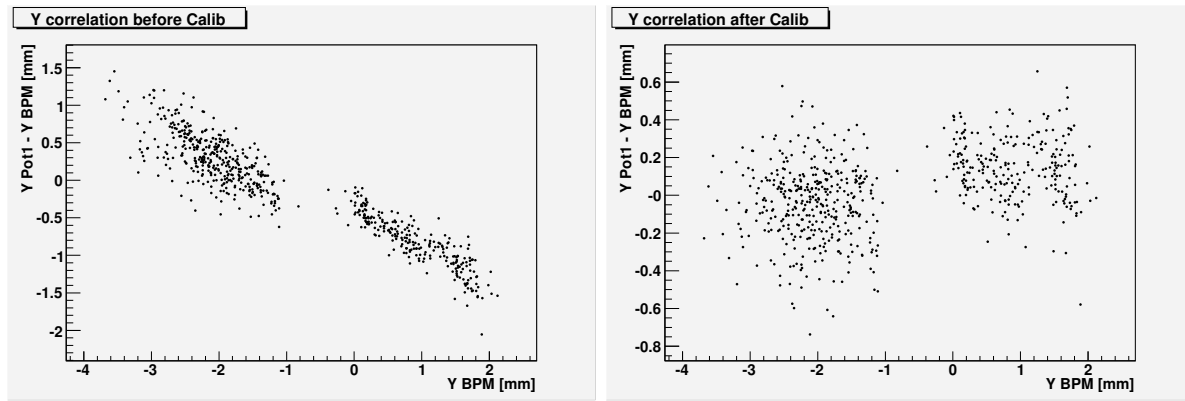


Figure 4.8: Difference between the local track position in VFPS 1 and the value of proton beam monitor at 220 m, in the y coordinate, for different values of BPM in the y direction. left) before the calibration; right) after the calibration.

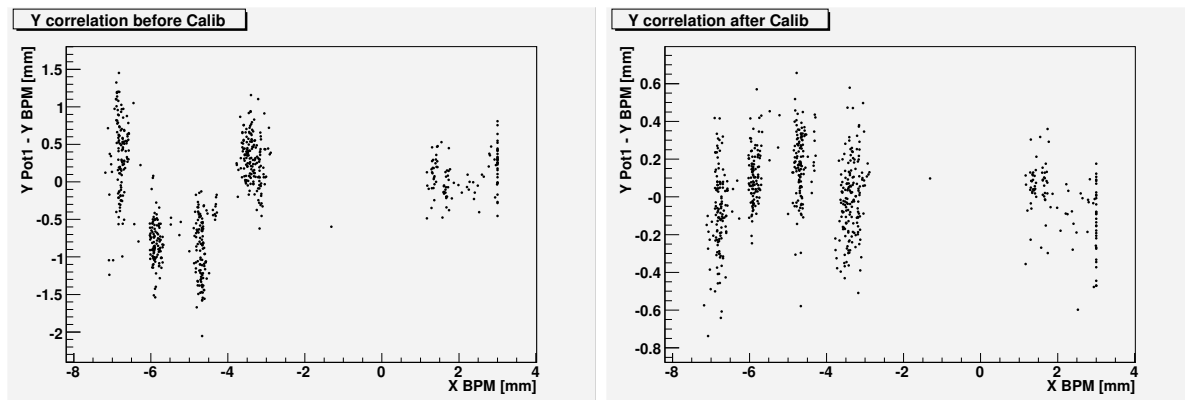


Figure 4.9: Same as in Fig. 4.8 but in different values of BPM in the x direction.

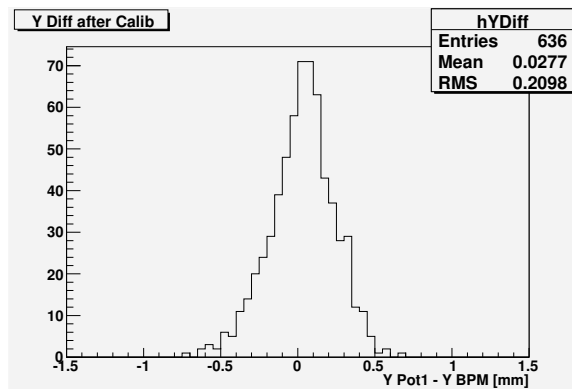


Figure 4.10: Difference in the y direction between the calibrated proton beam monitor at 220 m and the local track position in VFPS 1.

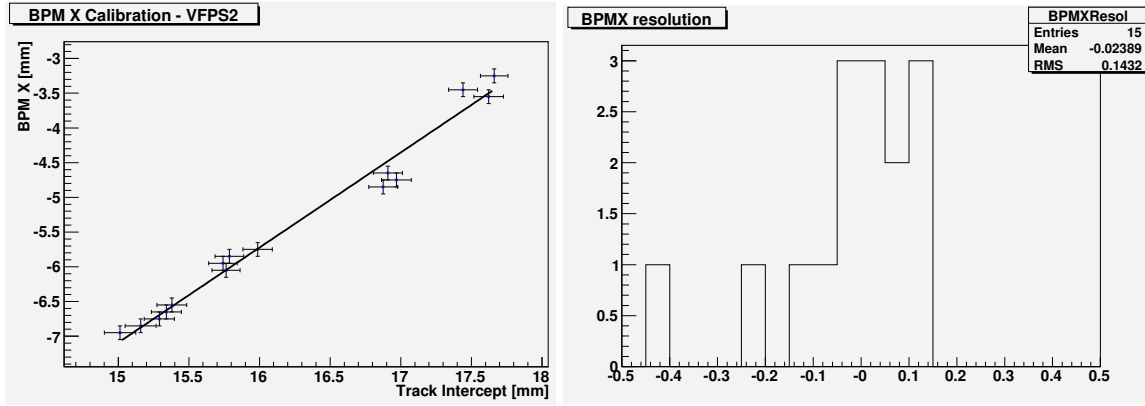


Figure 4.11: Calibration of the BPM in the x direction using local tracks in the single VFPS pot: correlation between the x beam position measured by the BPM220X and the local track intercept (left); difference in the x direction between the calibrated proton beam monitor at 220 m and the local track position in VFPS 1 (right).

Calibration of BPM220X

The calibration of the BPM220 in the x direction is not as simple. The x distributions of the local track intercept (Fig. 4.7c) do not peak at the beam value but is in a good approximation linearly dependent of the x_P values of the scattered protons. The calibration method is then the following: for a fixed value of x_P , the x intercept value of local tracks in one VFPS station should be a linear function of the x beam position. Taking into account the fact that the position of the VFPS station changes with time with respect to its parking position, and applying a cut on selected diffractive events (for selection details, see section 4.3.2) on x_P reconstructed by the central detector between 0.01 and 0.02, the track intercepts in x are presented as a function of the BPM220X in Fig. 4.11, left. Note that to avoid ambiguities, only events with a single local track have been kept in the present data selection. This procedure allows us to estimate the factor A of the calibration function

$$x'_{BPM} = A \cdot x_{BPM} + B, \quad (4.5)$$

while the offset term, B , remains unknown. A fit procedure leads to $A = 0.76 \pm 0.06$. The difference $x'_{BPM} - x_{BPM}$ is shown in Fig. 4.11, right. However, the resolution ($\sim 140 \mu\text{m}$), is hard to be estimated given the low number of points, but it is compatible or lower to the $210 \mu\text{m}$ found for the BPM220Y.

Using calibrated values of BPM220X allows to determine more precisely the proton beam bump that needs to be put into the simulation to describe the VFPS acceptance in data.

4.3 Study of Inclusive Diffraction With Tagged Proton

The aim of this section is to present the study of the VFPS performance using the inclusive elastic diffractive data,

$$ep \rightarrow eXp, \quad (4.6)$$

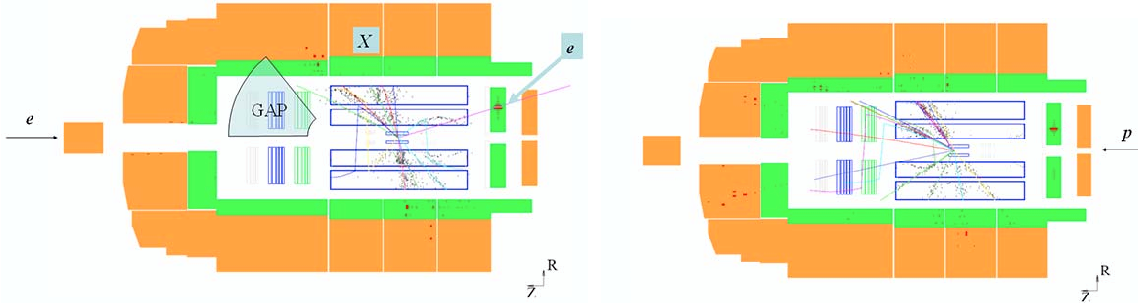


Figure 4.12: Example of an diffractive event selected by LRG method (left) and with the scattered proton tagged by the VFPS (right).

where the scattered proton is tagged in the VFPS and X represents a hadronic system emanating from the photon dissociation. The scattered electron is detected in the backward calorimeter, SpaCal.

Different experimental approaches can be used to select the diffractive sample at the H1 experiment. In the following, we will make use of two among them. In Large Rapidity Gap (LRG) method, diffractive events are selected on the basis of largest gap between the X system and the direction of the outgoing proton (see Fig. 4.12). The scattered proton is not detected and therefore the selected sample may include a contribution from the non-diffractive DIS $ep \rightarrow eX$ and from diffractive processes of the type $ep \rightarrow eXY$, where the proton dissociates into a hadronic system Y . The sample selected by the LRG method will be used as a reference sample in the process of the VFPS acceptance determination.

The second method is to directly tag the scattered proton using a proton spectrometer (here the VFPS). The tagging device restricts further the measurement in the (x_P, t) plane, but an advantage of this method is to give a sample free of the DIS and proton dissociation backgrounds.

The reference data sample of inclusive diffractive event candidates in the DIS regime is selected independently of a possible activity in the VFPS

- to control the quality of the diffractive sample and of its description by the MC simulation;
- to study the VFPS acceptance, whose estimate is based on the ratio of the VFPS tagged events to the total data sample.

4.3.1 Kinematic Reconstruction And Resolution

The kinematic variables Q^2 , y , x and W , as defined in section 2.1.1, are reconstructed using the measurement of the scattered electron as

$$Q^2 = 4E_{e'}E_e \cos^2 \frac{\theta_{e'}}{2}, \quad (4.7)$$

$$y = 1 - \frac{E_{e'}}{E_e} \sin^2 \frac{\theta_{e'}}{2}, \quad (4.8)$$

$$x = \frac{Q^2}{ys}, \quad (4.9)$$

$$W = \sqrt{ys - Q^2}, \quad (4.10)$$

where $E_{e'}$ and $\theta_{e'}$ are the energy and the polar angle of the scattered electron, respectively. As the scattered proton (or more generally the Y system) is leaving the detector through the beam pipe and is separated by a gap in rapidity from the X system, all activity in the main detector can be attributed to the X system. The hadronic final state X is measured with the forward and central tracking system and the SpaCal and LAr calorimeters. The information of tracks and clusters are combined to achieve the best precision available [46]. The sum of all four-vectors, p_X , of these combined objects is used to calculate the invariant mass M_X of the X system,

$$M_X = \sqrt{p_X^2}. \quad (4.11)$$

The momentum fraction β of the pomeron carried by the interacting quark is then reconstructed as

$$\beta = \frac{Q^2}{Q^2 + M_X^2}. \quad (4.12)$$

The $x_{\mathbb{P}}$ variable is reconstructed using the hadronic system and the scattered electron informations as

$$x_{\mathbb{P}} = \frac{\sum_{X,e'}(E + p_z)}{2E_p}, \quad (4.13)$$

where E_p is the energy of the incoming proton and the sum runs over the all detected hadronic final state particles and the scattered electron. We have chosen to reconstruct $x_{\mathbb{P}}$ using eq. (4.13) because of the best resolution. The relative resolution of the reconstructed $x_{\mathbb{P}}$ variable is computed as

$$\text{res} = \text{RMS} \left(\frac{x_{\mathbb{P},\text{gen}} - x_{\mathbb{P},\text{rec}}}{x_{\mathbb{P},\text{gen}}} \right) \quad (4.14)$$

and is shown in Fig. 4.13, left, based on the sample of elastic diffractive events (see section 4.3.4). The resolution in the region of $x_{\mathbb{P}} < 0.05$ is between 18% and 20%. The relative $x_{\mathbb{P}}$ bias is computed as the mean value of deviations for each bin in $x_{\mathbb{P}}$,

$$\text{bias} = \left\langle \frac{x_{\mathbb{P},\text{gen}} - x_{\mathbb{P},\text{rec}}}{x_{\mathbb{P},\text{gen}}} \right\rangle. \quad (4.15)$$

As shown in Fig. 4.13, right, the bias ranges between 12% and 40% and worsens towards the higher $x_{\mathbb{P}}$ values. The high bias at large $x_{\mathbb{P}}$ values is due to misreconstruction of the X system, which is boosted to the forward detector region and part of the hadronic system escapes the detection. In Fig. 4.14, the spread in $x_{\mathbb{P}}$ is shown for pomeron and reggeon contributions separately for two different η_{max} limits ($\eta_{\text{max}} < 2.5$ and $\eta_{\text{max}} < 3.2$). In the present study a lower $x_{\mathbb{P}}$ bias is maintained by restricting the rapidity extent of the X system to $\eta_{\text{max}} < 2.5$. This cut limits $x_{\mathbb{P}}$ region to $x_{\mathbb{P}} \lesssim 0.03$ (corresponding to $\log x_{\mathbb{P}} \lesssim -1.5$ in Fig. 4.14), where the bias is below 35% (Fig. 4.13). The large rapidity gap between the photon dissociation system and the direction of outgoing proton also minimises the contribution from the non-diffractive DIS.

4.3.2 Data Selection of the Reference Sample

Run Preselection

The data which will be used in the analysis are first preselected. The run (or a fraction of the run) is accepted only if:

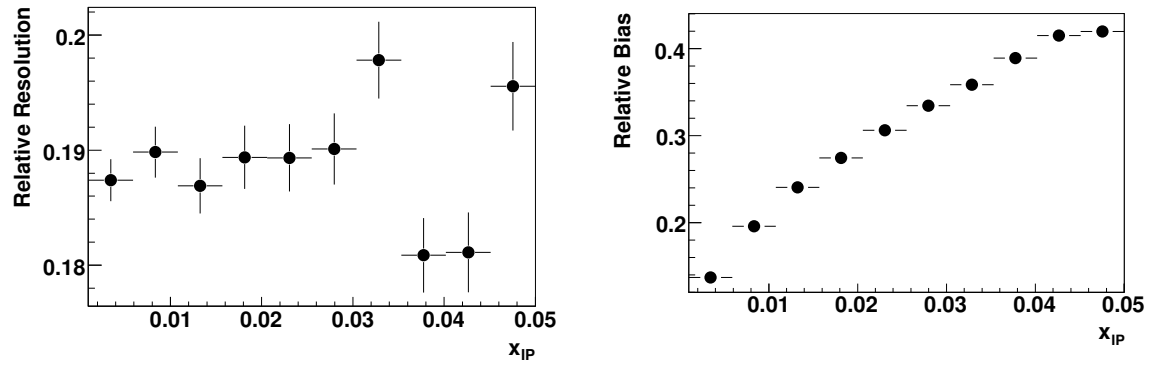


Figure 4.13: Relative resolution and bias of the x_{IP} variable.

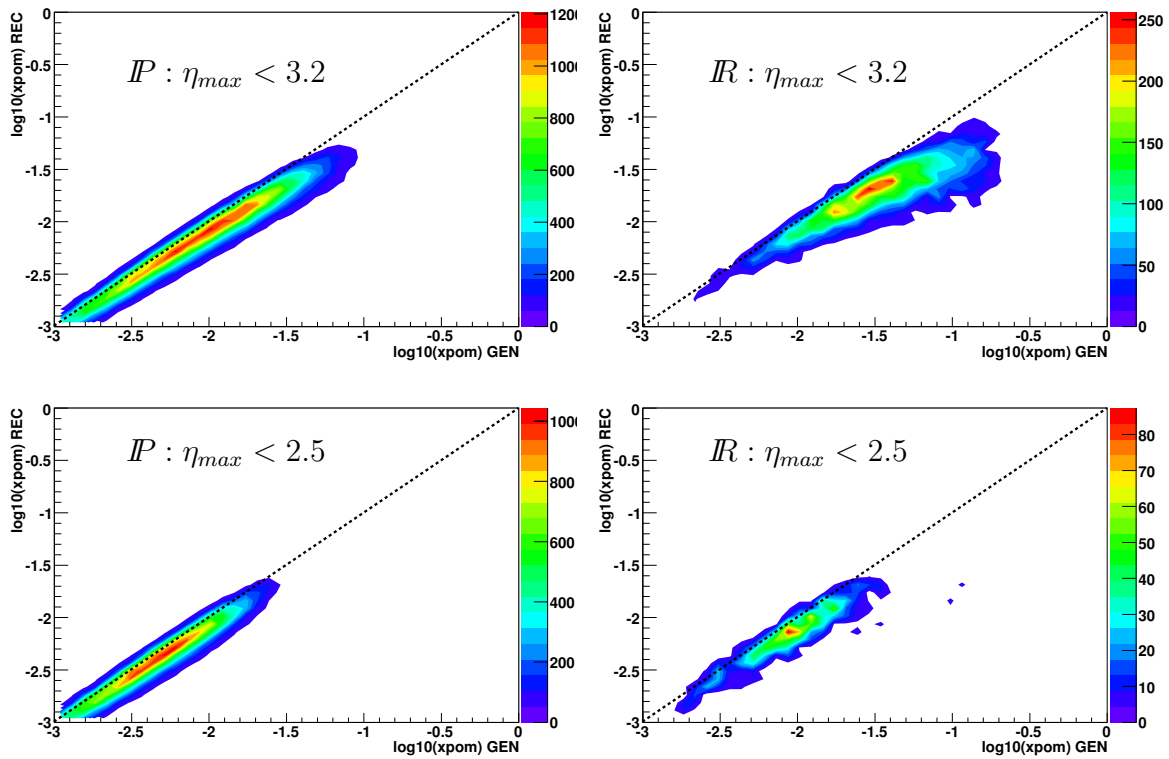


Figure 4.14: Spread in the x_{IP} variable for inclusive processes with pomeron (IP) and reggeon (IR) exchange for two different η_{max} limits: < 3.2 and < 2.5 .

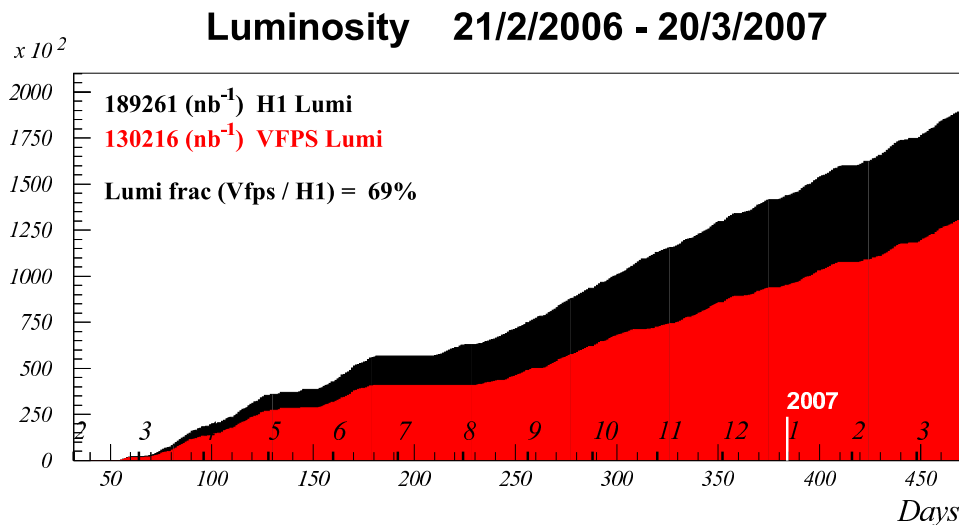


Figure 4.15: Integrated luminosity (in nb⁻¹) delivered to the H1 experiment (red+black) compared to the fraction of luminosity for the periods with active VFPS detectors (red) as a function of year days in 2006 and 2007. Months are also indicated on the plot.

- both VFPS pots are in the final position close to the beam.
- high and low voltage is supplied to the CJC1, CJC2, SpaCal, LAr, VFPS detectors, luminosity system and to the time of flight counters;

The integrated luminosity delivered to H1 experiment during 2006 and 2007 when the VFPS pots were in the operating position is 130.2 pb⁻¹. The integrated luminosity of 189.2 pb⁻¹ delivered to H1 during this period is compared to the period with active VFPS pots in Fig. 4.15. The VFPS was active for 69% of the stable luminosity running, reasonably high when considering the time (~ 20 min for each fill¹) to drive the pots close to the proton beam and the technical problems reported at the beginning of this chapter.

As stated before, two distinct samples are being analysed: a reference sample obtained using the LRG method to determine the VFPS acceptance and a subsample of it with the proton tagged by the VFPS. The selection cuts are discussed below.

Subtrigger Utilisation

The LRG diffractive sample is triggered by the subtrigger *S03*, which is used to select inclusive DIS events and is defined as

```
S03 L1: SPCLe_IET>2 && ToF&VETO
      L2: SPCL_R30
```

The trigger element *SPCLe_IET>2* triggers on an electromagnetic cluster with an energy above the threshold of 6 GeV in the outer SpaCal (see section 3.1.6). The L2 condition requires the SpaCal cluster to be at a distance in the transverse plane of more than approximately 30 cm from the beam pipe.

¹the duration of the HERA fill is generally up to 8 hours

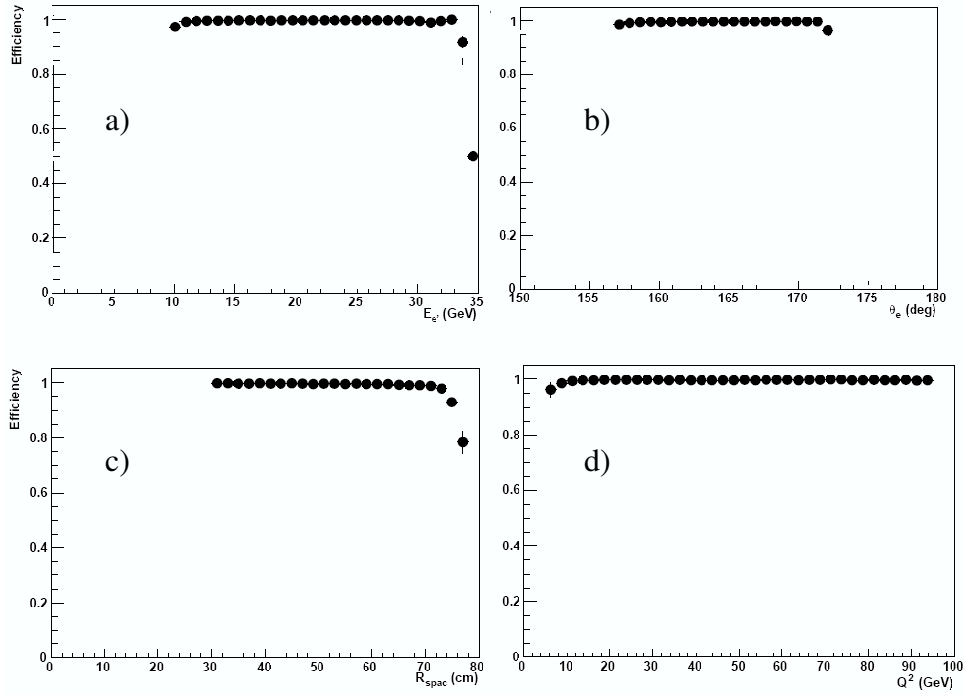


Figure 4.16: Efficiency of the $S03$ subtrigger as a function of the energy of the scattered electron (a), its polar angle (b), transverse distance of the electron cluster from the beam pipe (c) and the photon virtuality (d).

The efficiency of the IET element of the $S03$ subtrigger is shown in Fig. 4.16 for different variables related to the scattered electron. The additional time-of-flight and veto conditions, $T_{\text{OF\&VETO}}$, designed to reject non- ep background, are assumed to be 100% efficient. The subtrigger $S03$ is therefore estimated to be fully efficient in the range of the scattered electron energy $E_{e'} > 10$ GeV.

During the selected running periods, the $S03$ subtrigger was not downscaled. The average prescale at the trigger level 1 is therefore $\mathcal{P}_{03} = 1.0$. Because of the relatively high Q^2 , already reconstructed at the trigger level 4, the weight at this level is equal to 1 as well.

Scattered Electron Identification

The scattered electron deposits its energy in the electromagnetic part of the SpaCal and it may leave a track if it is in the acceptance of the central tracker. In order to correctly reconstruct the electron four momentum, its shower must be fully contained in SpaCal. This is achieved by imposing a cut on the polar angle of the electron candidate,

$$\theta_{e'} > 156^\circ. \quad (4.16)$$

The electron misidentification from hadrons, which in general create larger showers that start in the electromagnetic section of the calorimeter, is effectively suppressed by the requirement that the electron cluster radius be less than 4 cm and that the energy of the hadronic part of the calorimeter in the cone behind the cluster to be less than 0.2 GeV. Additionally, the requirement

on the cluster energy,

$$E_{e'} > 10 \text{ GeV}, \quad (4.17)$$

results into a high trigger efficiency. Because of the subtrigger restriction at trigger level 2, a cut on the distance of the electron candidate cluster from the beam pipe is present, $R_{spac} > 30 \text{ cm}$.

Diffraction Selection

The diffractive sample is required to have a large gap between the direction of the outgoing proton and the forward edge of the X system. The value of the η_{max} variable, which represents the pseudorapidity of the most forward cluster above noise threshold of 400 MeV in the LAr calorimeter, is required to be

$$\eta_{max} < 2.5. \quad (4.18)$$

Smaller η_{max} values restrict the X system, such that it is more likely to be fully detected by the LAr calorimeter. This cut reduces the amount of the non-diffractive DIS background, and also reduces the bias for the reconstructed $x_{\mathbb{P}}$ variable, as mentioned in section 4.3.1. To reduce further the contribution from proton dissociative events, FMD layers are required to be clean of hits above the noise level. The requirement is as follows:

- less than 2 hits in the first two layers, and
- less than 3 hits in the first three layers.

Basic Background Rejection

To reduce the background from beam-gas interactions, the z coordinate of the reconstructed event vertex must lie close to the nominal interaction point,

$$|z_{vtx}| < 35 \text{ cm}. \quad (4.19)$$

To reduce the background due to photoproduction, a cut

$$\sum_{X,e} (E - p_z) > 35 \text{ GeV} \quad (4.20)$$

is introduced, where the sum runs over the scattered electron candidate and the reconstructed hadrons from the X system.

Other Cuts

Because the diffractive production of vector mesons has not been simulated, the mass of the reconstructed X system is required to be $M_X > 3.5 \text{ GeV}$.

4.3.3 Subsample of Events With Proton Tagged by the VFPS

A subsample of diffractive events tagged by the VFPS is selected from the reference sample, asking for both VFPS trigger elements in coincidence.

Electron Candidate	$E_{e'} > 10 \text{ GeV}$ $\theta_{e'} > 156^\circ$ cluster radius $< 4 \text{ cm}$ HAD energy behind cluster $< 0.2 \text{ GeV}$ $R_{spac} > 30 \text{ cm}$
Diffractive Selection	$\eta_{max} < 2.5$ FMD hits in layer 1+2 < 2 FMD hits in layer 1+2+3 < 3 $M_X > 3.5 \text{ GeV}$
Background Rejection	$\sum_{X,e} (E - p_z) > 35 \text{ GeV}$ $ z_{vtx} < 35 \text{ cm}$
Subtrigger	$S03$

Table 4.3: Summary of cuts applied to select inclusive diffraction by the LRG method.

Cuts	Remaining Events
VFPS triggered, electron in SpaCal	869,162
$\sum (E - p_z) > 35 \text{ GeV}$	817,112
$ z_{vtx} < 35 \text{ cm}$	769,435
$\eta_{max} < 2.5$	222,025
clean FMD layers	194,947
$S03$ subtrigger, $R_{spac} > 30 \text{ cm}$	25,053
$M_X > 3.5 \text{ GeV}$	20,134

Table 4.4: Rejection power of the selection cuts w.r.t. VFPS tagged events. Each cut is applied in addition to the previous cuts.

Selection Summary

The list of all cuts for the LRG sample is summarised in Tab. 4.3. The number of inclusive diffractive event candidates selected by the LRG method in the period of 2006-2007 corresponds to 143,267. The number of events in this sample triggered by the VFPS corresponds to 20,134. Tab. 4.4 shows all cuts and the effect of the cuts. As shown, the total number of VFPS tagged inclusive events in the DIS regime is more than 800,000. After the LRG selection, this number reduces to approximately 20,000. During a fraction of the selected run period, the noise level in FMD was higher compared to the rest of 2006/2007. Therefore, the requirement of clean FMD layers rejects VFPS tagged events in these FMD noisy periods.

4.3.4 Simulation of Signal And Background Processes

The elastic diffraction as well as the background contributions are generated by the RAPGAP event generator (described in section 2.4.1). The generated processes are (see also Fig. 4.17):

- diffractive DIS scattering with pomeron exchange in the elastic and the proton dissociative regimes;

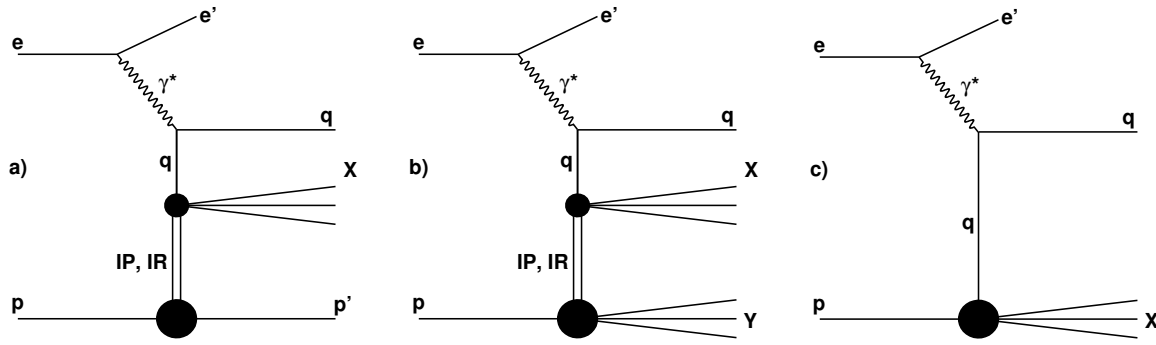


Figure 4.17: Processes generated by the RAPGAP Monte Carlo. The pomeron and the reggeon exchange in elastic (a) and proton dissociative (b) scattering and non-diffractive inclusive deep inelastic scattering (c).

- diffractive DIS scattering with reggeon exchange in the elastic and the proton dissociative regimes;
- non-diffractive deep inelastic scattering.

All the above processes are generated separately, and with initial and final state QED radiation. The incoming electron and the proton energies are set to $E_e = 27.6$ GeV and $E_p = 920$ GeV to match the beam energies in the data for that period. The generated kinematic domain in the photon virtuality, Q^2 , Björken x and the inelasticity, y , is

$$4.5 \leq Q^2 \leq 1000 \text{ GeV}^2 \quad (4.21)$$

$$3 \times 10^{-5} \leq x \leq 1.0 \quad (4.22)$$

$$0.005 \leq y \leq 0.90. \quad (4.23)$$

Simulation of Diffractive Events

The parameterisation of F_2^D is given in terms of the set of diffractive parton distribution functions obtained from the next-to-leading order QCD fit to the H1 data (H12006 B) [44]. The DPDFs in the fit were modelled in terms of a light flavour singlet distribution, consisting of u , d and s quarks and anti-quarks. For the contribution of charm, the boson-gluon fusion process had to be generated separately and needs to be added to the light quark cross section. In order to distinguish between pomeron and reggeon exchange, the two processes were generated separately.

The DPDF set has been extracted from the data sample obtained by the LRG method and contains the contribution from events with mass of the proton dissociative system $M_Y < 1.6$ GeV. However, for the present determination of the VFPS acceptance, it is essential to know the cross section fraction of elastic diffraction. As explained in section 2.2.3, the analysis of elastic diffractive events with the scattered proton measured by the FPS detector ($M_Y = m_p$), showed that the contribution of the proton dissociative diffraction with the $M_Y < 1.6$ GeV to the cross section measured by the LRG method is 23%. The elastic diffractive cross section given in the RAPGAP generator is therefore normalised by the factor of $1/1.23$.

Process	Elastic/ p -diss.	Int. Luminosity (pb ⁻¹)	N° Events	σ (nb)
pomeron exchange (uds)	elastic	227.0	600,000	26.6
pomeron exchange (uds)	p -diss.	101.5	450,000	26.8
pomeron exchange (c)	elastic	243.4	400,000	3.7
pomeron exchange (c)	p -diss.	149.1	50,000	0.7
reggeon exchange	elastic	294.2	300,000	4.5
reggeon exchange	p -diss.	0.8	150,000	178.5
non-diff. DIS	inelastic	137.2	3,000,000	219.6

Table 4.5: The list of generated processes. The cross section values, σ , given by the RAPGAP event generator are indicated.

The value of the effective pomeron intercept in RAPGAP was set to $\alpha_{\mathbb{P}}(0) = 1.11$ and the value of the slope $\alpha'_{\mathbb{P}} = 0.06$ in the linear pomeron trajectory $\alpha_{\mathbb{P}}(t)$. The value of the t slope was set to $B_{\mathbb{P}} = 5.5 \text{ GeV}^{-2}$ in the elastic diffraction and 1.6 GeV^{-2} in the case of proton dissociation. The M_Y distribution of the proton dissociation system is modelled by $1/M_Y^2$. The value of Λ_{QCD} was set to 220 MeV.

The kinematic domain in the $x_{\mathbb{P}}$ and t variables for all generated diffractive processes is

$$x_{\mathbb{P}} < 0.2 \quad (4.24)$$

$$|t| < 5 \text{ GeV}^2 \quad (4.25)$$

and reflects the range of the designed VFPS acceptance, with an extension to account for the smearing.

Simulation of DIS Background

The inclusive DIS cross section is based on the 'H1 2000 LO' [33] parton densities of the proton. In the same generated kinematic domain the cross section amounts to $\sigma \simeq 220 \pm 2 \text{ nb}$ and the generated integrated luminosity corresponds to $\mathcal{L} \simeq 137 \text{ pb}^{-1}$.

The summary of all generated processes with the number of actually produced events is depicted in Tab. 4.5. The produced events may be further weighted by the RAPGAP generator, depending on their kinematic region, with lower Q^2 events having higher weights than events at higher photon virtualities. To compare the simulated distributions with data, those weights will be applied on an event-by-event basis.

Simulation of the Forward H1 Region

The HERA magnets along the proton beam pipe are simulated with constant settings. Those settings are, however, input parameters and thus can be varied for different simulations. Of particular interest are the proton beam CX magnets in the forward H1 region, responsible for a certain beam bump in the region of 220 m, where the VFPS is installed. To simulate a certain beam bump at 220 m, the settings of the two magnets, CX1 at 149 m and CX2 at 200 m from the nominal interaction point, have to be adjusted. For the study presented in this thesis, the CX magnet settings were set to simulate the -6mm beam bump.

	$\langle z_{vtx} \rangle$ [cm]	$\sigma_{z_{vtx}}$ [cm]
Data	0.78 ± 0.04	9.40 ± 0.03
Uncorrected MC	0.59 ± 0.05	10.28 ± 0.03
Corrected MC	0.78 ± 0.04	9.41 ± 0.03

Table 4.6: Parameters of the gaussian fit to the reconstructed z vertex distributions in the data, and the uncorrected and corrected MC. The mean values $\langle z_{vtx} \rangle$ and the widths $\sigma_{z_{vtx}}$ are listed.

The position of the VFPS detector with respect to the center of the beam pipe in the x direction is also steerable. Both VFPS pots are set to the fixed position $x_{VFPS1} = 0.268$ mm and $x_{VFPS2} = 0.235$ mm [38]. Efficiencies of the VFPS trigger tiles (described in section 4.1) have been applied in the simulation.

Monte Carlo Corrections

z Vertex Reweighting The distribution of the z vertex coordinate differs in data and MC. Gaussian fits are applied to the distributions and the MC events are reweighted accordingly. Table 4.6 contains values of the means, $\langle z_{vtx} \rangle$, and the widths, $\sigma_{z_{vtx}}$, for the data, the uncorrected MC and the corrected MC.

SpaCal Cluster z Coordinate Shift The difference in the z position of the SpaCal clusters of the scattered electron candidates between data and MC distributions has been found to be $\Delta z \simeq 1.8$ cm. The MC distribution has been shifted to match that of the data.

4.3.5 Inclusive Diffraction

Distributions for inclusive diffraction selected on the basis of a large rapidity gap ($\eta_{max} < 2.5$) are shown in Fig. 4.18 and Fig. 4.19. The data are compared to the sum of the simulated elastic and proton dissociative diffractive and non-diffractive DIS processes.

The MC contribution from elastic diffraction and that from non-diffractive DIS are normalised to the data luminosity. The pomeron and the reggeon contributions from diffraction with the proton dissociation are first normalised to their luminosities as given by the RAPGAP (see Tab. 4.5). The sum of the proton dissociative events normalised at this stage being N_{pd} , it is then normalised to the number of events obtained after subtraction of the elastic diffractive events, N_{el} , and non-diffractive DIS events, N_{DIS} , from the data, N_{data} . The final normalisation weight for the proton dissociative contribution reads

$$w_{pd} = \frac{N_{data} - N_{el} - N_{DIS}}{N_{pd}}. \quad (4.26)$$

The cross sections in the proton dissociative case are poorly known and their predictions by RAPGAP are not accurate. To try to quantify the effect of this uncertainty, we estimated that if we would take the cross section equal in the elastic and proton dissociative cases (by assigning the value of the elastic cross section to the proton dissociative cross section), it would only affect our acceptance measurement (section 4.3.7) by 2%. This effect is quite small because the cut $\eta_{max} < 2.5$ rejects most of the contribution with reggeon exchange, which dominates

at higher $x_{\mathcal{P}}$ values and because the difference in shape of the $x_{\mathcal{P}}$ distribution between the two simulated processes with the pomeron exchange in the proton dissociation regime (Tab. 4.5) is negligible.

The non-diffractive DIS contributes at the level of $\sim 5\%$ in the region $\eta_{max} < 2.5$. The η_{max} distribution shows the characteristic diffractive plateau. Distributions are in general well described, except β and the polar angle of the X system, γ_h . These problems are mostly due to a mistake in the implementation of the H1 Fit 2006 B DPDFs in the RAPGAP MC, which has been reported only recently [48]. The kinematic peak around 27 GeV in the energy distribution of the scattered electron, $E_{e'}$, is suppressed due to the η_{max} cut: by selecting the X system spread approximately in the central region of the H1 detector, we select events where the longitudinal momentum of the incoming parton from the proton is compensated by the longitudinal momentum of the incoming virtual photon, leaving the scattered electron with smaller energy.

4.3.6 Inclusive Diffraction With VFPS Tagged Protons

Distributions for the elastic diffraction tagged by the VFPS are shown in Fig. 4.20 and Fig. 4.21 for the HERA period with the proton beam bump of 6 mm at 220 m, and they are compared to MC prediction of the elastic diffraction. The integrated luminosity of the corresponding sample is 24 pb^{-1} . The MC contribution is normalised to the data luminosity. As can be seen, the simulation of the VFPS slightly overshoots the data in terms of the normalisation, but the shapes of the distributions are generally well described. The difference in normalisation is mostly due to VFPS acceptance simulated in the Monte Carlo. The excess of events at low $x_{\mathcal{P}}$ in the data is due to the simulated VFPS position being too far from the proton beam for a fraction of the integrated luminosity. On the other hand, the agreement in the high $x_{\mathcal{P}}$ region shows a good understanding of the proton beam optics.

4.3.7 VFPS Acceptance in $x_{\mathcal{P}}$

The acceptance, A , of the VFPS is defined as the ratio of events tagged by the VFPS, to events selected by the large rapidity gap method (N_{LRG}) corrected for the contributions from diffractive proton dissociation (N_{PD}) and non-diffractive DIS (N_{DIS}),

$$A = \frac{N_{VFPS}}{N_{LRG} - N_{PD} - N_{DIS}}. \quad (4.27)$$

The acceptance is measured in bins of $x_{\mathcal{P}}$, which is reconstructed by the central H1 detector according to equation (4.13). The background contribution is shown in Fig. 4.22, right, and in overall amounts to 30% of the total large rapidity gap events (N_{LRG}). The acceptance measured using data (Fig. 4.22, left) shows a maximum of $\sim 75\%$ in the range $0.010 \lesssim x_{\mathcal{P}} \lesssim 0.015$. Because the region $x_{\mathcal{P}} \gtrsim 0.02$ is the tail of the $x_{\mathcal{P}}$ distribution, restricted by the η_{max} cut, the acceptance in this region is not reliable.

The simulated VFPS acceptance presented in the VFPS proposal (see Fig. 4.23, left) shows a relatively wide peak plateau in the region $0.010 \lesssim x_{\mathcal{P},gen} \lesssim 0.025$, whereas the measured acceptance (as a function of the reconstructed $x_{\mathcal{P}}$) at the value of $x_{\mathcal{P}} \simeq 0.025$ is significantly lower. One should, however, not compare the two acceptances directly. The main reasons of the differences between the two are:

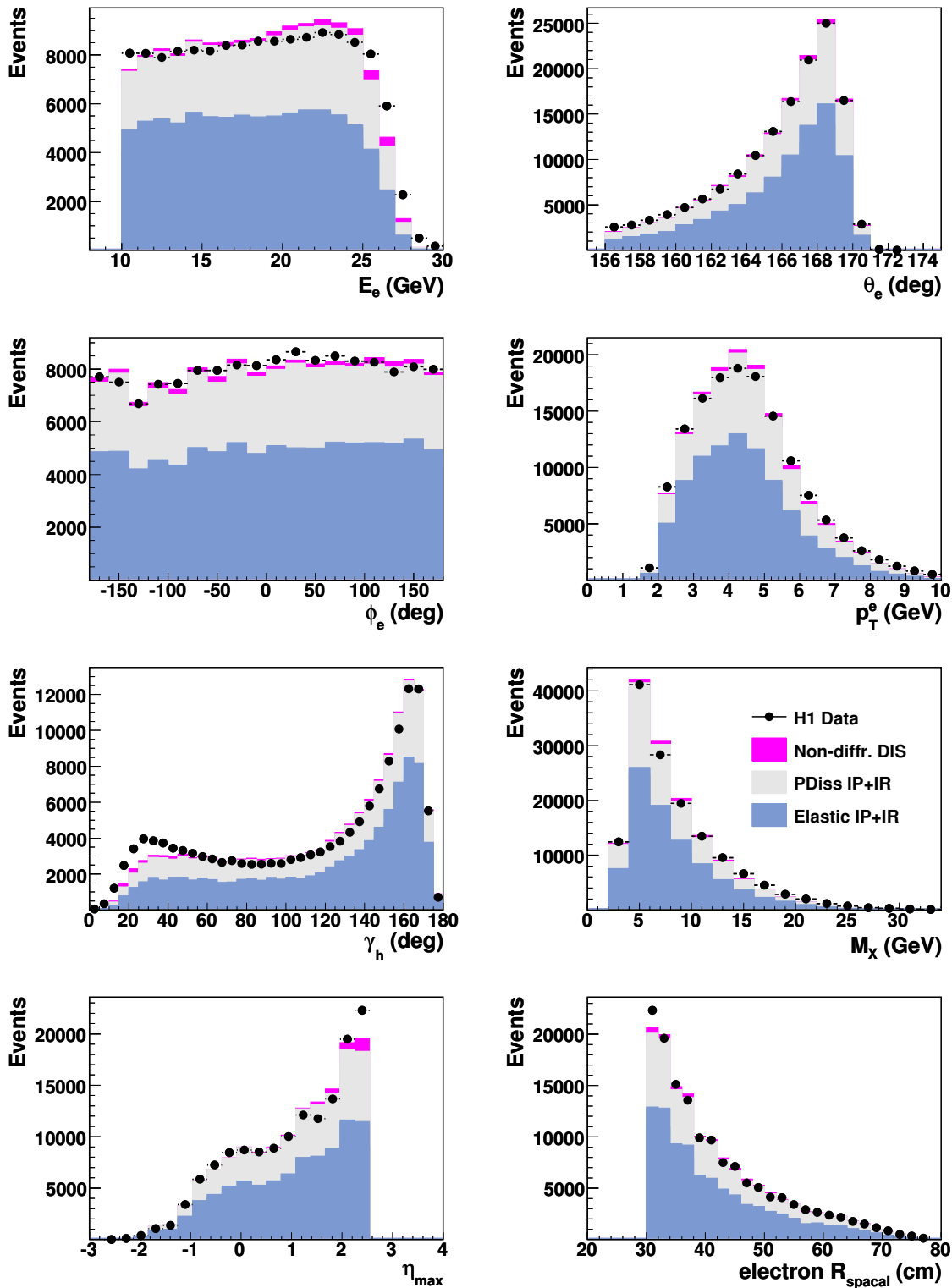


Figure 4.18: Distributions of the inclusive diffractive events, selected on the basis of a large rapidity gap in the event: energy of the scattered electron, E_e , its polar and azimuthal angles, θ_e and ϕ_e , respectively, transverse momentum of the scattered electron, p_T^e , polar angle of the X system, γ_h , and its invariant mass, M_X , limit of the rapidity gap, η_{max} , and distance of the scattered electron cluster from the beam pipe, R_{spacal} .

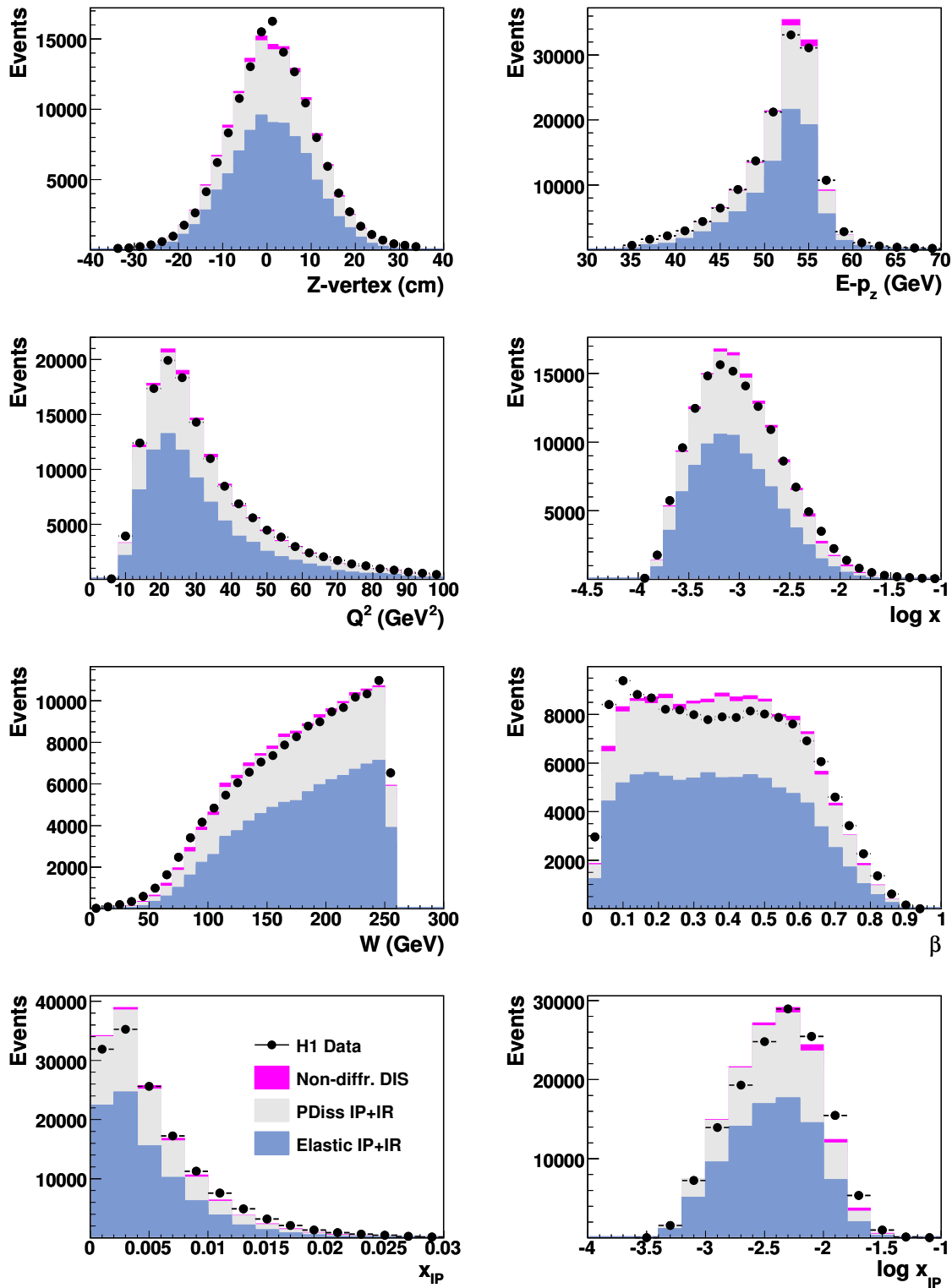


Figure 4.19: Distributions of the inclusive diffractive events, selected on the basis of a large rapidity gap in the event: z coordinate of the event vertex, $\sum_{X,e'}(E - p_z)$, photon virtuality, Q^2 , Björken scaling variable, x , invariant mass of the γp system, W , momentum fraction of the pomeron carried by the struck quark, β , and momentum fraction of the proton carried by the pomeron, x_{IP} .

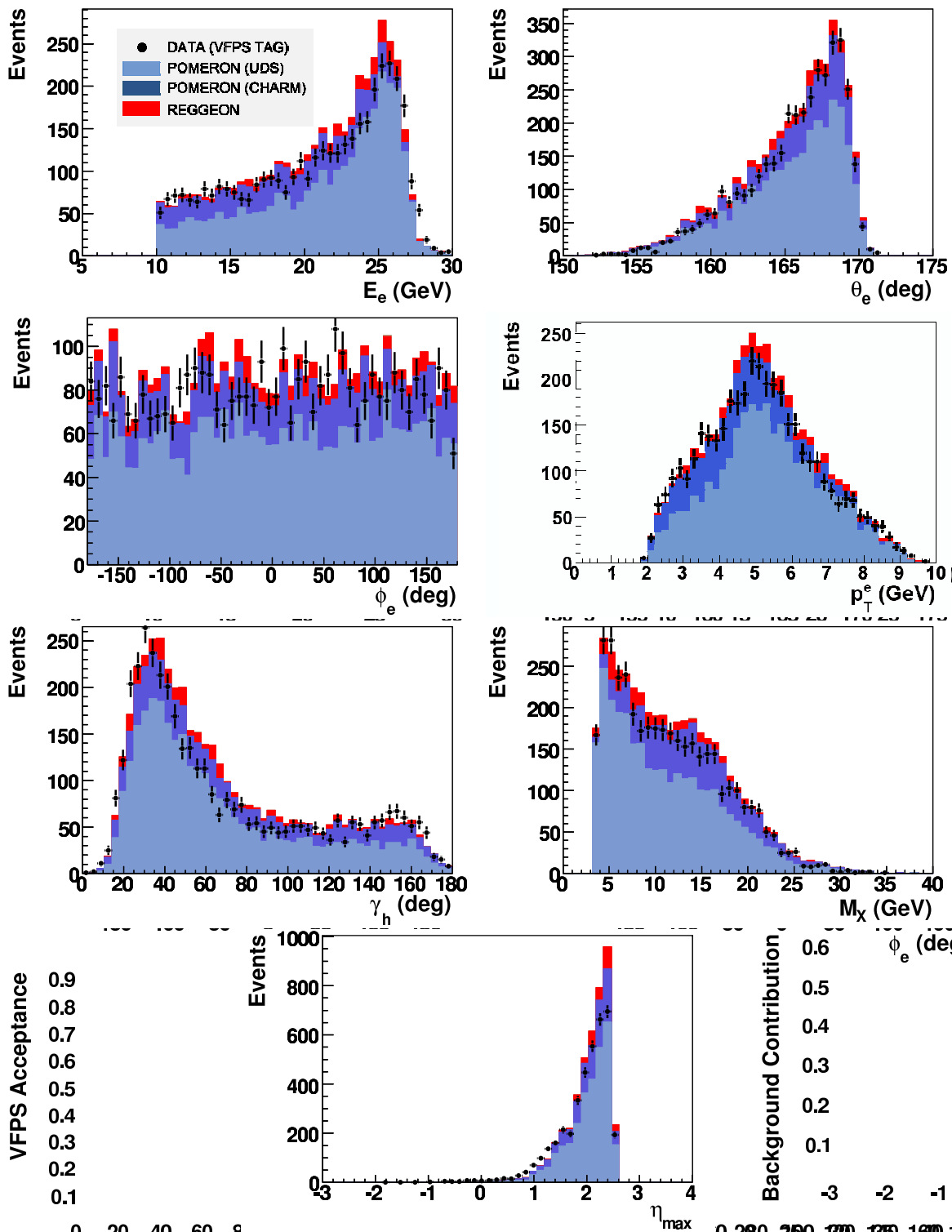


Figure 4.20: Distributions of the inclusive diffractive events tagged by the VFPS detector during the period of the -6 mm bump: energy of the scattered electron, E_e , its polar and azimuthal angles, θ_e and ϕ_e , respectively, transverse momentum of the scattered electron, p_T^e , polar angle of the X system, γ_h , and its invariant mass, M_X , and limit of the rapidity gap of the event, η_{max} .

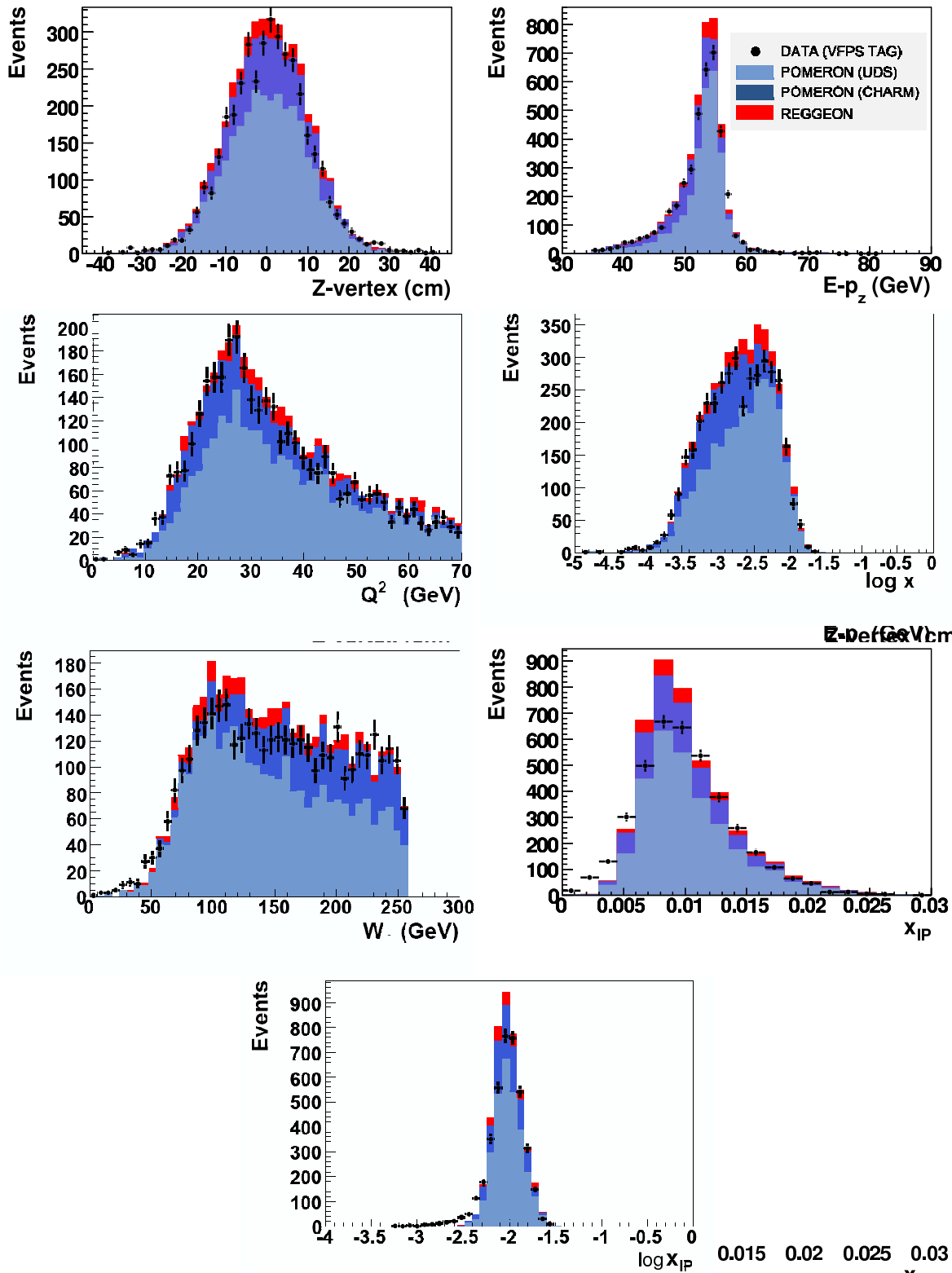


Figure 4.21: Distributions of the inclusive diffractive events tagged by the VFPS detector during the period of the -6 mm bump: z coordinate of the event vertex, $\sum_{X,e'}(E-p_z)$, photon virtuality, Q^2 , Björken scaling variable, x , invariant mass of the γp system, W , and momentum fraction of the proton carried by the pomeron, x_{IP} .

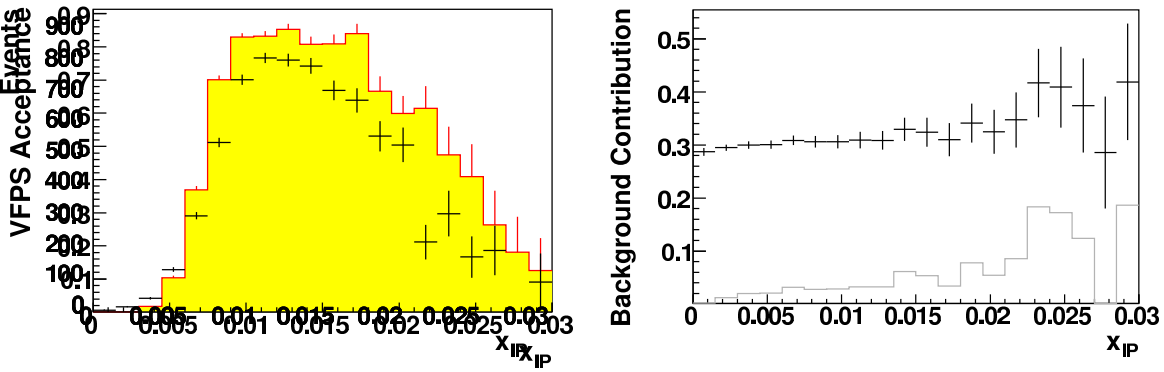


Figure 4.22: left) VFPS acceptance as a function of x_P (points) compared to the simulation (full histogram) for the running period with the proton beam bump of 6 mm; right) the background contribution to the large rapidity gap selection of elastic diffractive events: inclusive DIS (grey line histogram) and proton dissociation in diffraction. The sum of the two contributions is plotted as points.

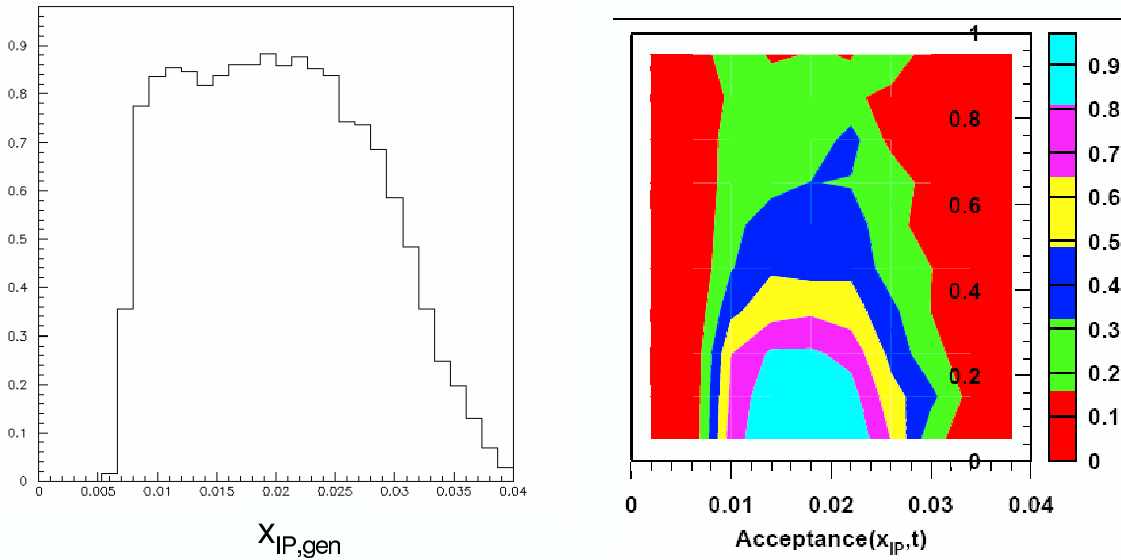


Figure 4.23: left) the VFPS acceptance in x_P and right) in x_P and $|t|$ for $0 < x_P < 0.04$ and $0 < |t| < 1 \text{ GeV}^2$, as in the VFPS proposal document [24].

- The acceptance computed in the proposal used a MC containing only the forward beam optic simulation, i.e. is presented as a function of the true (generated) proton relative energy loss, $x_{\mathbb{P},gen}$. In the measured acceptance shown in Fig. 4.22, the reconstructed value of $x_{\mathbb{P}}$ from the hadronic activity in the main H1 detector has a certain resolution and a significant bias, as discussed in section 4.3.1. The effect of the positive bias alone (neglecting the resolution effects), increasing with $x_{\mathbb{P}}$ from 20% to 30% for $x_{\mathbb{P},gen} = 0.010$ and 0.025 , makes an accumulation of events around $x_{\mathbb{P}} \simeq 0.010$ and thus shrinks the acceptance plateau.
- The acceptance in the low $x_{\mathbb{P}}$ region is sensitive to pot positions w.r.t. the proton beam. The VFPS pots in the simulation presented in the proposal have been set to a fixed position that is slightly too optimistic, compared to real beam conditions, where the high interaction rate in either of the pots often restricts the further movement of that pot.
- The fast simulation used in the proposal approximates the beam pipe as a cylinder of constant shape and the beam transport calculation has been used in the linear approximation.

Fig. 4.23, right, shows the simulated acceptance as a function of the generated $x_{\mathbb{P}}$ and $|t|$. In the absence of t reconstruction with the VFPS, the acceptance has to be integrated over t . In the simulation a plateau of $\sim 95\%$ in $x_{\mathbb{P},gen}$ is seen for $|t| \lesssim 0.3 \text{ GeV}^2$. The measured t -integrated acceptance in Fig. 4.22 is therefore lower than 95% and its MC estimation depends on the t slope put into the simulation.

4.3.8 Prospects

To improve the acceptance description in MC over the full period of 2006-2007, it is necessary to incorporate realistic VFPS pot positions into the MC simulation, as the position affects the VFPS acceptance in the low $x_{\mathbb{P}}$ region. Our recent studies show that one possibility to better simulate the pot position is by artificially moving the pots closer to the center of the beam pipe and remove a fraction of the local tracks in each pot depending on its distance to the beam to fine tune the position for each period (i.e. a lumifill). The description of the high $x_{\mathbb{P}}$ region ($x_{\mathbb{P}} \gtrsim 0.02$) can be improved by the simulation of samples with different settings of correction (CX) magnets, such that the full evolution of the BPM220X position with time is matched (see Fig. 4.6, left).

The overall description of the inclusive diffractive events presented in this chapter is good, but several issues need to be solved. In particular, the correct implementation of the DPDFs in RAPGAP needs to be done.

The next step would be to measure the diffractive structure function $F_2^{D(3)}$ using events with the scattered proton tagged by the VFPS. Events for this measurement will be triggered by the S115 subtrigger, defined as

```
S115 L1: (SPCLe_IET>1 || SPCLe_IET_Cen>2) && (VFPS1 || VFPS2)
        && ToF&VETO
L2: -
```

without directly asking for the presence of the rapidity gap in the event (see Fig. 4.12, right). This would allow us to relax the $R_{spac} > 30 \text{ cm}$ cut to use the full SpaCal acceptance and analyse the full VFPS yield of more than 900,000 events. Later on, when the reconstruction of

the x_P and t using VFPS tracks will be finalised, the differential $F_2^{D(4)}(Q^2, \beta, x_P, t)$ should be measured.

Chapter 5

Diffractive Scattering of Photons Off Protons at Large Momentum Transfer

This chapter presents the study of an exclusive diffractive process: the diffractive scattering of quasi-real photons off protons at large momentum transfer

$$\gamma p \rightarrow \gamma Y, \quad (5.1)$$

where Y represents a hadronic system emanating from the proton dissociation. The study is restricted to values of the momentum transfer $t = (p - p_Y)^2$ such that $|t| > 4 \text{ GeV}^2$, providing the hard scale needed for the pQCD predictions ($|t| \gg \Lambda_{QCD}^2$).

This process is accessed at HERA through the reaction $ep \rightarrow e\gamma Y$. The present study is limited in virtuality of the exchanged photon $Q^2 < 0.01 \text{ GeV}^2$ by the measurement of the scattered electron in the electron tagger. This detection also limits the range of the γp centre of mass energy W to $175 < W < 247 \text{ GeV}$. The scattered photon is detected in the backward calorimeter SpaCal. The hadronic system Y may be detected partially in the H1 detector by tracks in the forward and central trackers and energy deposits in the LAr calorimeter, most of the activity of the Y system being in the forward part of H1 detector (see events on Fig. 5.1).

In the following, the steps toward cross section measurement are detailed: preselection, event selection, background handling and study of systematic errors. Finally cross sections are compared to pQCD predictions and discussed.

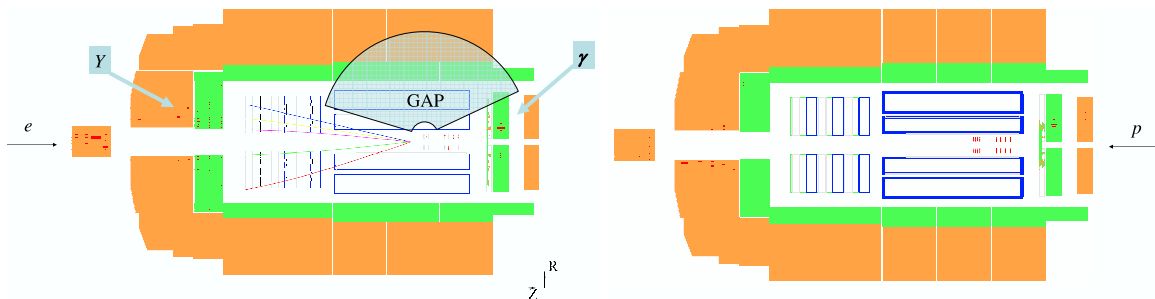


Figure 5.1: Two event candidates for diffractive photon scattering with large momentum transfer as reconstructed in the H1 detector. No energy flow is observed between the edge of the dissociative hadronic system or the edge of the LAr calorimeter and the scattered photon.

5.1 Reconstruction of Kinematic Variables

Different variables describing the kinematics of the process are reconstructed using informations from the scattered photon, electron or final state hadrons.

The inelasticity y is reconstructed using the electron information,

$$y = 1 - \frac{E_{e'}}{E_e} \sin^2 \frac{\theta_{e'}}{2}, \quad (5.2)$$

where $E_{e'}$ is the energy of the scattered electron deposited in the electron tagger and $E_e = 27.6$ GeV is the energy of the electron beam. Since the electron is scattered at very low polar angles, $\sin^2(\theta_{e'}/2) \simeq 1$ ($\theta_{e'} \simeq 180^\circ$, measured with respect to the proton beam direction).

Because the scattering angle of the electron is not measured, Q^2 is not reconstructed. However, as previously stated, the electron tagger limits the photon virtuality range to $Q^2 < 0.01$ GeV². Neglecting Q^2 , the invariant mass of the γp system, W , is reconstructed as

$$W^2 \simeq ys, \quad (5.3)$$

where $s = 4E_e E_p$ is the energy squared of the interaction in the electron proton centre of mass and $E_p = 920$ GeV is the energy of the incoming proton.

The momentum transfer squared at the proton vertex, $|t|$, is approximated as the square of the transverse momentum of the final photon, p_T^γ :

$$|t| \simeq (p_T^\gamma)^2. \quad (5.4)$$

The inelasticity of the γp interaction, $y_{\mathbb{P}}$, is reconstructed using the final state hadronic particles,

$$y_{\mathbb{P}} \simeq \sum_i \frac{(E - p_z)_i}{2E_{\gamma^*}}, \quad (5.5)$$

where $E_{\gamma^*} = E_e - E_{e'}$ is the energy of exchanged photon. The $y_{\mathbb{P}}$ variable can be measured accurately without need of measuring the complete hadronic system, since the forward hadronic activity lost at very low angles does not contribute significantly to the numerator.

The longitudinal momentum fraction of the proton carried by the diffractive exchange, $x_{\mathbb{P}}$, is reconstructed using the energy, E_γ , and longitudinal momentum, p_z^γ , of the scattered photon as

$$x_{\mathbb{P}} = \frac{E_\gamma + p_z^\gamma}{2E_p}. \quad (5.6)$$

5.2 Preselection

Events for this analysis have been detected during years 1999 and 2000. A small period in 2000 with shifted interaction vertex is excluded from the analysis. To preserve the high quality of analysed events, periods where the essential parts of the H1 detector related to the analysis didn't work correctly were not considered. In order to accept a given run, it must fulfill several quality criteria:

- All detectors relevant for the analysis are required to be fully operational and supplied with low and high voltage, and their information for a given run must be properly read out and stored. They are: the CJC detector, the LAr and SpaCal calorimeters, the electron tagger at -33m, the photon detector and the time of flight system.
- Only runs with an integrated luminosity of more than 0.2 nb^{-1} are considered in the analysis to avoid possible bias due to acquisition problems.
- Subtriggers S00 and S50 (see section 5.2.1) are activated in the run, with their prescales, \mathcal{P}_{00} and \mathcal{P}_{50} respectively, set to 10 or less.

The luminosity is determined separately for each run and then summed over all runs which enter the analysis. The total luminosity of the analysed period, corrected for the subtrigger prescales, is 46.2 pb^{-1} . A more detailed description related to the evaluation of the final luminosity is given in section 5.7.

5.2.1 Subtrigger Utilisation

Two topology-based subtriggers, S00 and S50, are used to select, amongst other processes, high p_T photons in diffraction. Their definitions are, separately for trigger levels L1 and L2, the following:

```
S00 L1: SPCLe_IET>2 && ToF&VETO
     L2: -
```

```
S50 L1: (SPCLe_IET>1 || SPCLe_IET_Cen_2) &&
      (LU_ET && !LU_PD_low) && ToF&VETO
     L2: SPCL_R30
```

The trigger element `SPCLe_IET>1` (`SPCLe_IET>2`) triggers on an electromagnetic cluster with energy above 2 (6) GeV in the outer SpaCal. The combination `(LU_ET&&!LU_PD_low)` triggers on an energy deposit in the 33m electron tagger in coincidence with no signal above the low level threshold in the photon detector. The L2 condition of S50 requires the SpaCal cluster transverse distance to be approximately at more than 30 cm from the beam pipe (`SPCL_R30`). This condition overrides the L1 condition triggering in the central region of SpaCal (`SPCLe_IET_Cen_2`). Both subtriggers include time-of-flight and veto conditions, consisting of additional timing requirements designed to reject non- ep background, and are assumed to be 100% efficient. The trigger Level 3 is transparent, but after the basic offline reconstruction at Level 4, the event can be downscaled according to the reconstructed Q^2 value. As the trigger software does not differentiate between electrons and photons, it gives a false reconstruction of Q^2 based on the photon in SpaCal and hence may downscale the event, giving it an additional L4 weight (see Fig. 5.2 left).

The usage of the S00 subtrigger enhances the event acceptance in the SpaCal region close to the beam pipe, which would otherwise lack statistics since the S50 L2 condition does not allow to trigger for particles which are close to the beam pipe. The transverse distance of the photon candidate cluster to the beam pipe for events after final selection (Tab. 5.1) is shown in Fig. 5.2, for the full sample (triggered by S00 or S50) and for the sample triggered only by the S00 subtrigger.

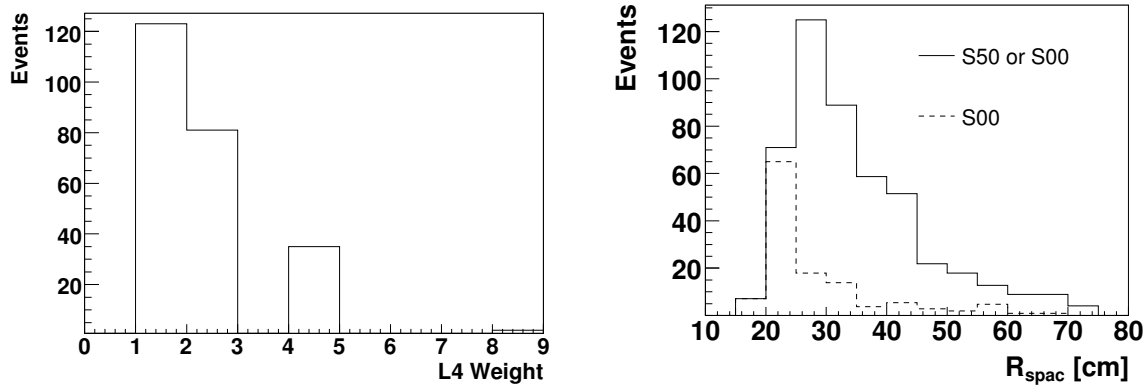


Figure 5.2: Final selection of events: left) distribution of L4 weights; right) distribution of the transverse distance of the SpaCal cluster from the beam pipe (solid histogram). Dashed histogram shows events triggered only by the S00 subtrigger.

Using two or more subtriggers requires the development of an effective logic and applying the correct event weighting scheme. For this analysis the main subtrigger was chosen to be S50, as it has lower average trigger prescale than S00 over the analysed period and can be supplemented by S00 in case of S50 inefficiency (SpaCal region closer to the beam pipe). Therefore, the event triggering scheme illustrated in Fig. 5.3 is as follows:

- 1) For each event we first look at the S50 subtrigger, validated at trigger Level 4 (left branch of Fig. 5.3).
 - a) If positive, the event i is kept with the L4 weight, w_{L4}^i . The corresponding S50 prescale factor is already incorporated in the final value of the integrated luminosity.
 - b) If S50 did not respond positively, the reason why the S50 was not validated is examined. Two reasons may happen:
 - i) Prescale factor¹ above 1. Since S50 prescale is already factored in the measurement, the high prescale event is rejected.
 - ii) Inefficiency². The status of the L4 validation of the S00 subtrigger is examined. If it is validated, event i is kept with weight equal to the ratio of the average prescales over the selected period of runs, $\langle \mathcal{P}_{00} \rangle / \langle \mathcal{P}_{50} \rangle = 2.96/1.55$, multiplied by w_{L4}^i . Otherwise the event is rejected and no further conditions are examined.
- 2) However, the definition of any subtrigger could vary between different periods. The definition of the S50 subtrigger has changed for a small period ($\sim 4 \text{ pb}^{-1}$) in 1999 from the SpaCal trigger into a VLQ³ trigger and thus could not be used. Instead of rejecting the affected run range, we decided to use only S00 for this period and differentiate the trigger logic even further (see right branch in Fig. 5.3).

¹The high trigger prescale status corresponds to a positive “raw” trigger status and an “actual” status set to zero

²Trigger inefficiency is defined as having “raw” status set to zero

³VLQ stands for a Very Low Q^2 detector, placed beyond the SpaCal very close to beam pipe, accessing the ep cross sections at small Q^2 , in the transition region between photoproduction and deep inelastic scattering

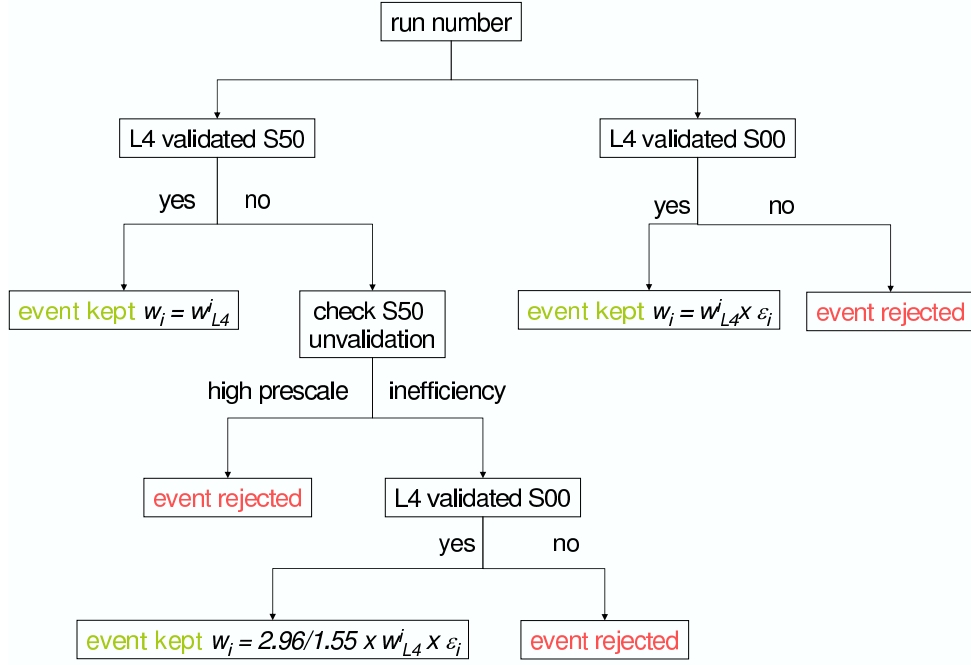


Figure 5.3: Trigger logic applied for the analysis of diffractive scattering of high p_T photons off protons. "Run number" tags periods with two different definitions of the S50 subtrigger, as described in the text. The S00 trigger efficiency, ϵ_i , is in practice set to 1.

Trigger Efficiency

In the logic described above, the data selection is independent of the S50 efficiency and assumes that S0 is 100% efficient. The S00 trigger efficiency, ϵ , is calculated using the sample of events triggered by SpaCal independent ("monitoring") subtriggers, with no trigger element in common with S00. It is evaluated as the fraction of events from the sample, N_{mon} , triggered by S00, $N_{mon\&S0}$,

$$\epsilon = \frac{N_{mon\&S0}}{N_{mon}}. \quad (5.7)$$

As monitor triggers, the LAr triggers S66, S67 and S77 have been used to maximize the statistical gain. The efficiency of the S00 subtrigger is depicted in Fig. 5.4 as a function of SpaCal cluster position in the (x, y) plane, for inclusive events in the selected running period with an electromagnetic cluster from the scattered electron candidate with energy above 8 GeV. The efficiency is uniform, compatible with 1 within statistical error in the region covered by the present analysis after the exclusion of a low efficiency region, in particular around $x \simeq -50$ cm and $y \simeq -25$ cm (for details see section 5.5).

5.3 Event Selection

For events kept by our trigger selection scheme, a set of cuts is applied to identify the final photon and scattered electron, select the particular kinematic domain and minimize contribution from background processes.

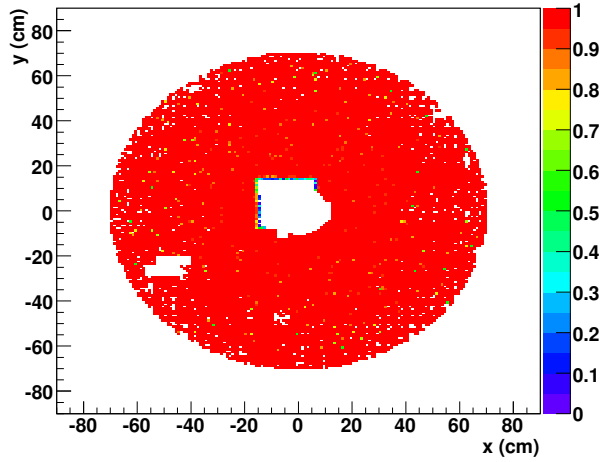


Figure 5.4: Efficiency of the SpaCal elements of the S00 subtrigger as a function of the cluster $[x, y]$ position in the electromagnetic part of calorimeter.

5.3.1 Scattered Electron

The measurement of the scattered electron is provided by the electron tagger at $z = -33$ m. To avoid energy leakage, the electron cluster is required to be well contained in the electron tagger crystals, i.e. the horizontal position of the cluster, x_{tag} , must be within 6.5 cm from the center of the detector.

5.3.2 Final State Photon Identification

In the present analysis, the diffractively scattered photon receives high transverse momentum from the interaction with the proton and is detected in the electromagnetic part of SpaCal. High p_T photon identification is made by the dedicated finder algorithm, finding clusters, isolated in the (η, ϕ) space, in the electromagnetic section of SpaCal. The condition for a small cluster radius (< 4 cm) separates well the electromagnetic shower from that of hadronic origin, since hadronic showers have generally larger transverse spread, resulting into larger cluster radii. The requirement that the sum of all energy deposits in the cone of the hadronic part of SpaCal behind the photon candidate cluster falls below the SpaCal noise threshold (0.2 GeV) reduces a possible misidentification of hadronic particles as well. To disentangle a photon from a charged particle, no track must be associated to the photon candidate cluster⁴.

As we restrict ourself to the kinematic region of $|t| > 4 \text{ GeV}^2$ and t is reconstructed as $|t| = (p_T^\gamma)^2$, the cut

$$p_T^\gamma > 2 \text{ GeV}. \quad (5.8)$$

is applied. In order to correctly reconstruct the four momentum of the photon, its energy cluster must be fully deposited in SpaCal. Therefore, an angular cut is applied to restrict cluster positions to polar angles $\theta_\gamma > 153$ degrees. The high limit $\theta_\gamma \lesssim 175^\circ$ is given by the requirement

⁴The difference between the position of a cluster and the nearest extrapolated track from the tracker region to the SpaCal region is required to be more than 12 cm

of a high transverse momentum of the final state photon. The energy of the photon candidate is required to be more than 8 GeV.

5.3.3 Proton Dissociative System

Due to the large value of $|t|$, the proton breaks up most of the time in the interaction and a hadronic system Y is formed along the axis of the outgoing proton beam. When the transverse momenta of the hadrons are high enough, part of the Y system can be detected in the forward region of the detector. Charged hadrons from the dissociative system may leave tracks in the tracking detectors and thus provide the interaction vertex for the event (shown in Fig. 5.1 left). If the Y system leaves undetected in the beam pipe, only the final state photon is detected in the main H1 detector and the event vertex can not be reconstructed (Fig. 5.1 right). Detected hadrons are reconstructed using combination of tracking and calorimetric information. LAr clusters of energies below 400 MeV, mainly due to electronic noise, are ignored in the reconstruction process of the hadronic system. Similarly for the hadronic part of SpaCal, clusters of energies below 200 MeV are ignored.

According to section 2.3, the studied process is characterised by a large rapidity gap, $\Delta\eta$, between the scattered photon and the struck parton of the proton, i.e. $\Delta\eta = \eta^{min} - \eta_\gamma$, related to the y_P variable by [5]

$$y_P \approx \frac{(p_T^\gamma)^2}{xW^2} \approx e^{-\Delta\eta}. \quad (5.9)$$

At the level of stable particles, the struck parton is approximated by the most backward final state particle of the Y system:

$$\Delta\eta \simeq \eta_Y^{min} - \eta_\gamma. \quad (5.10)$$

5.3.4 Basic Background Rejection

A number of restrictions is applied to minimize the contributions of overlapping events or non ep processes in the final data sample.

Bremsstrahlung

The Bremsstrahlung process (Fig. 5.5) is dominated by $Q^2 \sim 0$ and photon radiation is collinear to the electron beam direction. Such photons can be detected in the photon detector. The electron is also scattered collinearly and due to its energy loss ($E_{e'} = E_e - E_\gamma$) can be detected in the electron tagger for energies between 11 and 19 GeV. In the present analysis, to ensure that the electron in the electron tagger does not originate from a Bremsstrahlung event, a cut on the energy deposit in the photon detector, $E_{PD} < 2$ GeV is applied. This cut is already applied at trigger level for the S50 subtrigger.

Overlapping Events

A DIS event ($ep \rightarrow eX$) with overlapped photoproduction or Bremsstrahlung event may result into the topology of the process of interest, having the scattered electron from DIS in SpaCal and that from the Bremsstrahlung tagged in the 33 m electron tagger (the Bremsstrahlung photon escaping, for some reason, the PD detection). To reduce background from overlapping events,

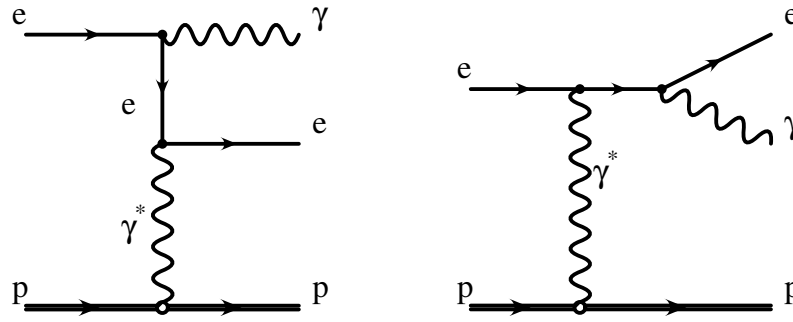


Figure 5.5: The Bremsstrahlung processes with the photon radiated from the incoming or scattered electron.

a cut is imposed on the sum of differences between energy, E , and longitudinal momentum, p_z , of all final state particles in the event, $\sum(E - p_z)$. Derived from the conservation of energy and momentum, this sum should be equal to 55 GeV for a fully (and single) reconstructed event. Because of the resolution of the detectors, the sum is required to be within

$$49 < \sum(E - p_z) < 61 \text{ GeV.} \quad (5.11)$$

This variable is little sensitive to particles lost in forward direction, such as the proton or part of its dissociated system. The full $\sum(E - p_z)$ spectrum is shown in Fig. 5.6. The right broad peak represents contributions from overlapping events, not fully reconstructed.

Beam-Gas Background

Possible beam-gas background can be reduced by asking that the interaction takes place in the region close to the nominal interaction point. A measure of this proximity is the z coordinate of the reconstructed event vertex (z_{vtx}). However, in case of diffractive high p_T photon scattering, only the Y system can contain charged particles that could leave tracks in the tracking detectors used for the vertex reconstruction. Because the hadronic system may escape detection in the trackers, we do not require a reconstructed event vertex. Only in cases where this reconstruction is successful ($\sim 76\%$ of the events, see Fig. 5.16), the z coordinate must lie within 35 cm from the nominal interaction point, $|z_{vtx}| < 35 \text{ cm}$.

By default⁵, in the events with no reconstructed vertex ($\sim 24\%$), all particle four momenta are reconstructed assuming that the event vertex lies at the nominal interaction point, that is $(x, y, z) = (0, 0, 0)$. This, in general, may not be the best assumption, as the distribution of vertex positions may vary from run to run. As shown in Fig. 5.7, mean run vertex coordinate distributions show that \bar{z} spreads significantly - within 5 cm from the nominal interaction point. Therefore, instead of assuming the nominal position for the event vertex, the mean run vertex position $(\bar{x}, \bar{y}, \bar{z})$ is chosen and the photon candidate four-momentum is recomputed accordingly before any cut is applied that involves the final state photon.

⁵in the official reconstruction code used by the H1 Collaboration

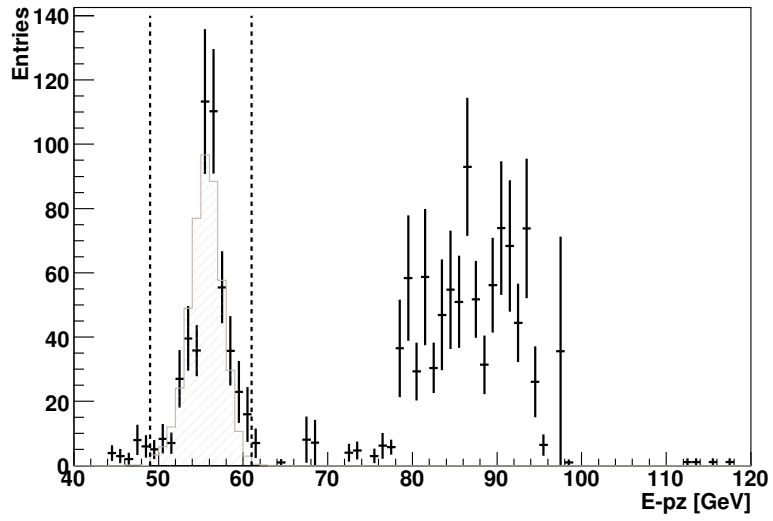


Figure 5.6: $\sum(E - p_z)$ distribution of the full sample (without the cut on $\sum(E - p_z)$) compared to the signal MC simulation. Vertical lines mark the cut boundaries between 49 and 61 GeV.

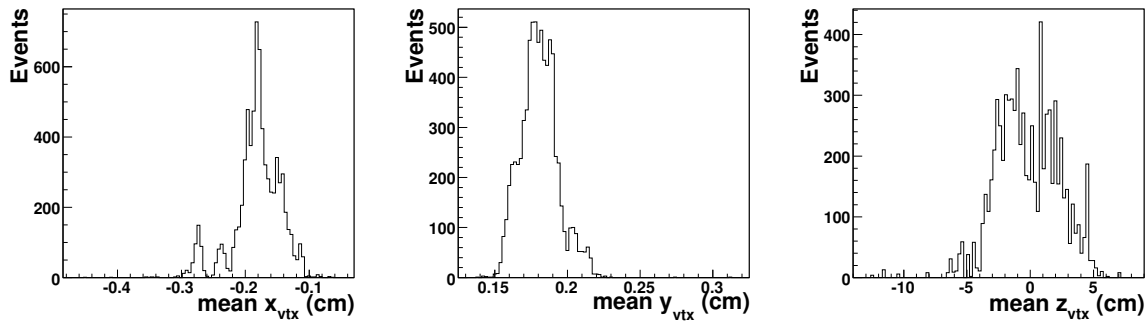


Figure 5.7: Run mean \bar{x} , \bar{y} and \bar{z} coordinates of event vertices in the selected run period.

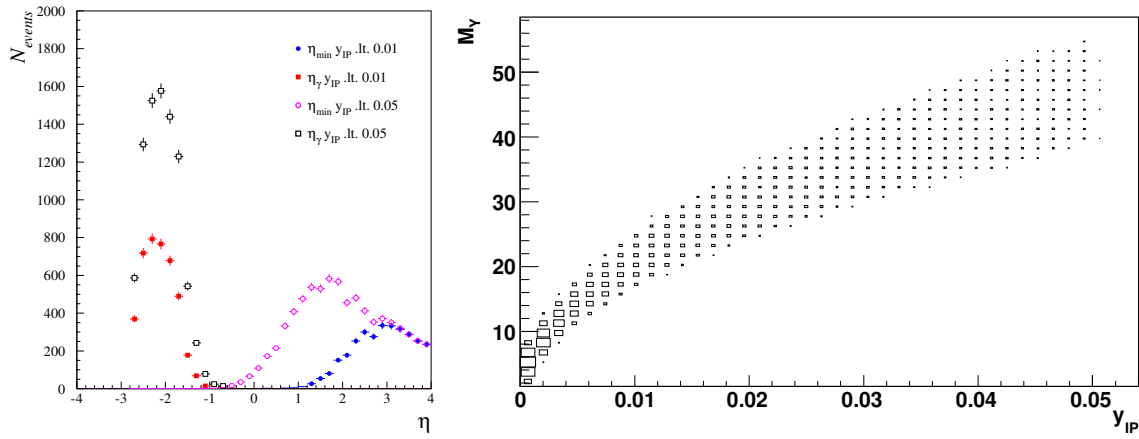


Figure 5.8: Left) Rapidities of the scattered photon and the backward edge of the proton dissociation system for the two different y_{IP} cuts (taken from [5]). Right) M_Y dependence on y_{IP} . The M_Y spectrum depends also on the hadronisation model used in the Monte Carlo simulation.

5.3.5 Kinematic Region

The location of the electron tagger at 33 m from the interaction point determines (through the electron beam optics) its acceptance in the Q^2 and y plane. The use of this detector limits us to analyse events in the domain

$$Q^2 < 0.01 \text{ GeV}^2 \quad (5.12)$$

$$0.3 < y < 0.6, \quad (5.13)$$

to ensure a reasonably high acceptance in y (Fig. 5.12). The y range can be directly translated into the W range $175 < W < 247 \text{ GeV}$.

As stated previously, the $|t|$ domain is limited to

$$4 < |t| < 36 \text{ GeV}^2. \quad (5.14)$$

The y_{IP} domain is set to $y_{IP} < 0.05$, ensuring a low mass, M_Y , for the proton remnant and a large rapidity gap between the photon and the most backward final state particle of the Y system (eq. (5.9)). In the frame of the BFKL predictions the relation between M_Y and y_{IP} and the effect of varying the y_{IP} limit on the size of rapidity gap is shown in Fig. 5.8.

The summary of all cuts of the selection is listed in Tab. 5.1.

5.4 Monte Carlo Models

Monte Carlo simulations serve several important purposes in the analysis chain - estimation of acceptances and resolutions, control of the contribution of background processes and estimation of systematic errors.

Signal and background processes are generated by Monte Carlo programs using suitable models. The generated samples are used as input for the complete simulation of the main H1

Detector Cuts	
Photon Candidate	$E_\gamma > 8 \text{ GeV}$ $\theta_\gamma > 153^\circ$ $p_T^\gamma > 2 \text{ GeV}$ no track cluster radius $< 4 \text{ cm}$ HAD energy behind cluster $< 0.2 \text{ GeV}$
Electron Candidate	detected in 33 m Electron Tagger $ x_{tag} < 6.5 \text{ cm}$ $175 < W < 247 \text{ GeV}$
Diffraction	$\Delta\eta > 2$
Background Rejection	$49 < \sum(E - p_z) < 61 \text{ GeV}$ $ z_{vtx} < 35 \text{ cm}$ (if exists) $E_{PD} < 2 \text{ GeV}$
Kinematic Domain	
$Q^2 < 0.01 \text{ GeV}^2$ $175 < W < 247 \text{ GeV}$ $4 < t < 36 \text{ GeV}^2$ $y_P < 0.05$	

Table 5.1: Summary of cuts applied to select the diffractive scattering of photon off proton at large $|t|$ and below the chosen kinematic domain.

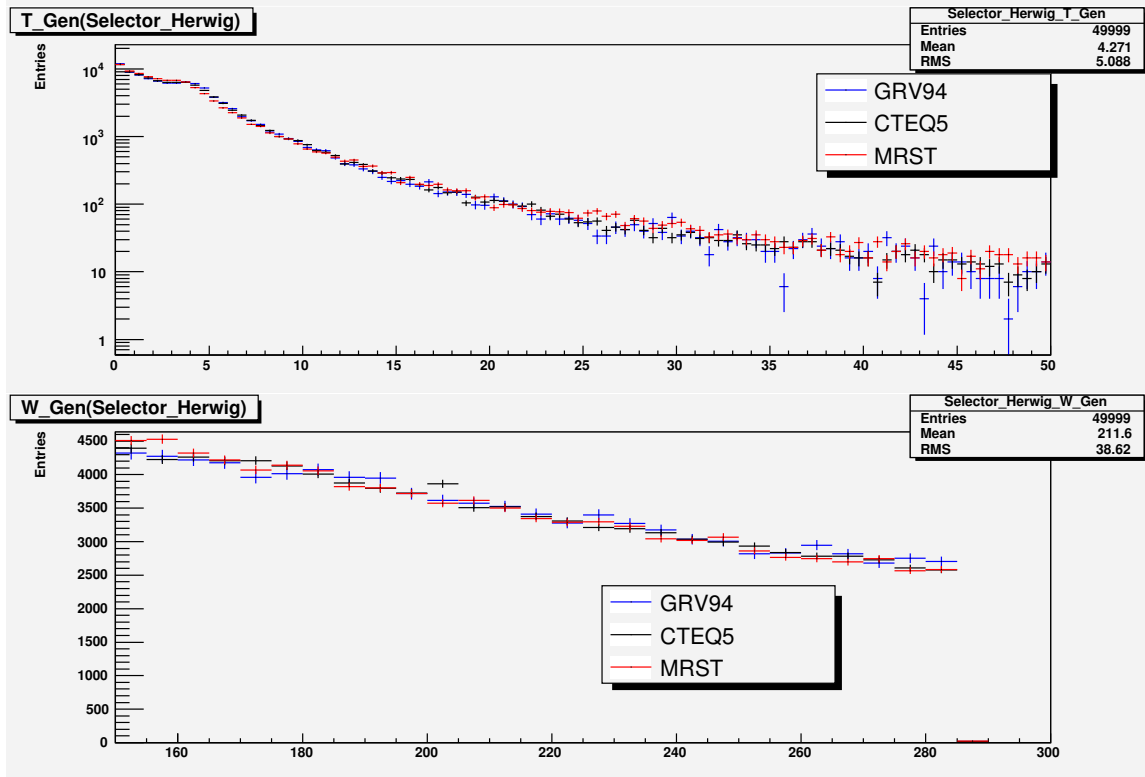


Figure 5.9: Generated $|t|$ distribution in GeV^2 (top) and W distribution in GeV (bottom), shown for three different proton PDF parameterisation, with $p_T^{\min} = 1$. Data are normalised.

detector. The output from this simulations then undergoes the same reconstruction procedure as the real data.

5.4.1 Signal Process

To correct events for detector acceptances and to estimate resolutions in the W and t variables, the HERWIG Monte Carlo program was used (described in section 2.4.2). The choice of $\alpha_s^{BFKL} = 0.17$ is used for the simulation of the signal process.

Events were generated in the kinematic region

$$Q^2 < 0.01 \text{ GeV}^2 \quad (5.15)$$

$$0.25 < y < 0.75 \quad (5.16)$$

and for $p_T^{\min} = 0.25 \text{ GeV}$, which is related to the minimum transverse momentum of the scattered photon. The total number of generated events amounts to 500,000.

For the parameterisation of the parton densities of the proton, the set GRV94 [45] was used; test samples with different parton densities (CTEQ5, MRST) showed no significant differences in distributions. Distributions of the $|t|$ and W variables for the three different parameterisations of the parton distribution functions of the proton are shown in Fig. 5.9.

5.4.2 Background Processes

Other processes can mimic the topology of the observed final state of the diffractive scattering of high p_T photon off proton ($e\gamma Y$), due to the failure of detection of one or more particles. This could lead to an unwanted background contribution to the cross section measurement. Estimation of these processes is made in order to know if they should be considered and, if needed, to subtract them from the data sample.

Inclusive Diffractive Photoproduction

Background events from inclusive diffractive photoproduction, $ep \rightarrow eXY$, are simulated using the PHOJET Monte Carlo generator [6]. The generated sample corresponds to the luminosity of 163 pb^{-1} . The remaining contribution to the selected data mainly comes from photons originating from π^0 decay, faking the high p_T photon candidate in the backward calorimeter, whereas any other hadronic activity from the photon dissociative system X is wrongly associated to the Y hadronic system, falls below SpaCal noise cuts or escapes detection. For the signal process, $ep \rightarrow e\gamma Y$, the rapidity gap is formed between the scattered photon and the most backward final state particle. Therefore, in the inclusive diffractive photoproduction to mimic the topology of the signal process, the rapidity gap has to be formed within the X system. This background is largely reduced by the cut on the presence of a rapidity gap, $\Delta\eta > 2$, that we apply. In the region of $\Delta\eta < 2$ the relative contribution of inclusive processes becomes dominant. This background is estimated to contribute to the cross section at the 3% level.

Lepton Pair Production

The background from the elastic and inelastic lepton pair production $ep \rightarrow ee^+e^-X$ is simulated using the GRAPE generator [7]. This process can fake the signal topology by having one lepton detected in the electron tagger, the second lepton faking the high p_T photon within SpaCal while the remaining lepton escapes detection. The limits on the generated polar angles of all final state leptons and the limits on their energy are shown in Tab. 5.2. The energy region of the lepton that fakes the scattered electron is set to reflect the electron tagger energy acceptance ($0.2 \lesssim y \lesssim 0.6$). A sample corresponding to a luminosity of 1 fb^{-1} has been simulated and passed through the selection criteria of the signal process. Lepton pair production is estimated to contribute 4% of the measured cross section.

final lepton	θ_{min} ($^\circ$)	θ_{max} ($^\circ$)	energy limits [GeV]
faking high p_T photon	150	178	> 7
faking scattered electron	178	180	[10, 22]
escaped detection	0	180	> 1

Table 5.2: Polar angles and energy limits for the three final state leptons of the lepton pair production process.

x range (cm)	y range (cm)	x range (cm)	y range (cm)
-12.5, -8.5	-4.5, 4.5	0.0, 4.5	4.0, 12.0
-12.5, -8.4	-8.5, -4.0	-12.5, -4.0	-12.5, -8.0
-53.0, -40.0	-24.5, -20.0	-16.5, -12.5	-8.5, 0.0
-57.0, -44.0	-29.0, -24.0	-41.6, -36.0	-27.3, -21.4
-8.5, -4.0	-12.5, -8.0	-8.2, -2.7	-45.2, -39.6
8.0, 12.5	-4.5, 4.5	43.2, 48.2	35.6, 40.5
-8.5, -4.0	-8.5, 4.0		

Table 5.3: Fiducial cuts applied to exclude inefficient SpaCal volumes during the 1999/2000 running period.

Diffractive ω^0 production

Diffractive ω^0 production at high $|t|$, with the most probable decay channel $\omega^0 \rightarrow \pi^+\pi^-\pi^0$ (branching ratio 89.1%), and subsequent decay of the π^0 meson into a photon pair, could contribute to the sample by faking the final state photon in SpaCal if both photons form a unique cluster. A study based on the DIFFVM generator [12] shows that this contribution is negligible (at the order of one per mil).

5.5 Monte Carlo Corrections

In order to describe the observed distributions of the data, several corrections to the simulated processes need to be applied. They are discussed in the following.

5.5.1 Detector Level

Event Vertex

Similarly to the vertex correction performed on the data sample, simulated events without reconstructed vertex are corrected by assuming the mean generated event vertex position $(\bar{x}, \bar{y}, \bar{z}) = (-0.19, 0.20, 2.93)$ cm, instead of the position of the nominal interaction point.

SpaCal Inefficient Regions

SpaCal does not have an uniform geometric acceptance. During the 1999/2000 data taking period, certain regions of dead or inefficient cells were excluded from the trigger. These inefficient regions (result of inspections of cluster distributions) are excluded from the analysis by introducing fiducial cuts shown in Tab. 5.3. The same cuts were applied on simulated events to maintain the same geometric acceptance.

SpaCal Cluster Energy Scale

The observed shift between the distributions of the total $\sum(E - p_z)$ for data and for the simulation (Fig. 5.10, left) has been corrected by scaling the simulated cluster energy in SpaCal by +2%. The photon four vectors have been recalculated accordingly. The scaling was applied

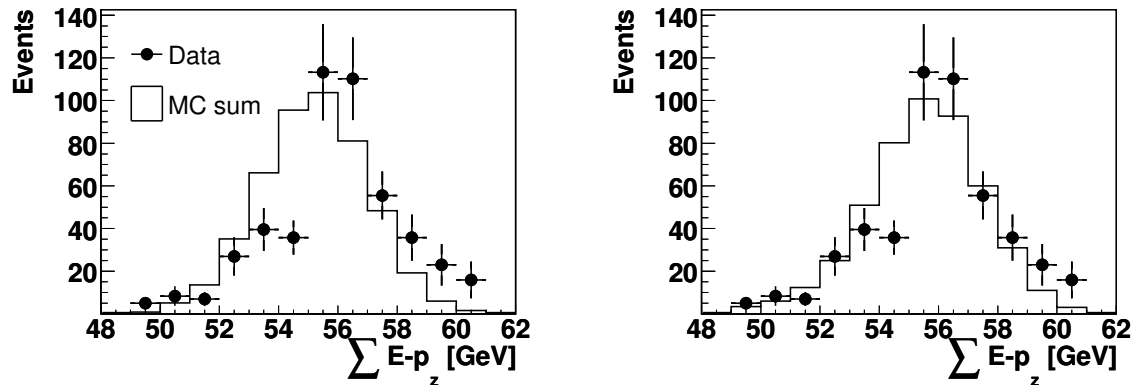


Figure 5.10: $\sum(E-p_z)$ distribution *left*) before and *right*) after the +2% rescale of the simulated photon energy.

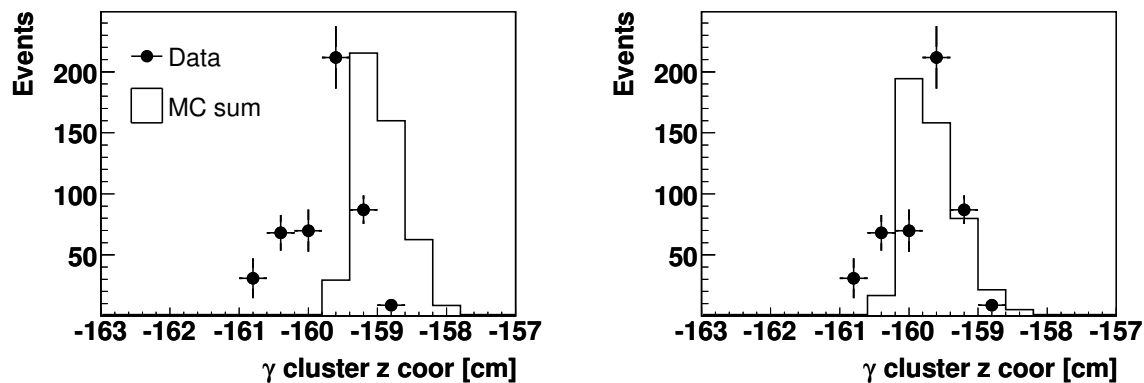


Figure 5.11: Distribution of the photon cluster z coordinate *left*) before and *right*) after the shift applied to simulated events.

before the selection cuts. SpaCal recalibration has been also applied in another H1 analyses (for example see [16]). The result of the energy rescaling on the $\sum(E-p_z)$ distribution is shown in Fig. 5.10, right. The remaining discrepancy at $\sum(E-p_z) \simeq 54$ GeV was studied in details, but remains unclear.

SpaCal Cluster z Coordinate Shift

Positions of simulated photon clusters in SpaCal have been found to be shifted along the z direction by $\Delta z \simeq -0.8$ cm with respect to the data, as can be seen in Fig. 5.11. The different z position of a cluster subsequently affects its x and y coordinates for fixed generated θ and ϕ and eventually results into mismatched SpaCal volume fiducial cuts. Therefore the z coordinate of the cluster has been shifted back by 0.8 cm and the x and y coordinates have been recomputed accordingly. The new cluster position is then subject to SpaCal fiducial cuts.

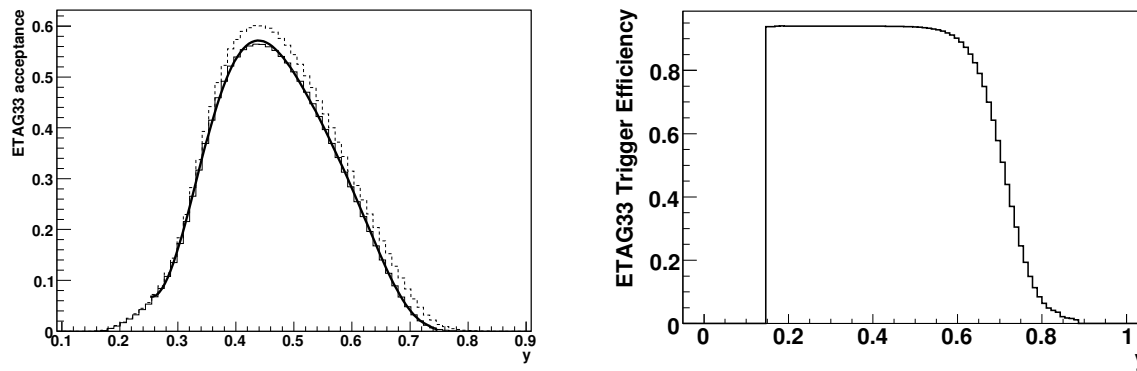


Figure 5.12: left) Electron tagger acceptance as a function of y for the selected run period multiplied by the electron tagger trigger efficiency (solid line histogram) and without trigger efficiency (dashed line histogram). A parameterisation of the acceptance in the form of a polynomial fit (solid curve) is shown as well. Right) Electron tagger trigger efficiency as a function of y .

Scattered Electron Reconstruction

The simulation of the 33m electron tagger is not performed in standard H1 simulation, since its acceptance depends significantly on the electron beam optics and may vary from beam fill to fill. Therefore, the generated energy of the scattered electron, $E_{e'}^{gen}$, has been smeared according to the measured resolution of the tagger, σ_{etag} , (see Fig. 3.10) during the selected running period [35],

$$\sigma_{etag} = 0.17 \cdot \sqrt{E_{e'}^{gen}} + 0.01 \cdot E_{e'}^{gen}, \quad (5.17)$$

for $E_{e'}^{gen}$ in GeV.

The acceptance of the electron tagger as a function of the inelasticity is shown in Fig. 5.12, left, as a dashed line histogram. The efficiency of the electron tagger trigger (separately plotted in Fig. 5.12, right) is also accounted for as a solid line histogram. The effect of acceptance and trigger efficiency is simulated by weighting MC events on the event-by-event basis, using the polynomial fit (solid curve), $A_{etag}(y_{gen})$.

5.5.2 Model Correction

The $|t|$ distribution of the theoretical prediction has been found to be steeper than that observed in the data. The fit of the form of $|t|^{-n}$ gives for the unsmeared distribution $n = 2.60 \pm 0.19$ (stat) $^{+0.03}_{-0.08}$ (syst) (section 5.7.4) and for the generated distribution $n_{MC} = 3.31 \pm 0.02$. In order to correctly evaluate the detector acceptance, the $|t|$ distribution of the simulated events has been multiplied by the ratio of the two fits,

$$R_t(|t|_{gen}) = (|t|_{gen})^{n-n_{MC}} = (|t|_{gen})^{-0.71}, \quad (5.18)$$

where $|t|_{gen}$ is the absolute value of generated momentum transfer squared. The initial $|t|$ distribution as well as the reweighted one are shown in Fig. 5.13.

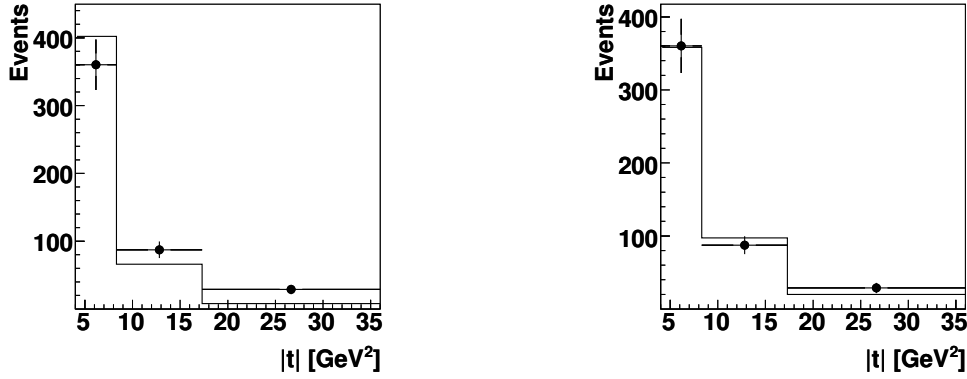


Figure 5.13: $|t|$ distributions *left*) before and *right*) after the reweight of the signal Monte Carlo sample.

To summarize, the total weight, w_i , applied for the given simulated event i consists of the electron tagger acceptance and the reweight of the $|t|$ distribution:

$$w_i = A_{etag}(y_{gen}) \cdot R_t(|t|_{gen}). \quad (5.19)$$

This weight will be incorporated into calculations of the detector acceptances (section 5.7.1).

5.6 Control Plots

Distributions of selected events are compared to predictions for the signal process simulated by HERWIG and for two background processes - inclusive diffraction in photoproduction and production of dileptons. In total, 240 unweighted events have been selected in the analysis, corresponding to 474.3 events after applying the trigger weights, corresponding to an average weight of 1.98. Data are weighted according to the weighting scheme discussed in section 5.2.1 and the statistical error is calculated as the square root of the sum of weight squares in each bin, $\sqrt{\sum_i w_i^2}$. Background processes are normalised to the luminosity of the data sample. Signal Monte Carlo events are first weighted on an event-by-event basis according to equation 5.19, then, due to the free normalisation of the HERWIG prediction (section 5.4.1), distributions are normalised to the number of events obtained after subtraction of the background from the weighted data sample.

In the following figures (Fig. 5.14, 5.15 and 5.16), data are represented by dots with statistical errors, open histograms represent the sum of dilepton production, inclusive diffraction in photoproduction and signal prediction with error bands representing the combined systematic errors added in quadrature (as will be described in section 5.7.2).

High p_T Photon

Distributions related to the scattered photon are shown in Fig. 5.14 and are in general well described by the sum of the signal and background processes. The photon polar angle θ_γ distribution shows a sharp falloff at ~ 173 degrees, related to the requirement of a high transverse

momentum p_T^γ . The p_T^γ distribution is nicely described, but it should be stated that the agreement was achieved after reweighting the t distribution in the signal Monte Carlo sample, as described in section 5.5.2. The background from dileptons production as well as from the inclusive processes is limited to the region of low p_T .

Kinematics

Distributions of the kinematic variables are shown in Fig. 5.15. The good description of the W distribution confirms the correct treatment of the electron tagger in the Monte Carlo, including the acceptance. The reweight applied to the $|t|$ distribution implies the good agreement between data and the reweighted HERWIG $|t|$ distribution. The highest $|t|$ value measured in the sample is 35 GeV². The $x_{\mathcal{P}}$ distribution is reasonably described. The $y_{\mathcal{P}}$ variable depends on the reconstruction of the Y system and shows some excess in the simulation in the region of $y_{\mathcal{P}} \simeq 0$, where almost no particles have been detected in the forward region of calorimeter. However our analysis is only weakly depending on the details of the $y_{\mathcal{P}}$ distribution as the cross section will be integrated over $y_{\mathcal{P}}$ between 0 and 0.05.

Other Variables

Distribution of the scattered electron energy, $E_{e'}$, in Fig. 5.16 shows an agreement with the MC simulation. The rapidity gap distribution between the final photon and the edge of the proton remnant system, $\Delta\eta$, is described and shows the range of gaps that can be measured in the diffractive high p_T photon scattering. Gaps up to 6 units are not uncommon. Distribution of the z vertex coordinate shows only events with a reconstructed vertex. Events where the absent reconstructed vertex is replaced by the run mean vertex are not shown. As can be seen in the mass distribution, M_{cal} of the fraction of the dissociative system Y that is reconstructed in the H1 detector (using the LAr calorimeter and tracking detectors), the visible proton remnant mass is properly modelled. The region of $M_{cal} = 0$ corresponds to events with less than two reconstructed final state particles of the Y system. The reconstruction of the event vertex from the charged particles is described only roughly, with lower efficiency in the simulation (excess of simulated events with event vertex type 0). Improving this agreement by additional correction factor would have only a minor effect on our measurement. Indeed the presence of a reconstructed event vertex only improves slightly the precision of the photon momentum measurement in SpaCal. The effect of the photon polar angle uncertainty will be covered in the study of the systematic errors (section 5.7.2). The $E - p_z$ sum of the event peaks at ~ 55 GeV, with the dilepton background dominating the contribution in the region of low values.

In overall, data are reasonably described and the MC simulation can be used to correct data for the smearing effects of the detector.

Contribution From Region of $R_{spac} < 30$ cm

The present analysis has been extended w.r.t. [14] by including data kept by the S00 trigger. This extended the region of available transverse SpaCal cluster distance from the beam pipe, R_{spac} , which was limited by the L2 condition of the S50 trigger (see section 5.2.1). Of particular interest is the region of low cluster distances providing the majority of low $|t|$ events. As shown on Fig. 5.17, the event gain is significantly enlarged in the low $|t|$ (large W) region, improving the statistical precision of the final measurement.

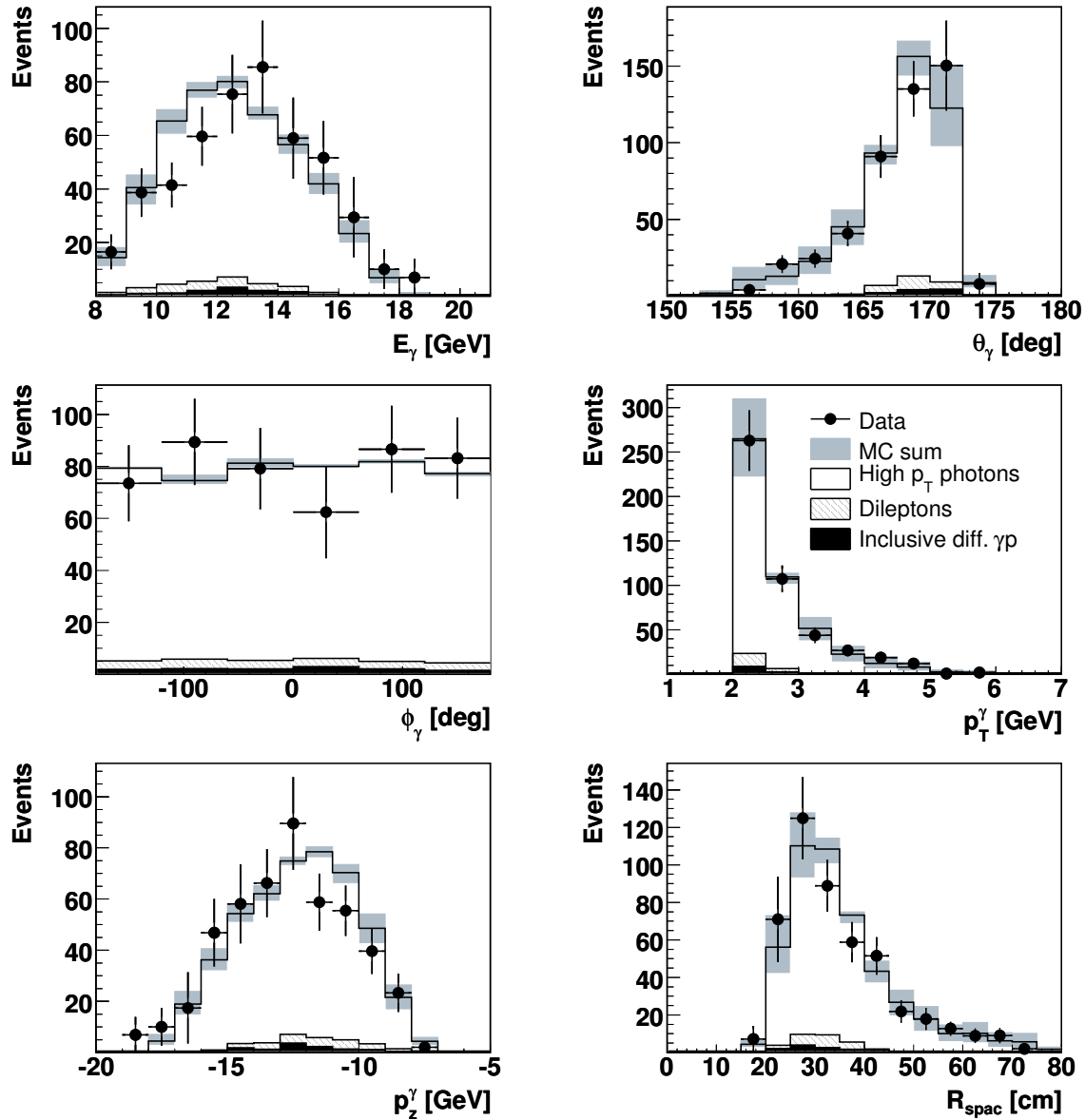


Figure 5.14: Control distributions: photon energy, E_γ , its polar and azimuthal angles, θ_γ and ϕ_γ , respectively, its transverse and longitudinal momenta, and transverse distance of the photon cluster from the center of the beam pipe. Points represent the data with statistical errors and open histograms the sum of signal, dilepton production and inclusive diffraction predictions, with error bands representing the combined systematic errors added in quadrature.

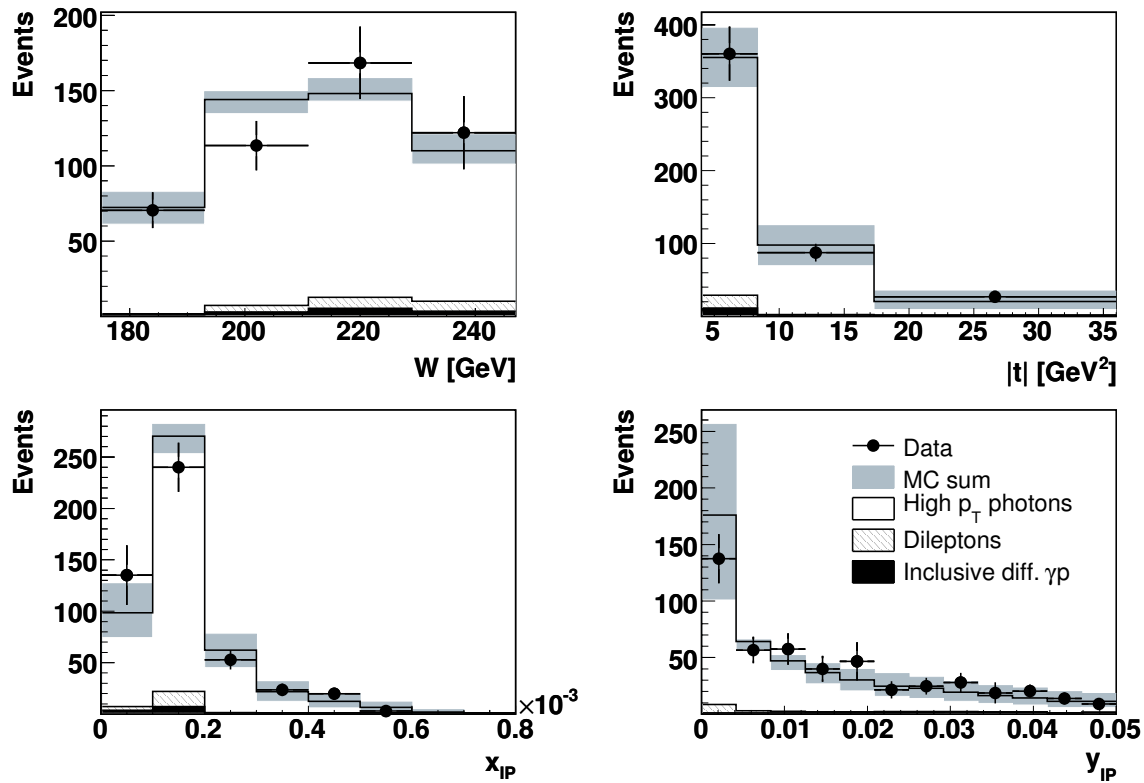


Figure 5.15: Control distributions: invariant mass of γp system, W , momentum transfer squared, $|t|$, x_{IP} and y_{IP} . Points represent the data with statistical errors and open histograms the sum of signal, dilepton production and inclusive diffraction predictions, with error bands representing the combined systematic errors added in quadrature.

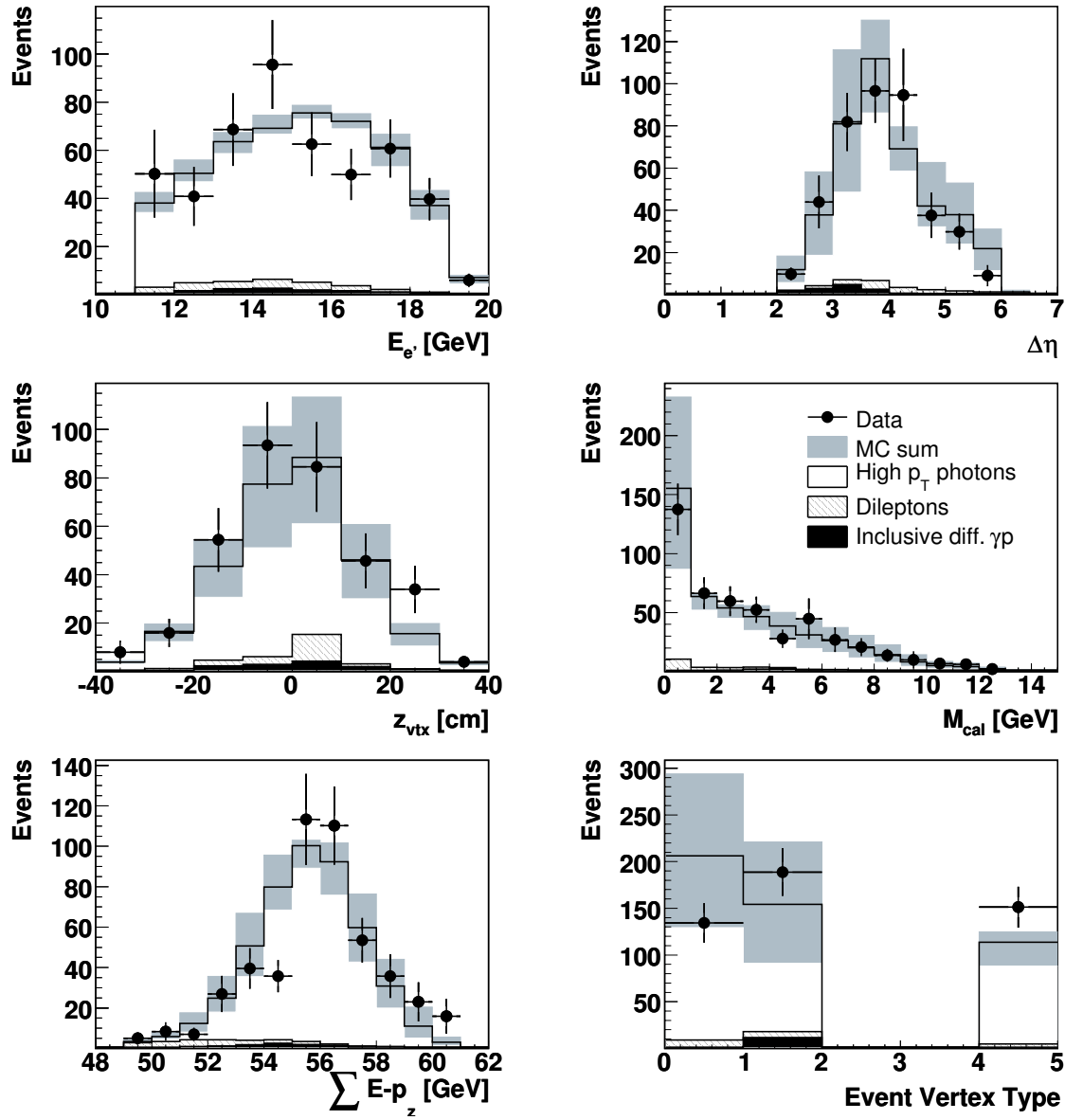


Figure 5.16: Control distributions: energy of the scattered electron, $E_{e'}$, rapidity gap $\Delta\eta$, z coordinate of the event vertex, z_{vtx} , reconstructed fraction of the proton remnant invariant mass, M_{cal} , $\sum E - p_z$ of the event, and type of event vertex: 0 - not reconstructed, 1 - reconstructed by central tracker, 4 - reconstructed by forward tracker. Points represent the data with statistical errors and open histograms the sum of signal, dilepton production and inclusive diffraction predictions, with error bands representing the combined systematic errors added in quadrature.

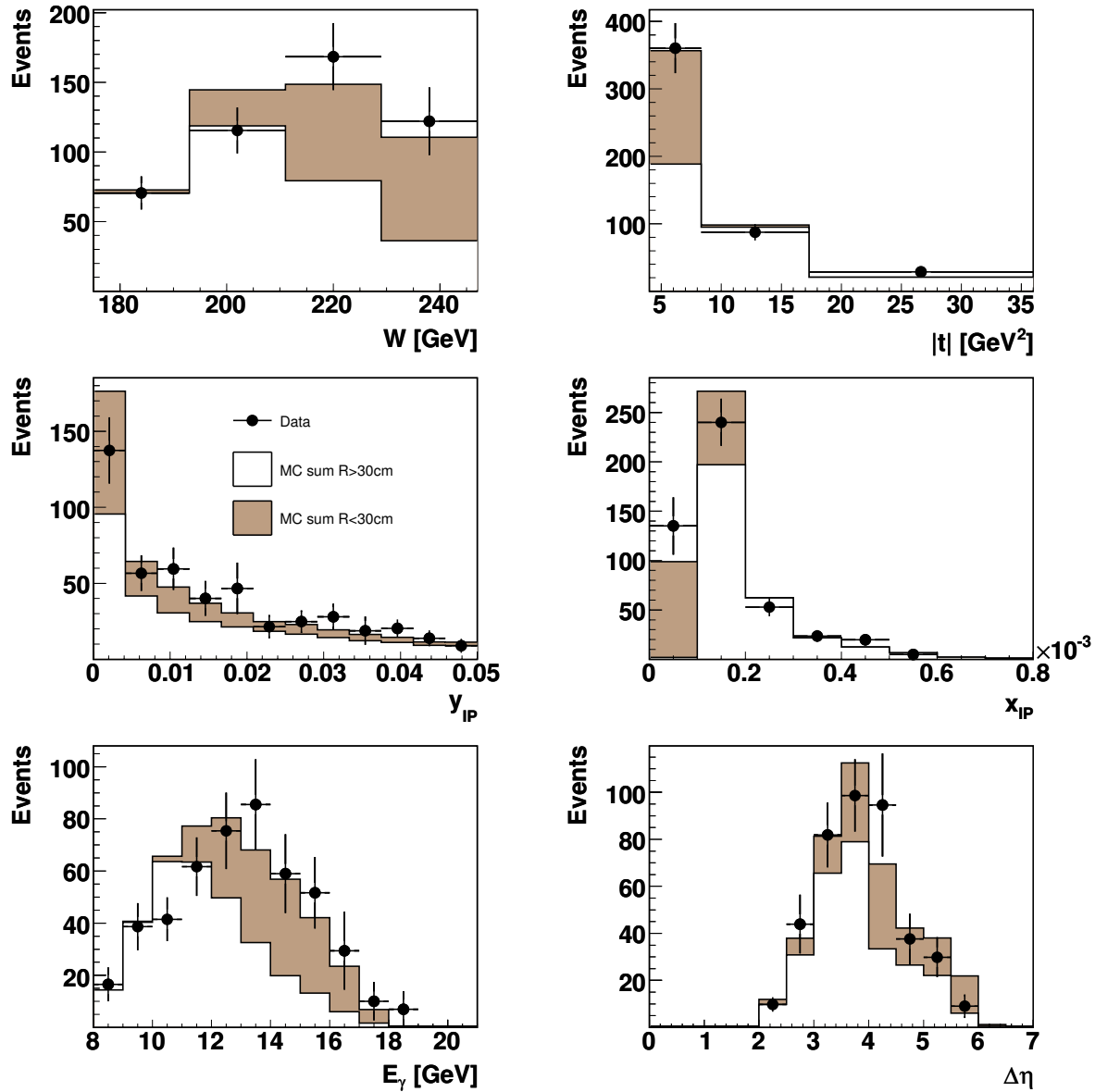


Figure 5.17: Contribution from events with photon candidate cluster at $R_{spac} < 30$ cm to the total distributions. Points represent the data with statistical errors, histograms the sum of signal and background contributions from events below (gray histogram) and above (open histogram) $R_{spac} = 30$ cm.

integrated luminosity	\mathcal{L}_{50}^{35cm}	\mathcal{L}_{50}^{all}	\mathcal{L}_{00}^{35cm}	\mathcal{L}_{00}^{all}	\mathcal{L}
value (pb ⁻¹)	42.37	44.14	3.39	3.57	46.2

Table 5.4: Integrated luminosities corrected for different subtriggers, as explained in the text.

5.7 Cross Sections

In this section, measurements are presented of the γp cross section $\sigma(W)$ as a function of W , and of the differential cross section $d\sigma/dt$, together with the determination of detector acceptances and resolutions and the study of systematic errors.

First the measurement is performed at the electron-proton level and then the γp cross section is extracted using the flux of photons from the electron. The ep cross sections, $\sigma_i[ep \rightarrow e\gamma Y]$, in bin i of width Δ_i are defined as

$$\frac{d\sigma_i[ep \rightarrow e\gamma Y]}{dq} = \frac{N_i^{data} - N_i^{bg}}{\Delta q_i \cdot A_i \cdot \mathcal{L}}, \quad q \equiv t, W \quad (5.20)$$

where N_i^{data} is the number of events in the data sample, with applied weights to correct for the trigger (see section 5.2.1), N_i^{bg} is the sum of the dilepton and inclusive diffractive background events (estimated by MC) in bin i , A_i is the acceptance of bin i and $\mathcal{L} = 46.2 \text{ pb}^{-1}$ is the total integrated luminosity of the data sample.

The total luminosity is corrected for prescales of the corresponding subtriggers including contribution of events originating from satellite bunches. Contribution of satellite bunches is included due to the fact, that only three quarters of events have a reconstructed vertex, $f_v = 0.74$. Thus, the remaining 26% of events may originate from interactions in satellite bunches and this fact is accounted for in the luminosity determination:

$$\mathcal{L} = f_v \cdot \mathcal{L}^{35cm} + (1 - f_v) \cdot \mathcal{L}^{all}, \quad (5.21)$$

where \mathcal{L}^{35cm} (\mathcal{L}^{all}) is the integrated luminosity considering events having vertex within 35 cm (200 cm) from the nominal interaction point. As the analysis is further divided into two periods of different subtrigger treatments (see section 5.2.1), the luminosity is corrected for the appropriate subtrigger prescale in each period:

- In the period that uses S00 and S50, the mean prescale of S50 is included into the luminosity value (\mathcal{L}_{50})
- In the small period using S00 only, the luminosity is corrected for the mean prescale of S00 (\mathcal{L}_{00}).

As a result, the final luminosity value entering the cross section formula reads

$$\mathcal{L} = f_v \cdot (\mathcal{L}_{50}^{35cm} + \mathcal{L}_{00}^{35cm}) + (1 - f_v) \cdot (\mathcal{L}_{50}^{all} + \mathcal{L}_{00}^{all}). \quad (5.22)$$

Values are given separately for each period in Tab. 5.4. However, as the fraction of events without reconstructed vertex is relatively small, the contribution from satellite bunches is small ($\sim 1\%$).

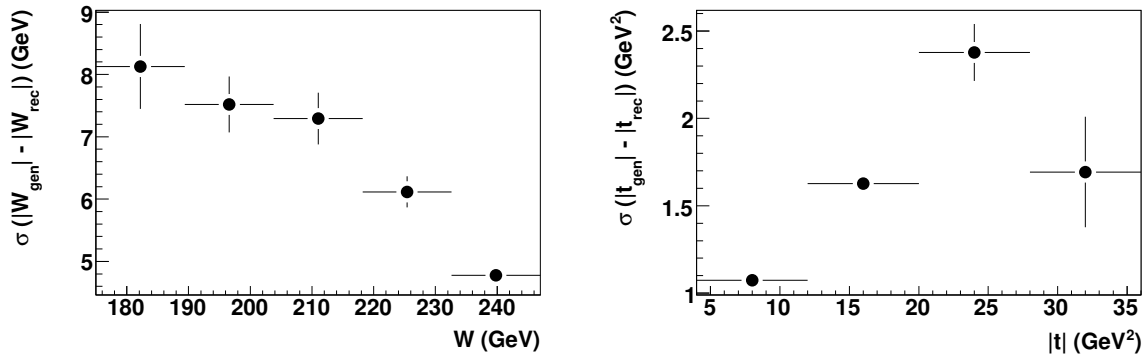


Figure 5.18: Resolutions of W and t as a function of the corresponding variable.

W bin [GeV]	$N^{data} \pm \delta N$	N^{lep}	N^{ip}	N^{bg}
(175, 193)	70.5 ± 11.8	0.8	1.2	1.9
(193, 211)	113.4 ± 16.3	4.4	3.0	7.4
(211, 229)	168.4 ± 24.0	7.2	5.2	12.3
(229, 247)	122.0 ± 24.3	6.4	3.5	9.9

$ t $ bin [GeV ²]	$N^{data} \pm \delta N$	N^{lep}	N^{ip}	N^{bg}
(4.0, 8.3)	360.3 ± 37.1	17.5	11.4	28.9
(8.3, 17.3)	87.3 ± 12.3	1.2	1.1	2.4
(17.3, 36.0)	26.7 ± 6.7	0.0	0.3	0.3

Table 5.5: Corrected numbers of events in the bins in W and $|t|$, together with the background contributions.

Resolutions and Bin Widths

Resolutions, measured as the widths, σ , of the gaussian fit to the $q_{gen} - q_{rec}$ distributions in each bin for the quantity $q = W, t$ are shown in Fig. 5.18. Resolutions range from 2% to 6% in W , whereas the mean resolution in t is around 7%. To avoid large fluctuations originating from the limited resolution, the size of the bins have been chosen large w.r.t. the resolution. In view of the small statistics of the sample (240 events) to enhance the statistics per bin, four bins were chosen in W and three bins in $|t|$, as shown in Tab. 5.5; the bin widths are larger than the resolutions.

Background Subtraction

The estimated number of lepton pairs, N^{lep} , and of inclusive diffractive events in photoproduction, N^{ip} , is subtracted from each bin for the cross section measurement with $N^{bg} = N^{ip} + N^{lep}$. The number of signal and background events in each bin of W and $|t|$ is shown in Tab. 5.5. The given statistical error on data takes into account their respective trigger weights, as $\delta N = \sqrt{\sum_i w_i^2}$. The total background contribution per bin ranges from 3% to 8% in W and from 1% to 8% in $|t|$.

5.7.1 Acceptances

Detector effects such as the geometric acceptance or temporary inefficiencies in the detector response, affect in general the data collection. A correction is made to account for these effects, by determining the acceptance, A_i , for each bin i in W and t . The acceptance is an estimate of the relative loss of statistics at the reconstructed level with respect to statistics in the measured domain one would get if the detector would be ideal. It is estimated by MC and defined as the ratio of the number of events at the reconstructed level, N_i^{rec} , obtained after the full analysis cuts are applied on the simulated quantities, over the total number of generated events N_i^{gen} generated in the domain \mathcal{D} ,

$$A_i = \frac{N_i^{rec}}{N_i^{gen}}, \quad (5.23)$$

where in the present case the domain $\mathcal{D} = \mathcal{D}(Q^2 < 0.01 \text{ GeV}^2, 4 < |t| < 36 \text{ GeV}^2, 175 < W < 247 \text{ GeV}, y_P < 0.05)$. As shown in Fig. 5.19, values of the acceptances in W and t range from 20% to roughly 40% and are largely affected by the inclusion of the electron tagger acceptance and trigger efficiency (shown in Fig. 5.12), which amount to more than 50% of the overall acceptance value.

Even if the description of the detector is very good, to gain confidence in the validity of the measurement, it is necessary to ensure that migration effects are reasonably low. To study migrations, the purity, P_i , and the stability, S_i , in a given bin are estimated. Purity in a bin is defined as the fraction of reconstructed events originated from the same bin at the generator level, $N_i^{rec\&gen}$. Stability considers migrations out of the bin and is defined as the fraction of generated events, provided they were not lost in the data selection after reconstruction, N_i^{gen} , that are also reconstructed in the same bin,

$$P_i = \frac{N_i^{rec\&gen}}{N_i^{rec}}, \quad (5.24)$$

$$S_i = \frac{N_i^{rec\&gen}}{N_i^{gen}}. \quad (5.25)$$

The purities and stabilities in $|t|$ and W are shown in Fig. 5.19. They are in general high, above 70% in most bins, and indicate low migration between the bins.

5.7.2 Study of Systematic Errors

Detector effects such as resolutions or calibration uncertainties that can not be minimized by enlarging the statistical sample, together with model uncertainties propagate to the acceptance estimation (eq. (5.23)) and therefore imply an uncertainty on the cross section measurement and on related variables. Systematic errors have been estimated using Monte Carlo. Systematic uncertainties were studied separately for each bin in W and t , where the systematic error in bin i , originating from a source s , has been computed at the acceptance level as

$$\delta\sigma_{i,s}^{sys} = \frac{|A_i^+ - A_i^-|}{2A_i}, \quad (5.26)$$

where A_i^+ and A_i^- are acceptances obtained after the respective systematic shifts, whereas A_i is the nominal acceptance. An overview of the relevant systematic uncertainties sources and the

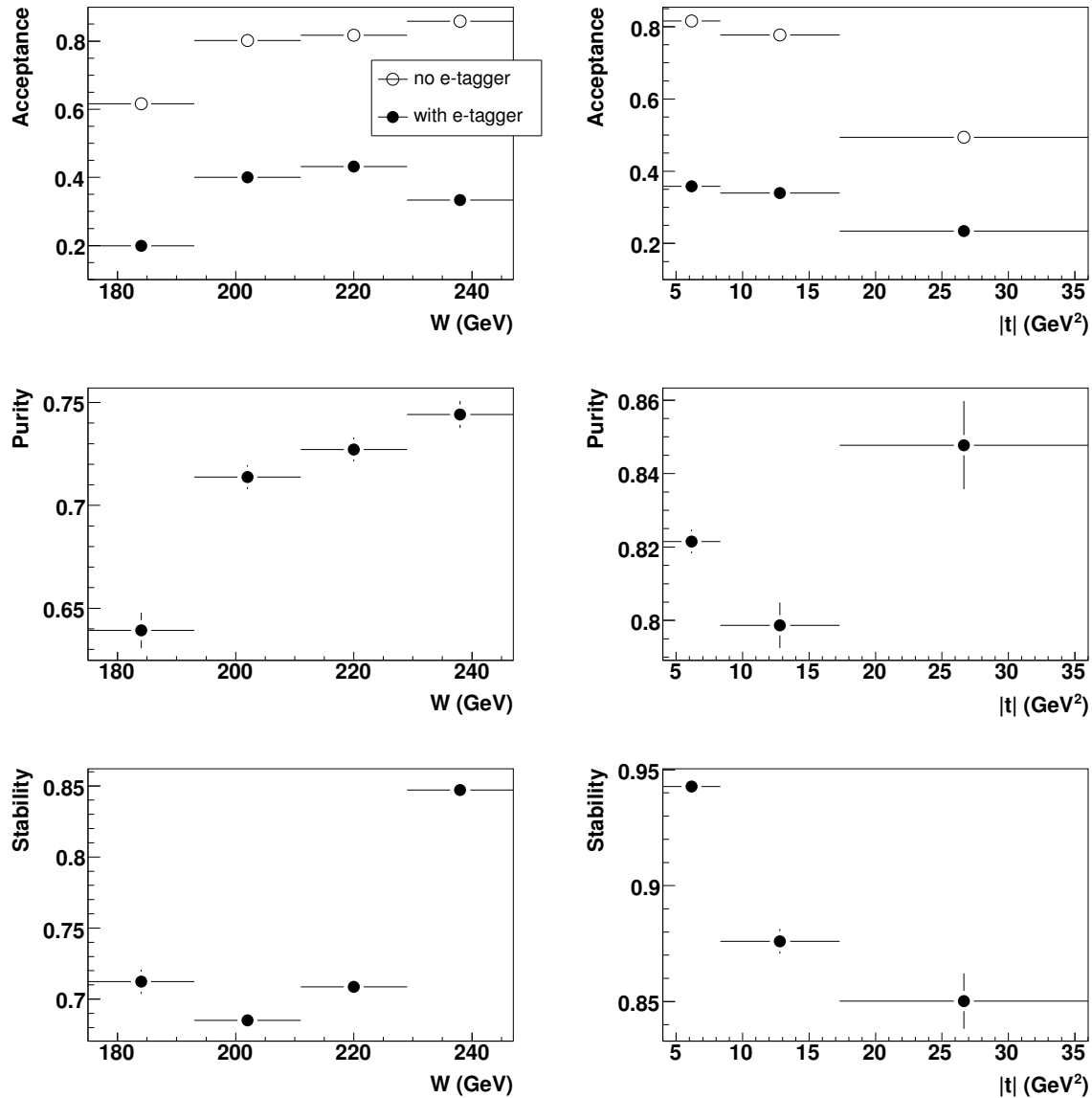


Figure 5.19: Acceptance, purity and stability in W and t bins. Open histograms show the acceptance without consideration of the electron tagger acceptance.

total systematic errors in bins in W and $|t|$ is given in Tab. 5.6 and 5.7. Selected distributions compared to those obtained by the systematic shifts for each source separately, are shown in Fig. 5.20 and 5.21.

Experimental Systematic Errors

- The energy scale uncertainty for an electromagnetic cluster measured by the SpaCal varies with energy and is known to average at 1%. The corresponding variation gives errors in the range of 2% to 4%.
- The uncertainty of the polar angle measurement of the charged particle in SpaCal is generally known to 1 mrad, but as the photon might originate from events without reconstructed vertex, a ± 2.5 mrad shift is applied, resulting in systematic errors ranging from 1% to 3%.
- The energy scale uncertainty of $\pm 1.5\%$ in the electron tagger results in errors from 1% to 6% except in the lowest W bin, where the error is 11%.
- The hadronic final state energy scale uncertainty variation of $\pm 4\%$ leads to an error of around 1%.
- The LAr energy threshold below which the cluster is considered as noise (400 MeV) was varied by 25%, affecting separately each cluster in the event. In case of a lower threshold, the former noise cluster enters the Y system and may decrease the rapidity gap of the event, if found at the edge of the newly reconstructed hadronic system. On the other hand, raising the threshold may, eventually, extend the rapidity gap as one or more hadrons would in this case be considered as noise and therefore not enter the final Y system. Variation of the noise threshold gives errors from 5% to 11%.
- The integrated luminosity is measured with an accuracy of $\pm 1.5\%$, contributing to a relative normalisation uncertainty of the cross section.

Systematic Errors Due to Uncertainties on Model Parameters

For the estimation of errors due to model dependencies (i.e. $x_{\mathbb{P}}$, t and M_Y), the systematic errors are estimated by reweighting the concerned distributions. The change in slope of a reweighted distribution is such that the systematic shift still describes other variable distributions in data within their statistical errors.

- The uncertainty due to $x_{\mathbb{P}}$ dependence was estimated by reweighting the $x_{\mathbb{P}}$ distribution by $(1/x_{\mathbb{P}})^{\pm 0.4}$ and yields an errors from 3% to 9%. More strongly reweighted $x_{\mathbb{P}}$ distribution would not describe the data, mainly at the larger $x_{\mathbb{P}}$ region.
- The uncertainty due to t dependence was estimated by variation of the $|t|$ distribution by $(1/|t|)^{\pm 0.2}$, according to the uncertainty of the measured t -slope of the cross section, as discussed in section 5.7.4 and yields an error between 1% and 4%.
- The uncertainty in the modelling of the proton remnant system Y was estimated by reweighting the generated M_Y distribution⁶ by $(1/M_Y^2)^{\pm 0.3}$ and yields an error between

⁶The generated invariant mass of the proton remnant, M_Y , is computed from the sum of all stable particles produced in the event, except the scattered electron and the scattered photon.

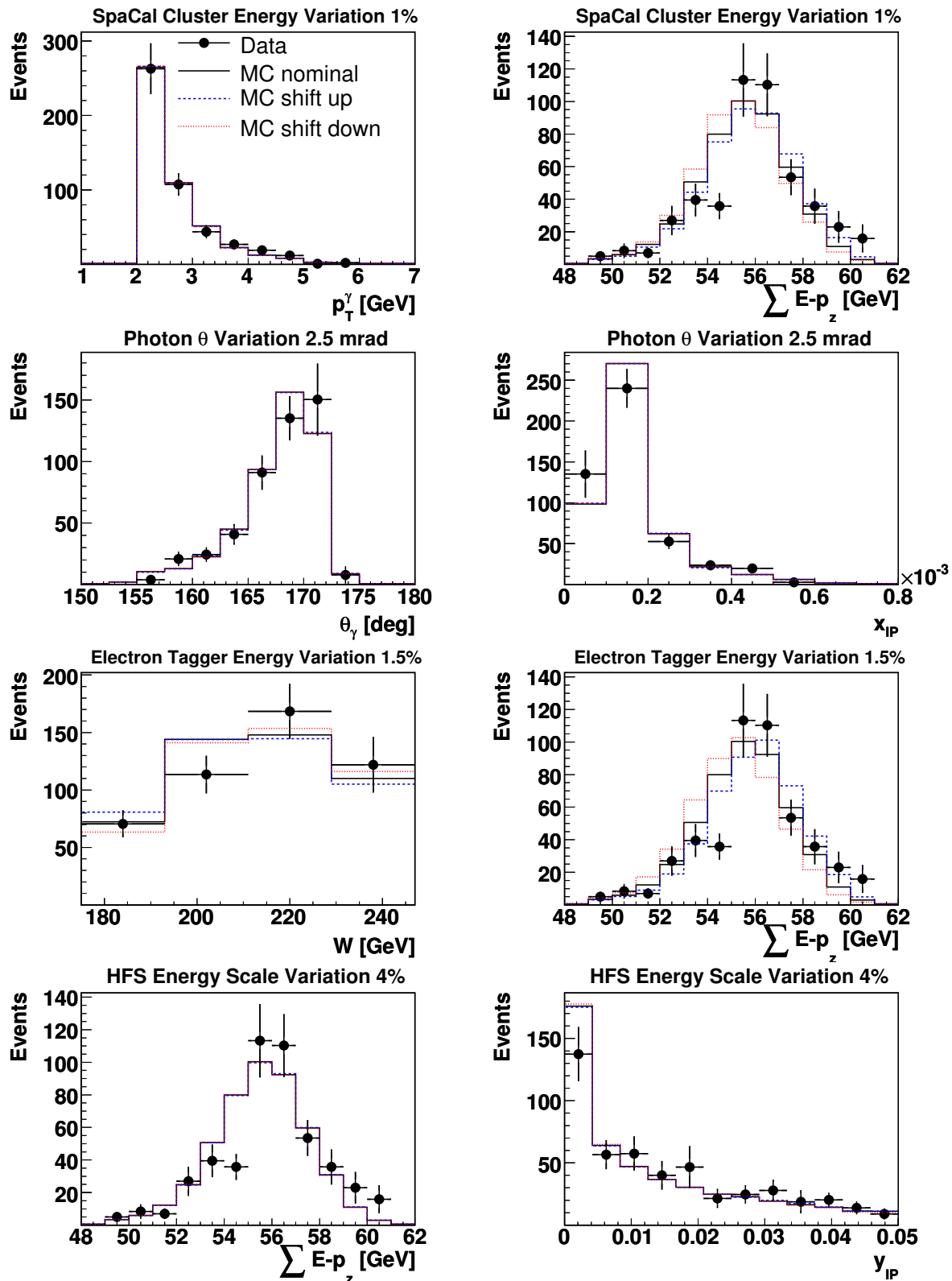


Figure 5.20: Effects of the systematic variations on the selected sample distributions. MC represents the sum of signal and background contributions.

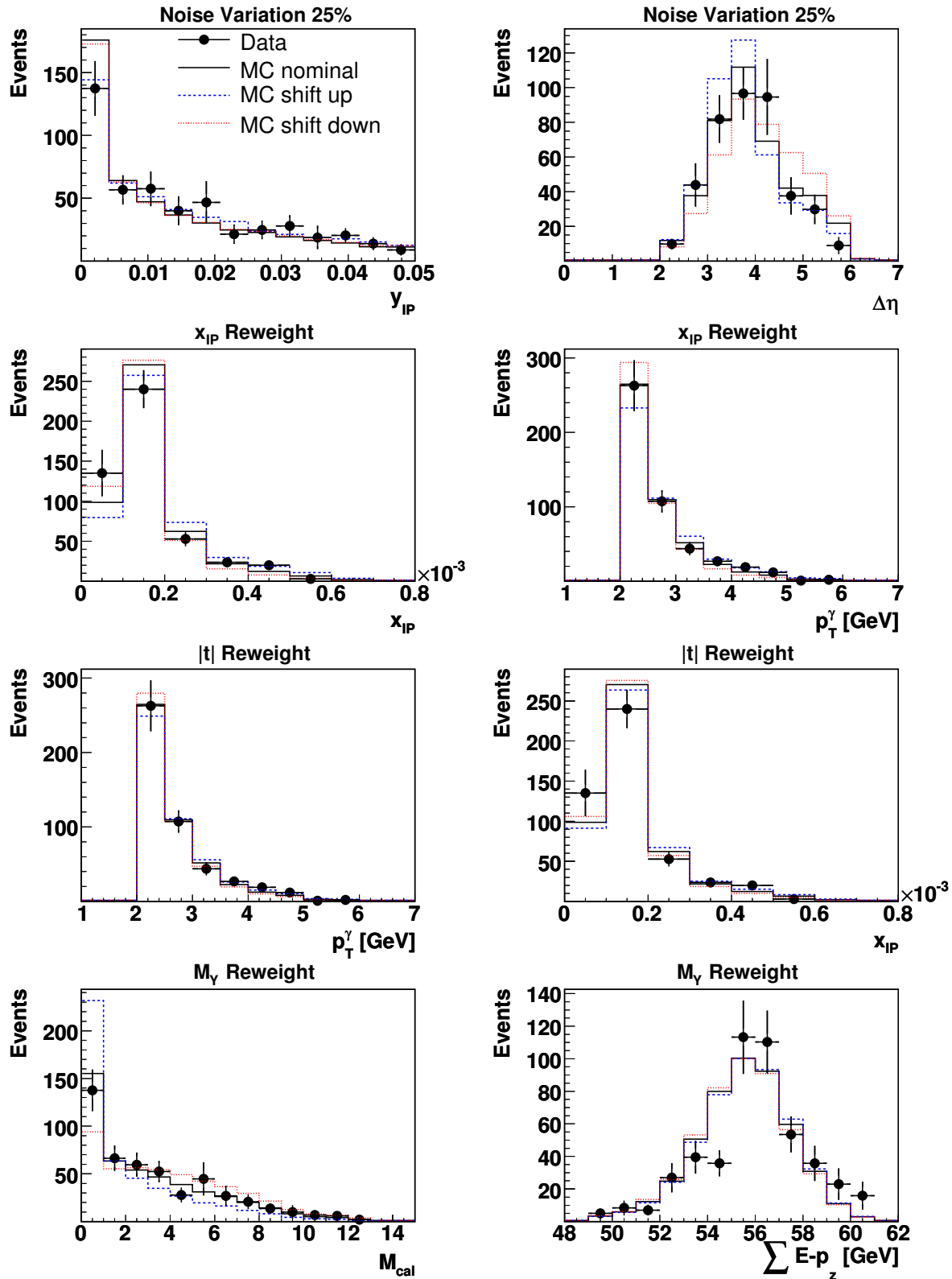


Figure 5.21: Effects of the systematic variations on the selected sample distributions. MC represents the sum of signal and background contributions.

source	W bin centers [GeV]				power
	185	202	220	240	δ
$E_\gamma \pm 1\%$	$\begin{matrix} \uparrow +4.3\% \\ \downarrow -3.9\% \end{matrix}$	$\begin{matrix} \uparrow -0.0\% \\ \downarrow -5.4\% \end{matrix}$	$\begin{matrix} \uparrow +7.6\% \\ \downarrow -0.8\% \end{matrix}$	$\begin{matrix} \uparrow +1.8\% \\ \downarrow -2.0\% \end{matrix}$	$\begin{matrix} \uparrow 2.64 \\ \downarrow 2.56 \end{matrix}$
$\theta_\gamma \pm 2.5$ mrad	$\begin{matrix} \uparrow -2.4\% \\ \downarrow +2.1\% \end{matrix}$	$\begin{matrix} \uparrow -2.8\% \\ \downarrow -0.2\% \end{matrix}$	$\begin{matrix} \uparrow -0.7\% \\ \downarrow +4.3\% \end{matrix}$	$\begin{matrix} \uparrow -3.2\% \\ \downarrow +3.0\% \end{matrix}$	$\begin{matrix} \uparrow 2.72 \\ \downarrow 2.60 \end{matrix}$
$E_{\text{etag}33} \pm 1.5\%$	$\begin{matrix} \uparrow +10.5\% \\ \downarrow -12.3\% \end{matrix}$	$\begin{matrix} \uparrow -1.2\% \\ \downarrow -1.7\% \end{matrix}$	$\begin{matrix} \uparrow -3.5\% \\ \downarrow +4.7\% \end{matrix}$	$\begin{matrix} \uparrow -6.0\% \\ \downarrow +6.6\% \end{matrix}$	$\begin{matrix} \uparrow 3.27 \\ \downarrow 2.03 \end{matrix}$
HFS $\pm 4\%$	$\begin{matrix} \uparrow -1.4\% \\ \downarrow +1.1\% \end{matrix}$	$\begin{matrix} \uparrow -1.1\% \\ \downarrow +0.8\% \end{matrix}$	$\begin{matrix} \uparrow -0.9\% \\ \downarrow +0.6\% \end{matrix}$	$\begin{matrix} \uparrow -0.9\% \\ \downarrow +0.6\% \end{matrix}$	$\begin{matrix} \uparrow 2.71 \\ \downarrow 2.75 \end{matrix}$
noise thr. $\pm 25\%$	$\begin{matrix} \uparrow -6.2\% \\ \downarrow +8.0\% \end{matrix}$	$\begin{matrix} \uparrow -5.8\% \\ \downarrow +7.4\% \end{matrix}$	$\begin{matrix} \uparrow -4.4\% \\ \downarrow +7.7\% \end{matrix}$	$\begin{matrix} \uparrow -3.7\% \\ \downarrow +7.2\% \end{matrix}$	$\begin{matrix} \uparrow 2.60 \\ \downarrow 2.69 \end{matrix}$
luminosity $\pm 1.5\%$	$\begin{matrix} \uparrow -1.5\% \\ \downarrow +1.5\% \end{matrix}$	$\begin{matrix} \uparrow -1.5\% \\ \downarrow +1.5\% \end{matrix}$	$\begin{matrix} \uparrow -1.5\% \\ \downarrow +1.5\% \end{matrix}$	$\begin{matrix} \uparrow -1.5\% \\ \downarrow +1.5\% \end{matrix}$	$\begin{matrix} \uparrow 2.73 \\ \downarrow 2.73 \end{matrix}$
PHOJET $\pm 100\%$	$\begin{matrix} \uparrow -1.7\% \\ \downarrow +1.7\% \end{matrix}$	$\begin{matrix} \uparrow -2.8\% \\ \downarrow +2.8\% \end{matrix}$	$\begin{matrix} \uparrow -3.3\% \\ \downarrow +3.3\% \end{matrix}$	$\begin{matrix} \uparrow -3.1\% \\ \downarrow +3.1\% \end{matrix}$	$\begin{matrix} \uparrow 2.68 \\ \downarrow 2.78 \end{matrix}$
x_P slope	$\begin{matrix} \uparrow -10.3\% \\ \downarrow +8.0\% \end{matrix}$	$\begin{matrix} \uparrow -6.0\% \\ \downarrow +5.0\% \end{matrix}$	$\begin{matrix} \uparrow -6.8\% \\ \downarrow +4.7\% \end{matrix}$	$\begin{matrix} \uparrow -4.5\% \\ \downarrow +3.2\% \end{matrix}$	$\begin{matrix} \uparrow 2.57 \\ \downarrow 2.88 \end{matrix}$
$ t $ slope	$\begin{matrix} \uparrow -3.8\% \\ \downarrow +3.1\% \end{matrix}$	$\begin{matrix} \uparrow -2.8\% \\ \downarrow +2.5\% \end{matrix}$	$\begin{matrix} \uparrow -3.3\% \\ \downarrow +2.7\% \end{matrix}$	$\begin{matrix} \uparrow -2.4\% \\ \downarrow +2.1\% \end{matrix}$	$\begin{matrix} \uparrow 2.70 \\ \downarrow 2.76 \end{matrix}$
M_Y slope	$\begin{matrix} \uparrow +3.9\% \\ \downarrow -0.0\% \end{matrix}$	$\begin{matrix} \uparrow +4.9\% \\ \downarrow -0.7\% \end{matrix}$	$\begin{matrix} \uparrow +4.3\% \\ \downarrow -0.6\% \end{matrix}$	$\begin{matrix} \uparrow +4.2\% \\ \downarrow -1.0\% \end{matrix}$	$\begin{matrix} \uparrow 2.74 \\ \downarrow 2.76 \end{matrix}$
$\Delta\delta$ propagation	$\begin{matrix} \uparrow +0.4\% \\ \downarrow -0.4\% \end{matrix}$	$\begin{matrix} \uparrow +0.4\% \\ \downarrow -0.4\% \end{matrix}$	$\begin{matrix} \uparrow +0.4\% \\ \downarrow -0.4\% \end{matrix}$	$\begin{matrix} \uparrow +0.4\% \\ \downarrow -0.4\% \end{matrix}$	-
Σ	17.5%	10.4%	11.8%	11.0%	$\begin{matrix} \uparrow +0.56 \\ \downarrow -0.78 \end{matrix}$

Table 5.6: Relative systematic errors per given source in each bin in W together with resulting variations of the power δ in the fit of W^δ of the γp cross section.

1% and 4%. Since there is no prediction (up to date) of the distribution of the proton remnant mass at large $|t|$ for this process, the same shape has been used as in the case of diffractive photoproduction of ρ mesons at large $|t|$ [18].

- The uncertainty of 100% assumed on the normalisation of the subtracted inclusive diffractive photoproduction background leads to an error of 1% to 3%. The size of uncertainty has been chosen such that the varied contribution of this background describes the data at low values of $\Delta\eta$ when cuts $\Delta\eta > 2$ and $y_P < 0.05$ are dropped.
- The propagation of the uncertainty on the power-law parameter in the γp cross section extraction procedure leads to a normalisation error of 4% for $d\sigma[\gamma p \rightarrow \gamma Y]/d|t|$ and is below 1% in all W bins for $\sigma[\gamma p \rightarrow \gamma Y](W)$ (see section 5.7.3).

The uncertainty on the normalisation of the inclusive diffractive photoproduction and the size of the variations of the model dependences in x_P , $|t|$ and M_Y were estimated from the measured distributions in the data. The total systematic error in bin i , $\delta\sigma_i^{sys}$, is obtained by adding the individual bin contributions $\delta\sigma_{i,s}^{sys}$ in quadrature,

$$\delta\sigma_i^{sys} = \sqrt{\sum_s (\delta\sigma_{i,s}^{sys})^2}, \quad (5.27)$$

and is found to be comparable or smaller than the statistical error in the same bin.

The $ep \rightarrow e\gamma Y$ cross section $d\sigma/dW$ is shown in Fig. 5.22 and the $d\sigma/d|t|$ cross section is shown in Fig. 5.23. Both cross sections are compared to predictions of the leading log approximation of the BFKL evolution.

source	$ t $ bin centers [GeV ²]			power	corr
	6	12	25	n	
$E_\gamma \pm 1\%$	$\begin{matrix} \uparrow +3.7\% \\ \downarrow -2.1\% \end{matrix}$	$\begin{matrix} \uparrow +2.5\% \\ \downarrow -6.1\% \end{matrix}$	$\begin{matrix} \uparrow +4.7\% \\ \downarrow -2.1\% \end{matrix}$	$\begin{matrix} \uparrow 2.60 \\ \downarrow 2.57 \end{matrix}$	C
$\theta_\gamma \pm 2.5$ mrad	$\begin{matrix} \uparrow -2.1\% \\ \downarrow +1.1\% \end{matrix}$	$\begin{matrix} \uparrow -3.0\% \\ \downarrow +0.2\% \end{matrix}$	$\begin{matrix} \uparrow +0.4\% \\ \downarrow -0.3\% \end{matrix}$	$\begin{matrix} \uparrow 2.60 \\ \downarrow 2.59 \end{matrix}$	U
$E_{\text{etag}33} \pm 1.5\%$	$\begin{matrix} \uparrow -1.1\% \\ \downarrow +0.4\% \end{matrix}$	$\begin{matrix} \uparrow -1.4\% \\ \downarrow +0.7\% \end{matrix}$	$\begin{matrix} \uparrow -0.2\% \\ \downarrow -0.1\% \end{matrix}$	$\begin{matrix} \uparrow 2.60 \\ \downarrow 2.60 \end{matrix}$	U
HFS $\pm 4\%$	$\begin{matrix} \uparrow -0.7\% \\ \downarrow +0.6\% \end{matrix}$	$\begin{matrix} \uparrow -1.7\% \\ \downarrow +1.3\% \end{matrix}$	$\begin{matrix} \uparrow -1.7\% \\ \downarrow +0.5\% \end{matrix}$	$\begin{matrix} \uparrow 2.59 \\ \downarrow 2.61 \end{matrix}$	C
noise thr. $\pm 25\%$	$\begin{matrix} \uparrow -4.0\% \\ \downarrow +6.7\% \end{matrix}$	$\begin{matrix} \uparrow -7.3\% \\ \downarrow +9.2\% \end{matrix}$	$\begin{matrix} \uparrow -9.8\% \\ \downarrow +12.3\% \end{matrix}$	$\begin{matrix} \uparrow 2.55 \\ \downarrow 2.60 \end{matrix}$	C
luminosity $\pm 1.5\%$	$\begin{matrix} \uparrow -1.5\% \\ \downarrow +1.5\% \end{matrix}$	$\begin{matrix} \uparrow -1.5\% \\ \downarrow +1.5\% \end{matrix}$	$\begin{matrix} \uparrow -1.5\% \\ \downarrow +1.5\% \end{matrix}$	$\begin{matrix} \uparrow 2.60 \\ \downarrow 2.60 \end{matrix}$	C
PHOJET $\pm 100\%$	$\begin{matrix} \uparrow -3.4\% \\ \downarrow +3.4\% \end{matrix}$	$\begin{matrix} \uparrow -1.3\% \\ \downarrow +1.3\% \end{matrix}$	$\begin{matrix} \uparrow -1.0\% \\ \downarrow +1.0\% \end{matrix}$	$\begin{matrix} \uparrow 2.58 \\ \downarrow 2.63 \end{matrix}$	C
x_P slope	$\begin{matrix} \uparrow -3.3\% \\ \downarrow +3.5\% \end{matrix}$	$\begin{matrix} \uparrow -2.6\% \\ \downarrow +2.9\% \end{matrix}$	$\begin{matrix} \uparrow -6.5\% \\ \downarrow +6.6\% \end{matrix}$	$\begin{matrix} \uparrow 2.60 \\ \downarrow 2.61 \end{matrix}$	C
$ t $ slope	$\begin{matrix} \uparrow -1.0\% \\ \downarrow +1.1\% \end{matrix}$	$\begin{matrix} \uparrow -0.8\% \\ \downarrow +1.0\% \end{matrix}$	$\begin{matrix} \uparrow -1.5\% \\ \downarrow +1.5\% \end{matrix}$	$\begin{matrix} \uparrow 2.60 \\ \downarrow 2.60 \end{matrix}$	C
M_Y slope	$\begin{matrix} \uparrow +2.8\% \\ \downarrow +1.0\% \end{matrix}$	$\begin{matrix} \uparrow +0.8\% \\ \downarrow +2.1\% \end{matrix}$	$\begin{matrix} \uparrow -2.6\% \\ \downarrow +4.6\% \end{matrix}$	$\begin{matrix} \uparrow 2.57 \\ \downarrow 2.62 \end{matrix}$	U
$\Delta\delta$ propagation	$\begin{matrix} \uparrow +2.8\% \\ \downarrow -3.7\% \end{matrix}$	$\begin{matrix} \uparrow +2.8\% \\ \downarrow -3.7\% \end{matrix}$	$\begin{matrix} \uparrow +2.8\% \\ \downarrow -3.7\% \end{matrix}$	-	U
Σ	8.9%	10.7%	14.2%	$\begin{matrix} \uparrow +0.03 \\ \downarrow -0.08 \end{matrix}$	

Table 5.7: Relative systematic errors per given source in each bin in $|t|$ together with resulting variations of the power n in the fit of $|t|^{-n}$ of the γp cross section and correlation type of each source. Correlated (C) systematic sources are defined as being those shifting all cross section values in the same direction under a single shift, whereas all other systematic sources, shifting values independently, are uncorrelated (U).

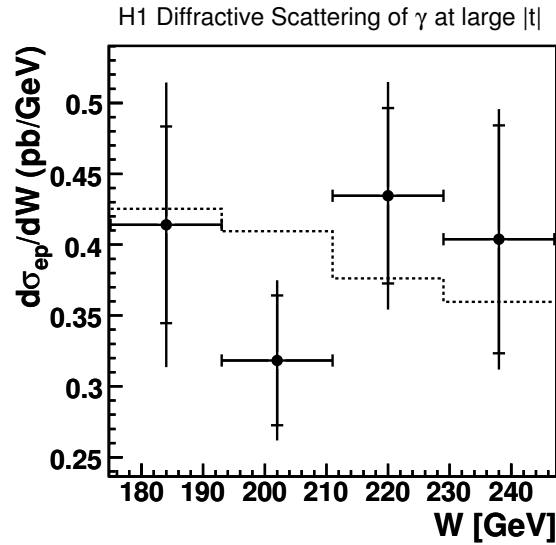


Figure 5.22: The ep cross section of diffractive scattering of photons off protons differentially in W in the phase-space defined by $4 < |t| < 36$ GeV², $y_P < 0.05$ and $Q^2 < 0.01$ GeV². The inner error bars show the statistical errors and the outer error bars show the statistical and systematic errors added in quadrature. The dotted line shows the result of the LLA BFKL prediction from HERWIG for the value of $\alpha_s^{BFKL} = 0.17$.

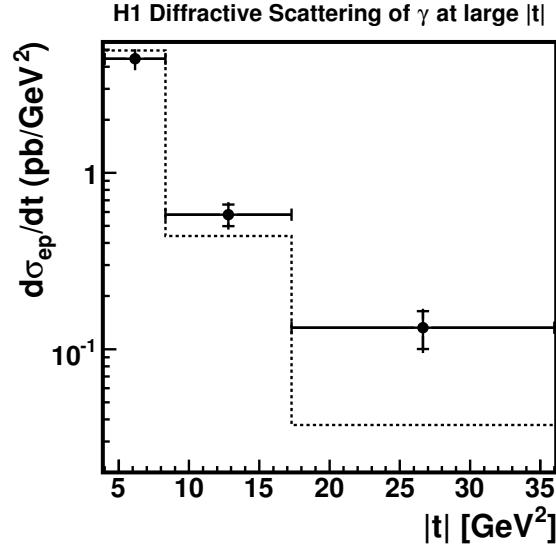


Figure 5.23: The ep cross section of diffractive scattering of photons off protons differentially in $|t|$ for $W = 219$ GeV, $y_p < 0.05$ and $Q^2 < 0.01$ GeV². The inner error bars show the statistical errors and the outer error bars show the statistical and systematic errors added in quadrature. The dotted line shows the result of the LLA BFKL prediction from HERWIG for the value of $\alpha_s^{BFKL} = 0.17$.

5.7.3 γp Cross-section Extraction Method

The measurable quantity at HERA is the cross section of electron proton scattering $ep \rightarrow e\gamma Y$. To study the hard part of the process, predicted by the perturbative QCD calculation, the γp cross sections $\sigma(W)$ and $d\sigma/d|t|$ will be extracted. The electron-proton cross section is converted into the γp cross section using relation

$$\frac{d\sigma[ep \rightarrow e\gamma Y]}{dWdt} = \Gamma(W) \frac{d\sigma[\gamma p \rightarrow \gamma Y]}{dt}, \quad (5.28)$$

where the $\Gamma(W)$ is the Weizsäcker-Williams approximation of the flux of photons in the photo-production regime [11],

$$\Gamma(y, Q^2) = \frac{\alpha_{em}}{2\pi} \left(\frac{2m_e^2 y}{Q^4} + \frac{1 + (1-y)^2}{yQ^2} \right), \quad (5.29)$$

using $W^2 = ys$ and is integrated in the following over the Q^2 range $[Q_{min}^2, Q_{max}^2]$, where

$$Q_{min}^2 = \frac{m_e^2 y^2}{1-y}, \quad Q_{max}^2 = 0.01 \text{ GeV}^2, \quad (5.30)$$

and α_{em} is the electromagnetic coupling constant. The flux integration over Q^2 gives

$$\Gamma(y) = \frac{\alpha_{em}}{2\pi} \left(2m_e^2 y \left(\frac{1}{Q_{max}^2} - \frac{1}{Q_{min}^2} \right) + \frac{1 + (1-y)^2}{y} \ln \frac{Q_{max}^2}{Q_{min}^2} \right). \quad (5.31)$$

The γp cross sections are extracted using an iterative procedure. In the case of the cross section measured as a function of W , the slope parameter, δ , is extracted at each step and the iteration finishes when δ is stabilised, i.e. when $\Delta\delta/\delta < 0.005$. In the case of $d\sigma[\gamma p \rightarrow \gamma Y]/d|t|$, bin centers in $|t|$ are evaluated at each step in addition to the extraction of the slope parameter n (with the same stabilisation condition as for δ).

In the following, we use an approximation of the γp cross section, $\tilde{\sigma}$, as a function of W that follows eq. (2.43) and is expressed as a power-law

$$\tilde{\sigma}[\gamma p \rightarrow \gamma Y](W) = N \cdot W^\delta, \quad (5.32)$$

where N and $\delta = 4\omega_0$ are the two parameters of the fit. The electron-proton cross section approximation in each bin of W ($W\square$) is then

$$\tilde{\sigma}[ep \rightarrow e\gamma Y] = N \cdot \int_{W\square} \Gamma(W)W^\delta dW, \quad (5.33)$$

where the integral runs over the W range of the corresponding bin. Finally, the measured γp cross section at each value of W_0 is obtained using eq. (5.32) and 5.33 as

$$\sigma[\gamma p \rightarrow \gamma Y](W_0) = \frac{d\sigma[ep \rightarrow e\gamma Y]}{dW} \Delta W \frac{W_0^\delta}{\int_{W\square} \Gamma(W)W^\delta dW}. \quad (5.34)$$

W_0 values at which the γp cross section have been extracted are listed in Tab. 5.8 and were obtained by first evaluating the middle of each bin $W\square$ and then shifting to the nearest rounded value.

Once the δ parameter is extracted from the fit in W , the $|t|$ dependence of the $d\sigma_{\gamma p}/d|t|$ cross section is evaluated using a similar approach,

$$\frac{d\sigma[\gamma p \rightarrow \gamma Y]}{d|t|}(|t|_0) = \frac{d\sigma[ep \rightarrow e\gamma Y]}{d|t|}(|t|_0) \frac{\overline{W}^\delta}{\int_W \Gamma(W)W^\delta dW}, \quad (5.35)$$

where $\overline{W} = 219$ GeV is the average W and the integral in the denominator on the right hand side of the equation runs over the W range of $175 < W < 247$ GeV. Thus, unlike the W cross section, the $d\sigma[\gamma p \rightarrow \gamma Y]/d|t|$ cross section differs from that at the ep level only by a normalisation factor of 0.0101.

Because of the low statistics, bins in $|t|$ are wide, in particular at high $|t|$. Because of the steeply falling distribution, we compute the bin center $|t|_0$ in a bin between $|t|_{min}$ and $|t|_{max}$ using the approach described in [13]. Using a fit of the form $|t|^{-n}$ (eq. (2.45)), the center position, $|t|_0$, in the bin between $|t|_{min}$ and $|t|_{max}$ is such that

$$|t|_0^{-n} = \frac{1}{|t|_{max} - |t|_{min}} \int_{|t|_{min}}^{|t|_{max}} |t|^{-n} d|t|, \quad (5.36)$$

and is determined at each fit iteration.

The cross section values in each bin in W and $|t|$ are shown in Tab. 5.8 together with corresponding values of the photon flux calculated at center of the bin. For $d\sigma_{\gamma p}/d|t|$ the flux is integrated over the full W range.

W_0 [GeV]	W range [GeV]	$d\sigma_{ep \rightarrow e\gamma Y}/dW$ [pb/GeV]	$\Gamma(W)$	$\sigma_{\gamma p \rightarrow \gamma Y}$ [nb]
185	175 – 193	$0.414 \pm 0.069 \pm 0.072$	0.0565	$2.02 \pm 0.34 \pm 0.35$
202	193 – 211	$0.318 \pm 0.046 \pm 0.033$	0.0431	$1.86 \pm 0.27 \pm 0.19$
220	211 – 229	$0.434 \pm 0.062 \pm 0.051$	0.0328	$3.06 \pm 0.44 \pm 0.36$
240	229 – 247	$0.404 \pm 0.080 \pm 0.044$	0.0246	$3.48 \pm 0.69 \pm 0.38$
$ t $ [GeV ²]	$ t $ range [GeV ²]	$d\sigma_{ep \rightarrow e\gamma Y}/d t $ [pb/GeV ²]	$\Gamma(W)$	$d\sigma_{\gamma p \rightarrow \gamma Y}/d t $ [pb/GeV ²]
6	4.0 – 8.3	$4.04 \pm 0.42 \pm 0.36$	0.0333	$401.0 \pm 41.3 \pm 35.7$
12	8.3 – 17.3	$0.58 \pm 0.08 \pm 0.06$	0.0333	$57.8 \pm 8.1 \pm 6.2$
25	17.3 – 36.0	$0.13 \pm 0.03 \pm 0.02$	0.0333	$12.5 \pm 3.1 \pm 1.8$

Table 5.8: Measured cross sections of the $ep \rightarrow e\gamma Y$ and $\gamma p \rightarrow \gamma Y$ process. The upper part of the table presents the measured cross section for different values of W in the range of $4 < |t| < 36$ GeV². The lower table presents the measured cross sections differentially in $|t|$ at $W = 219$ GeV. The first errors are statistical, the second systematic. The photon flux, Γ and the ranges in W and $|t|$ used for the measurements are also given.

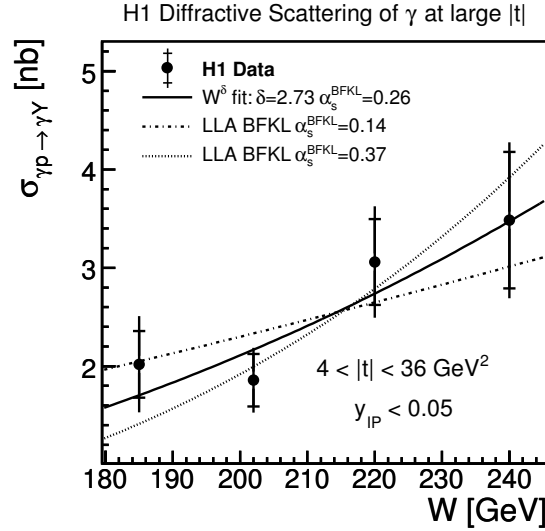


Figure 5.24: γp cross section of diffractive scattering of photons off protons as a function of W in the phase-space defined by $4 < |t| < 36$ GeV², $y_{IP} < 0.05$ and $Q^2 < 0.01$ GeV². The inner error bars show the statistical errors and the outer error bars show the statistical and systematic errors added in quadrature. The solid line shows the result of a fit to the cross section of the form W^δ . Additional curves show the LLA BFKL predictions from the HERWIG event generator for the values of $\alpha_s^{BFKL} = 0.14$ and 0.37 .

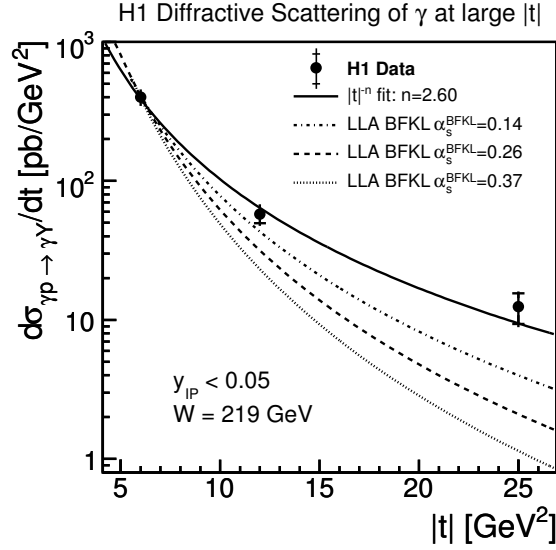


Figure 5.25: γp cross section of diffractive scattering of photons off protons differentially in $|t|$ for $W = 219$ GeV, $y_{IP} < 0.05$ and $Q^2 < 0.01$ GeV². The inner error bars show the statistical errors and the outer error bars show the statistical and systematic errors added in quadrature. The solid line shows the result of a fit to the cross section of the form $|t|^{-n}$. Additional curves show the LLA BFKL predictions from the HERWIG event generator for the values of $\alpha_s^{BFKL} = 0.13, 0.25$ and 0.36 .

5.7.4 $\sigma_{\gamma p}$ Measurement And Extraction of the α_s^{BFKL} Parameter

Figure 5.24 presents the γp cross section as a function in W , measured at four values of W for the experimental range $175 < W < 247$ GeV. The corresponding average $|t|$ value is 6.1 GeV² in the kinematic region limited to $Q^2 < 0.01$ GeV² and $y_{IP} < 0.05$. The inner bars are the statistical errors, whereas the outer error bars show the sum of the statistical and systematic errors added in quadrature. The cross section corresponds to the values shown in Tab. 5.8. As mentioned in section 5.4.1, the W cross section is expected to follow an approximate power-like behaviour. A fit of the form W^δ motivated by eq. (2.43) yields a power

$$\delta = 2.73 \pm 1.02 \text{ (stat)} \begin{matrix} +0.56 \\ -0.78 \end{matrix} \text{ (syst)} \quad (5.37)$$

with $\chi^2/ndf = 2.7/2$. The statistical error is the fit error, obtained after a fit to the data with the statistical errors only. To extract the systematic error of the power, fits to γp cross sections were performed after applying shifts due to each systematic source separately (described in section 5.7.2). The powers obtained from these fits were combined quadratically to give the systematic error.

The steep rise of the cross section with W is interpreted as an indication of the presence of a hard sub-process in the diffractive interaction. The δ value is compatible with that measured by H1 in diffractive J/ψ photoproduction [17], $\delta = 1.29 \pm 0.23(\text{stat}) \pm 0.16(\text{syst})$.

Figure 5.25 presents the γp cross section differentially in $|t|$ in the range of $4 < |t| < 36$ GeV² at $\bar{W} = 219$ GeV and in the kinematic domain $Q^2 < 0.01$ GeV² and $y_{IP} < 0.05$. The

data are reasonably described by a power

$$n = 2.60 \pm 0.19 \text{ (stat)} \begin{matrix} +0.03 \\ -0.08 \end{matrix} \text{ (syst)} \quad (5.38)$$

with $\chi^2/ndf = 1.6/1$. The statistic and systematic errors are derived following the same procedure as for the case of the W dependence of the cross section. In comparison to the diffractive photoproduction of J/ψ mesons at large $|t|$ measured by H1 [17], where they measure $n = 3.78 \pm 0.17(\text{stat}) \pm 0.06(\text{syst})$, the $|t|$ dependence measured in high $|t|$ photons is harder.

Comparison with LLA BFKL Prediction

Cross sections are compared to the leading log approximation BFKL prediction. Because the normalisation is not predicted in the LLA BFKL calculation, predictions are normalised to the integrated measured cross section.

The shape of the cross section as a function of W is compatible with a power law, as predicted. From the fit to the W dependence of the cross section the value of α_s^{Fit} is extracted using eq. (2.44), where $\delta = 4\omega_0$ and gives

$$\alpha_s^{Fit} = 0.26 \pm 0.10 \text{ (stat)} \begin{matrix} +0.05 \\ -0.07 \end{matrix} \text{ (syst)}. \quad (5.39)$$

This is shown in Fig. 5.24 as a solid line. Curves corresponding to one standard deviation are shown as two different BFKL predictions with $\alpha_s^{BFKL} = 0.14$ and 0.37 .

Previous measurements of diffractive scattering at HERA are described by BFKL predictions with α_s^{BFKL} compatible with the presented measurement. The H1 measurement of high $|t|$ J/ψ production [17] is well described with $\alpha_s^{BFKL} = 0.18$, whereas the H1 measurement of high $|t|$ ρ production [18] and ZEUS measurements of exclusive ρ , ϕ and J/ψ production at high $|t|$ are best described by $\alpha_s^{BFKL} = 0.20$.

The $|t|$ distribution predicted by the LLA BFKL is steeper than measured in the data and is shown as the dashed line in Fig. 5.25. The additional curves, representing LLA BFKL predictions at different α_s^{BFKL} values, were obtained by measuring the $|t|$ dependences of the Monte Carlo samples generated at different values of α_s^{BFKL} , ranging from 0.15 to 0.23. Fig. 5.27 plots the power n of the fit as a function of α_s^{BFKL} . From a linear fit to this distribution, the resulting power of the $|t|$ dependence for $\alpha_s^{BFKL} = 0.13$ is predicted to be $n = -3.21$ and for $\alpha_s^{BFKL} = 0.36$, it is $n = -4.07$. A possible deviation of the BFKL approach from the measured shape may be seen in the H1 measurement of ρ meson at high $|t|$ (see Fig. 5.26) as well, though the measured range in $|t|$ is only between 1.5 and 10 GeV^2 .

5.7.5 Summary

In this analysis, the first measurement of the diffractive scattering of photons off protons at high $|t|$ is studied. The process is measured in ep interactions at HERA based on a luminosity of 46.2 pb^{-1} . The kinematic range covered by the measurement is $4 < |t| < 36 \text{ GeV}^2$, $Q^2 < 0.01 \text{ GeV}^2$, $175 < W < 247 \text{ GeV}$ and $y_P < 0.05$. The clean signature of the process in the H1 detector and the requirement of large measured rapidity gaps makes it experimentally very interesting to measure. On the other side, the access to high $|t|$ region makes the process one of the candidates to test the BFKL dynamics of the hard process.

$\sigma(W)$ and $d\sigma/d|t|$ cross sections have been measured at the γp level and compared to the leading log approximation of the BFKL prediction. The W dependence is well described by the

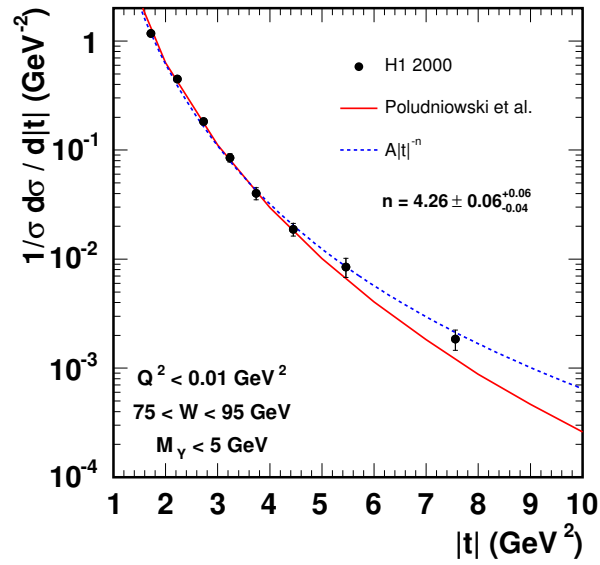


Figure 5.26: t dependence of the $ep \rightarrow epY$ cross section [18]. Inner error bars show the statistical errors, while the outer error bars represent the sum of statistical and systematic errors added in quadrature. The solid line shows the prediction from the BFKL model.

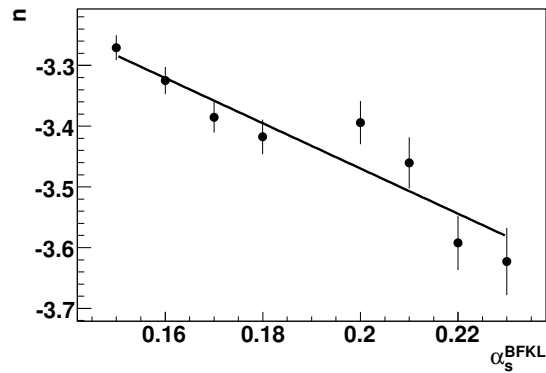


Figure 5.27: Dependence of the power of the $|t|^{-n}$ fit on the LLA BFKL prediction with different α_s^{BFKL} . The solid line shows the linear fit.

BFKL evolution with power $\delta = 2.73 \pm 1.02$ (stat) $^{+0.56}_{-0.78}$ (syst), representing one of strongest energy dependences measured in the diffractive processes. The corresponding effective value of α_s extracted from the measurement according to the LLA BFKL prediction [5], $\alpha_s^{Fit} = 0.26 \pm 0.10$ (stat) $^{+0.05}_{-0.07}$ (syst), is compatible with previous HERA measurements of diffractive scattering. The measured $|t|$ dependence is however harder than predicted by LLA BFKL.

Chapter 6

Conclusions

In this thesis, two different studies of diffractive phenomena have been performed on the data taken with the H1 experiment at the electron proton collider HERA.

Firstly presented is the study of the inclusive diffractive process $ep \rightarrow eXp$ in the deep inelastic regime, where the hard scale for application of perturbative QCD calculations is supplied by the large photon virtuality, Q^2 . The data were selected by means of tagging the scattered proton by the Very Forward Proton Spectrometer, measuring the scattered electron in the backward calorimeter and the hadronic system X in the central part of the detector. The VFPS detector has been installed at H1 in 2004 to take benefit of the HERA II phase luminosity increase. The analysed diffractive events are selected from the HERA running period 2006-2007, where the VFPS has operated smoothly. The study of the optics of the forward proton beam in 2006 revealed a significant loss of VFPS acceptance for proton relative energy loss, $x_{\mathbb{P}} \gtrsim 0.02$. The result of this study led to the modification of the beam optics settings through the introduction of the local proton beam bump at 200 m from the interaction point. The optics have been modified using the proton correction magnets such that the VFPS acceptance is maximised. The VFPS acceptance has been estimated using the fraction of events tagged in the VFPS in a sample of the inclusive diffractive events selected on the basis of the large rapidity gap (LRG) between the direction of the outgoing proton and the X system. A subsample of the VFPS tagged events corresponding to an integrated luminosity 24 pb^{-1} , i.e. the period where the proton beam bump at 220 m was close to its extreme, that is -6mm, has been compared to the simulation. To estimate the VFPS acceptance, the LRG data sample has been corrected for the contributions of the diffractive scattering with proton dissociation, $ep \rightarrow eXY$, and of the non-diffractive DIS process, $ep \rightarrow eX$. The acceptance has been estimated to be $\sim 75\%$ in the region of $0.010 \lesssim x_{\mathbb{P}} \lesssim 0.015$ and the distributions of the VFPS-tagged events have been shown to agree with the MC simulation.

The available integrated luminosity of $\sim 130 \text{ pb}^{-1}$ corresponding to nearly 900,000 VFPS tagged diffractive events in the DIS regime gives the possibility of a precise measurement of the diffractive structure function $F_2^{D(3)}$ in the near future, in the region of $0.008 \lesssim x_{\mathbb{P}} \lesssim 0.02$ and $|t| \lesssim 0.5 \text{ GeV}^2$. After the reconstruction program of $x_{\mathbb{P}}$ and t from the proton measured by the VFPS is finalised, the differential $F_2^{D(4)}(Q^2, \beta, x_{\mathbb{P}}, t)$ can be measured.

The second analysis presented leads to the cross section measurement of the diffractive photon scattering $\gamma p \rightarrow \gamma Y$, with large momentum transfer squared, t , where the final photon is separated from the proton dissociative system Y by a large rapidity gap. In this case, t provides the hard scale for the pQCD calculations, while $Q^2 \ll \Lambda_{QCD}^2$. The cross section

of this process has been measured in the kinematic domain $Q^2 < 0.01 \text{ GeV}^2$, $4 < |t| < 36 \text{ GeV}^2$, $175 < W < 247 \text{ GeV}$ and $y_{\mathbb{P}} < 0.05$. The measurement is based on the data collected during the HERA I phase in years 1999-2000, with the integrated luminosity of 46.2 pb^{-1} . The process provides a clean test of the underlying dynamics of the diffractive exchange, described in QCD by the BFKL approach. It also complements the measurements of diffractive production of vector mesons at high $|t|$. Measured cross sections at the γp level, $\sigma(W)$ and $d\sigma/d|t|$, are compared to the LLA BFKL calculation. A power-law dependence of the form $\sigma \sim W^\delta$ is fitted to the measured cross section $\sigma(W)$. The fit yields $\delta = 2.73 \pm 1.02$ (stat) $^{+0.56}_{-0.78}$ (syst) measured at an average $|t|$ value of 6.1 GeV^2 . Such a strong energy dependence is a clean signature of the hard regime of the interaction. The measured δ value is compatible with that measured by H1 in diffractive J/ψ photoproduction of $\delta = 1.29 \pm 0.23$ (stat) ± 0.16 (syst) [17]. A good description of the measured W dependence of the cross section is found with the BFKL-driven fit, where the extracted δ corresponds to the value of the $\alpha_s^{BFKL} = 0.26 \pm 0.10$ (stat) $^{+0.05}_{-0.07}$ (syst).

The cross section differential in $|t|$, at $W = 219 \text{ GeV}$, is fitted by the form $d\sigma/dt \sim |t|^{-n}$. The fit result is $n = 2.60 \pm 0.19$ (stat) $^{+0.03}_{-0.08}$ (syst). The $|t|$ dependence is harder than that of $n = 3.78 \pm 0.17$ (stat) ± 0.06 (syst) measured by H1 in the diffractive photoproduction of J/ψ mesons at large $|t|$ [17] and that of $n = 4.26 \pm 0.06$ (stat) $^{+0.06}_{-0.04}$ (syst) measured by H1 in the diffractive photoproduction of ρ mesons at large $|t|$ [18]. The LLA BFKL model predicts a $|t|$ dependence that is too strong and hence unable to describe the data. However, next-to-leading corrections, known to be large for the present leading order BFKL approximation [9], should be considered to make a strong statement.

Bibliography

- [1] H1 Collaboration, “The H1 detector at HERA”, *Nucl. Instrum. Methods A* **386**, 310 (1997)
- [2] H. Jung, “The RAPGAP Monte Carlo for Deep Inelastic Scattering”, 2006
- [3] H1 Collaboration, *Eur. Phys. C* **48**, 715 (2006)
- [4] B. List, A. Mastroberardino, “DIFFVM - A Monte Carlo Generator for Diffractive Processes in ep Scattering”, 1998
- [5] B. E. Cox, J. R. Forshaw, *J. Phys. G* **26**, 702 (2000)
- [6] F. W. Bopp, R. Engel, J. Ranft, “Rapidity gaps and the PHOJET Monte Carlo”, hep-ph/9803437
- [7] T. Abe, “Grape-Dilepton (Version 1.1): A generator for dilepton production in e p collisions”, *Comp. Phys. Comm.* **136**, 126 (2001)
- [8] I. F. Ginzburg, D. Yu. Ivanov, *Phys. Rev. D* **54**, 5523 (1996)
- [9] D. Yu. Ivanov, M. Wüsthoff, “Hard diffractive Photon-Proton Scattering at large t ”, *Eur. Phys. C* **8**, 107 (1999)
- [10] N. G. Evanson, J. R. Forshaw, “Diffractive photon production in γp and $\gamma\gamma$ interactions”, *Phys. Rev. D* **60**, 034016 (1999)
- [11] S. Frixione, M. L. Mangano, P. Nason, G. Ridolfi, *Phys. Lett. B* **319**, 339 (1993)
- [12] M. Beckingham, “Diffractive photoproduction of high p_T photons at HERA”, Ph.D. Thesis, University of Manchester (2003)
- [13] G. D. Lafferty and T. R. Wyatt, *Nucl. Instrum. Methods A* **355**, 541 (1995)
- [14] H1 Collaboration, “Diffractive photoproduction of high- p_t photons at HERA”, International Europhysics Conference on High Energy Physics, EPS03, Aachen (2003)
- [15] V. Fadin, E. Kuraev, L. Lipatov, *Phys. Lett. B* **60**, 50 (1975)
L. Lipatov, *Sov. J. Nucl. Phys.* **23**, 338 (1976)
V. Fadin, E. Kuraev, L. Lipatov, *Sov. Phys. JETP* **44**, 443 (1976)
V. Fadin, E. Kuraev, L. Lipatov, *Sov. Phys. JETP* **45**, 199 (1977)
Y. Balitzky, L. Lipatov, *Sov. J. Nucl. Phys.* **28**, 822 (1978)

- [16] L. Janauschek, “Elastic Photoproduction of J/ψ Vector Mesons at high Photon-Proton Centre-of-Mass Energy at the H1 Experiment at HERA”, Ph.D. Thesis, Ludwig-Maximilians-Universität, München (2004)
- [17] H1 Collaboration, “Diffractive Photoproduction of J/ψ Mesons with Large Momentum Transfer at HERA”, *Phys. Lett. B* **568**, 205 (2003)
- [18] H1 Collaboration, “Diffractive Photoproduction of ρ Mesons with Large Momentum Transfer at HERA”, *Phys. Lett. B* **638**, 422 (2006)
- [19] H1 Collaboration, “Performance of an Electromagnetic Lead/Scintillating-Fibre Calorimeter of the H1 Detector”, *Nucl. Instrum. Methods A* **374**, 149 (1996)
H1 Collaboration, “H1 Backward Upgrade with a SPACAL Calorimeter: the Hadronic Section”, DESY Report, **DESY-96-013**
- [20] V. Boudry *et al.*, “The Inclusive Electron Trigger for the SPACAL: Design and CERN-test Results”, H1 internal note, **H1-03/95-430**
- [21] R. Prosi: “Pedestrian’s Guide to the L4 Filter Farm”, H1 internal note, **H1-11/94-412**
- [22] S. Egli, E. Elsen, V. Lemaitre, K. Müller, H. Rick H.-C. Schultz-Coulon: “Calculating Event Weights in Case of Downscaling on Trigger Levels 1-4”, H1 internal note, **H1-04/97-517**
- [23] H1 Collaboration, “Proposal to Merge Level-4 and Level-5 Systems of the H1 Experiment”, **DESY PRC 99-03**
- [24] L. Favart *et al.*, “Proposal for Installation of a Very Forward Proton Spectrometer in H1 after 2000”, H1 internal note, **H1-05/00-582** and **DESY PRC-01/00**
H1 Collaboration, “Study on Acceptances and Resolutions of the H1 VFPS Detector”, Addendum to H1-05/00-582
- [25] H1 Collaboration, “ ep Physics beyond 1999”, H1 internal note, **H1-10/97-531**
H1 Collaboration, “Proposal for an Upgrade of the H1 Luminosity System and its Associated Electronics for HERA 2000”, **DESY PRC - 98/05**
- [26] G. A. Voss, “THE HERA-PROJECT”, presented at the 1st European Particle Accelerator Conference, Rome, Italy (1988)
- [27] W. Bartel *et al.*, “HERA Luminosity Upgrade”, proceedings of the Future Physics at HERA Workshop 1995/96, Vol. 2
- [28] M. Cuje *et al.*, “CIP and Level 1 Vertex Trigger”, Proposal (1997)
- [29] H1 Collaboration, “Proposal for an Upgrade of the H1 Forward Track Detector for HERA 2000”, **DESY PRC 98/06**
- [30] B. List, “The H1 silicon tracker”, *Nucl. Instrum. Methods A* **549**, 33 (2005)
- [31] W. Schüte, “Results of Measurements on the HERA proton beam position monitors”, Proceedings of the IEEE Particle Accelerator Conference, Chicago, Illinois (1989)

- [32] W. Schüte, M. Wendt, K.-H. Mess, “The New Directional-Coupler Pick Up for the HERA Proton Beam Position Monitoring System”, Proceedings of the IEEE Particle Accelerator Conference, Washington, D.C. (1987)
- [33] H1 Collaboration, “Measurement and QCD Analysis of Jet Cross Sections in Deep-Inelastic Positron-Proton Collisions at \sqrt{s} of 300 GeV”, *Eur. Phys. C* **19**, 289 (2001)
- [34] The ROOT System Home Page, <http://root.cern.ch/>
- [35] S. Levonian, private communication
- [36] A. Kwiatkowski, H. Spiesberger, H.-J. Möhring, “HERACLES 4.1 - An event generator for ep interactions at HERA including radiative processes”, in *Proc. of the Workshop on Physics at HERA, Vol. 3* (1991) p. 1294.
- [37] T. Sjöstrand, M. Bengtsson, ”The LUND Monte Carlo for jet fragmentation and e^+e^- physics - JETSET version 6.3 - and update”, *Comp. Phys. Comm.* **71**, 15 (1992)
- [38] T. Sýkora, R. Roosen, private communication
- [39] G. Marchesini *et al.*, “HERWIG 6.1 Release Note”, *Comp. Phys. Comm.* **67**, 465 (1992)
G. Corcella *et al.*, “HERWIG 6.4 Release Note”, arxiv:hep-ph/0201201 (2002)
- [40] H1 Collaboration, ”Diffractive deep-inelastic scattering with a leading proton at HERA”, *Eur. Phys. C* **48**, 479 (2006)
- [41] J. C. Collins, D. E. Soper, G. Sterman, *Nucl. Phys. B* **261**, 104 (1985)
- [42] V. N. Gribov, L. N. Lipatov, *Sov. J. Nucl. Phys.* **15**, 438 (1972)
Y. L. Dokshitzer, *Sov. Phys. JETP* **46**, 641 (1977)
G. Altarelli, G. Parisi, *Nucl. Phys. B* **126**, 298 (1977)
- [43] J.C. Collins, *Phys. Rev. D* **57**, 3051 (1998)
- [44] H1 Collaboration, ”Measurement and QCD Analysis of the Diffractive Deep-Inelastic Scattering Cross Section at HERA”, *Eur. Phys. C* **48**, 715 (2006)
- [45] M. Glück, E. Reya, “Dynamical parton distributions of the proton and small-x physics”, DESY Report, **DESY-94-205**
- [46] C. Adloff *et al.*, *Z. Phys. C* **74**, 221 (1997)
- [47] G. P. Salam, “An introduction to leading and next-to-leading BFKL”, presented at the Cracow School of Theoretical Physics, 1999
- [48] P. Newman, private communication

Acknowledgements

First of all my sincere gratitude goes to my supervisor Laurent Favart who introduced me to H1, for his great guidance and support - I am thankful for his patience and confidence in my work through the years of my study.

I warmly thank professors Daniel Bertrand and Gabriela Martinská who allowed me to study at the Université Libre de Bruxelles (ULB) and the University of Pavel Jozef Šafárik in Košice (UPJŠ) in a form of a co-tutorship. At this place I thank to Jozef Urban for being my co-tutor at UPJŠ and for his remote support and useful suggestions to my work. I also thank Dušan Bruncko for the 'pomeron discussions' and Pavel Murín, to whom I owe the most for his support, mainly in the early years of my studies. My warm thanks goes also to Dr. Kazi Firos and Peter Kaliňák.

I have spent three pleasant years of my PhD studies at the Interuniversity Institute for High Energies (IIHE) in Brussels, where I have met so many nice people - particularly I am thankful to the H1 group: Laurent Favart and Xavier Janssen for their suggestions and always a cheer mood; Pierre Marage who accepted to be the president of jury at my defense and for his priceless comments to this thesis; Robert Roosen for sharing his deep knowledge of the VFPS detector; Dr. Benoit Roland and Julie Delvax, with whom I shared the office, sometimes the way home at the very evenings, and, more importantly, the humour which made the tough times (when they appeared) much more bearable. I also appreciated company of Otman Charaf, Vincent Dero, Sherif Elgammal and Mathieu Labare, whose spontaneous teaching of Walloon was as fruitful as me teaching him Slovak.

Analysis of the high p_T photon scattering would not be so complete without numerous discussions with members of the H1 Diffractive Group at DESY in Hamburg, I benefited considerably from their comments. First of all I thank to Matthew Beckingham, with whom I have worked on the analysis - I enjoyed our numerous discussions very much and he was always ready to help when I needed it (I remember several mail exchanges after midnight). I also thank to Jan Olsson and Vincent Boudry for being referees for the analysis paper and tirelessly read and commented all the versions. I also thank to Anatoli Astvatsatourov and Tomáš Sýkora for their support in the VFPS analysis; Mirek Nožička, Deniz Sunar, Filip Tomasz, and Karel Černý, people who made my stays at DESY much more enjoyable.

Although Brussels does not offer so much sun over the year, it gathers many nice and unique people from all around the world, whose friendship I value so much that no sun is needed anymore to cheer me up. Thank you for all the great moments Alexandra, Hani, Federica, Ben, Roxana, Radu, Alexander, Axelle, Mila and Rado.

A big hug goes to my family, which I have seen so seldom during recent years, for all their support and for turning into feast each day I showed at home - thank you mom, dad and Miloš.

My sweetest thanks go to my lovely Tekla, for being in my life and meaning so much to me.

